The Thesis Committee for Matthew Halperin Manley
Certifies that this is the approved version of the following thesis:

Experimental Investigation of the Effects of Electrical Currents in Small-scale Contact Regimes

APPROVED BY
SUPERVISING COMMITTEE:

Supervisor:

Krishnaswamy Ravi-Chandar

Sikhanda Satapathy

Experimental Investigation of the Effects of Electrical Currents in Small-scale Contact Regimes

by

Matthew Halperin Manley, B.S.E.

Thesis

Presented to the Faculty of the Graduate School of
The University of Texas at Austin
in Partial Fulfillment
of the Requirements
for the Degree of

Master of Science in Engineering

The University of Texas at Austin
August 2010

Dedication

This work is dedicated to my muses Carl Sagan and Gene Roddenberry. Their philosophies and lives' work have inspired me to see the world with an open and critical mind as well as to dream of a brighter tomorrow for humanity.

Acknowledgements

I want to give my sincere thanks to those who have helped me in this endeavor. My advisor, Dr. Krishnaswamy Ravi-Chandar, whom I first met at a seminar during my senior year at the University of Michigan and whose work led me to Austin, Texas the following fall. I have gotten invaluable ideas and feedback during research meetings with Dr. Sikhanda Satapathy from the Institute for Advanced Technology, Dr. Laxminarayan Raja, and Javan Marshall Albright. Dr. Dewei Xu has been very helpful in giving me a background of the instrumentation and showing me around the laboratory.

I also want to thank those who have made other important contributions: my predecessor, Alfonso García López for his useful internship report; Jeffrey Cook for training me in scanning electron microscopy, Dr. Donggao Zhao for use of electron backscatter diffraction in his laboratory, and Pablo Cortez for technical assistance.

Finally, my parents Dr. Ronald Manley and Dr. Linda Halperin have instilled in me the drive and determination to pursue any opportunity. Thank you for everything.

August 13, 2010

Abstract

Experimental Investigation of the Effects of Electrical Currents in Small-scale Contact Regimes

Matthew Halperin Manley, M.S.E.
The University of Texas at Austin, 2010

Supervisor: Krishnaswamy Ravi-Chandar

Railguns undergo excessive wear between the projectile and the electromagnetic launcher rails due to the hypersonic relative motion and very large current density involved. The wear effects at the small-scale on the rail-armature interface are not well known but need to be examined in order to support the development of a multishot launcher. Proposed contact regimes in the surface asperity interactions include solid-solid contact, liquid-metal lubricated contact, and arcing. In the present work, a modified Mesoscale Friction Tester (MFT) equipped with a probe and substrate was used to investigate experimentally the arcing and friction conditions that the rail-armature interface would experience. Copper probes with a range of radii of curvature were electrochemically etched and polished to submicrometer roughness. The minimum electrode distances for arcing to occur was found in air at atmospheric pressure and led to a modified Paschen curve where field emission of electrons was the dominant physical mechanism as opposed to Townsend avalanche of ionized gas. Arcing erosion was studied by varying the current, number of strikes, dwell time, and nearest electrode positions horizontally and vertically. Copper-copper friction with a constant normal force resulted in reduced wear when applying a constant current between the electrodes.

Table of Contents

List of Tables

List of Figures

Chapter 1

Introduction: Research and Development of Railguns

1.1 BACKGROUND ON RAILGUN DEVELOPMENT

The conceptual basis behind an electromagnetic launcher for firing projectiles dates back to the early twentieth century. An ongoing goal of research into the railgun, a device with electrically conductive rails and the properties of the coupled magnetic field to accelerate a projectile along the length of said rails, has been to develop a launcher capable of multiple shots without degradation in performance. Current work to understand some of the physical interactions (e.g. erosion along the rail-armature interface) better may prove significant in furthering the development of a multishot electromagnetic launcher.

1.1.1 Components and function

The essential components of a railgun consist of a pulsed-power supply, conductive parallel rails, and an armature situated between the rails that conducts current and houses the projectile. The Lorentz force, introduced in 1892 by Dutch physicist Hendrik Lorentz, propels the armature along the rails with a force F of magnitude:

$$F = \frac{1}{2} L' i^2 \qquad (1.1)$$

where:

L': axial inductance gradient (henries/meter)

i: electric current (amperes)

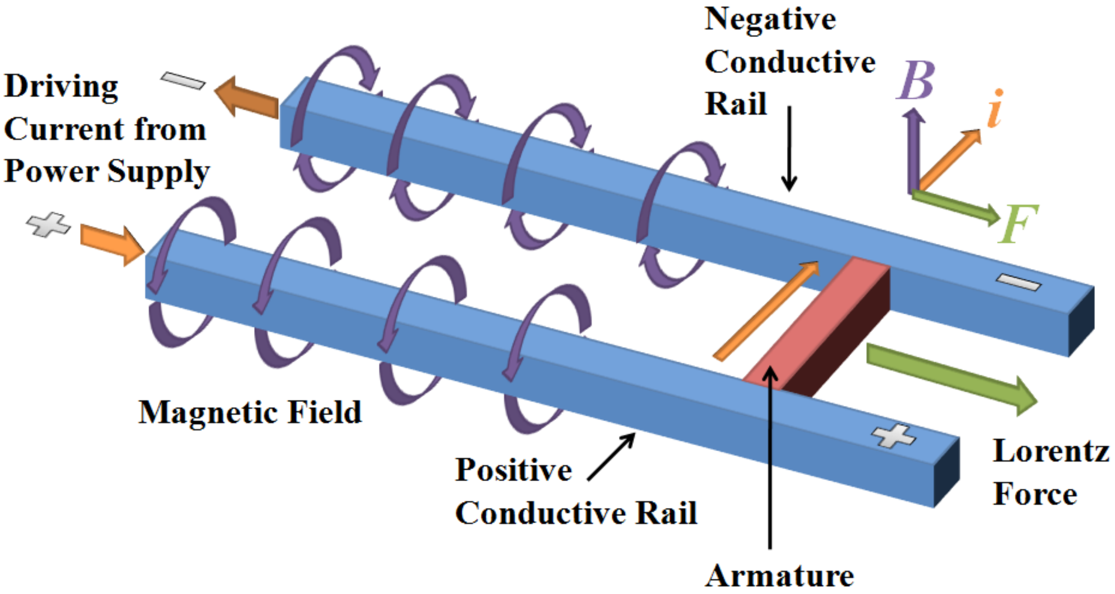

Figure 1.1: Railgun components and Lorentz force

A driving current, on the order of millions of amps, goes along the closed circuit from the positive conducting rail, through the armature, and back to the power supply along the negative conductive rail (Fig. 1.1). The Lorentz force will accelerate the armature housing the projectile along the length of the rails until it has surpassed the rail end and the circuit is broken. The projectile exits the railgun with an instantaneous speed or muzzle velocity that is used to measure the kinetic energy:

$$E_k = \frac{1}{2} m v^2 \tag{1.2}$$

where:

m: projectile mass (kilograms)

v: muzzle velocity (meters/second)

1.1.2 Contemporary issues

The Lorentz force acts orthogonal to the current i and magnetic field B (Fig. 1.1). A greater force will result in a greater kinetic energy and so can be increased by rail length or driving current. However, with the former, a larger Lorentz force makes it a design challenge for the rails to maintain a parallel geometry. The power supply results in current densities on the order of 10^{10} A/m^2 that can damage rails from electrical arcing [1].

1.2 OUTLINE OF THIS THESIS

The small-scale surface effects (10^{-5} to 10^{-8} m) on the armature and rails due to the current flow are not well known. It has been proposed by Brown et al. [1] that there are multiple contact regimes – such as solid-solid contact, liquid-metal lubricated contact, and arcing contact – that coexist through surface asperity interaction. This contact model is a modified form of the Bowden-Tabor model where contact and separation of asperities is continuously occurring from the relative motion between the rails and armature during the firing of a railgun [2,3]. Due to the difficulties of directly probing the rail-armature interface to understand the tribological behavior better, more controlled experiments have been performed in a laboratory setting to experimentally simulate the appropriate conditions [1].

Experiments to study some of the small-scale effects on the rail-armature interface involved the use of a modified Mesoscale Friction Tester (MFT) such that a closed electrical circuit can be formed with the probe and sample. Similar current densities as found in a railgun (approximately 10^{10} A/m^2) have been achieved on the device [1,4]. This thesis will describe the process, data, and analysis of the arcing and solid-solid contact experiments for the purpose of better understanding the qualitative and quantitative small-scale effects that would be encountered on the rail-armature interface and aid in development of a multishot electromagnetic launcher. This thesis is divided into six parts: the motivation for the research into small-scale contact regimes in the rail-armature interface in railguns is discussed in the present chapter. A description of the experimental equipment and procedure used to carry out an investigation into said contact regimes is presented in Chapter 2. The relationship between arcing and distance, a modified form of the Paschen curve, is discussed in Chapter 3. The erosion of material from arcing and from sliding contact are examined in Chapters 4 and 5 respectively. Finally, the conclusions from the investigation are summarized in Chapter 6.

Chapter 2

Methodology: Experimental Equipment and Setup

2.1 MESOSCALE FRICTION TESTER (MFT)

The Mesoscale Friction Tester (MFT) was developed at the University of Texas at Austin to bridge the gap in mechanical testing of interfacial interaction between the nano- and micro-scales. For friction experiments, the MFT can apply forces between 10 nN to 1 mN over contact radii from 10 nm to 10 μm. As it is greater than the loading range for an atomic force microscope (AFM) and interfacial force microscope (IFM) but below that of a surface force apparatus (SFA) it is able to conduct experiments in this intermediate range [4]. The MFT was modified to pass direct current (dc) and uses state-of-the-art actuators, sensors, and digital data acquisition and control systems (Fig. 2.1) [1,4].

2.1.1 Stage movement controls

Samples for the MFT are placed underneath a stationary probe. The sample can be brought to a chosen distance through a computer interface that controls coarse and fine movement. Coarse vertical translations are performed using a Newport 20025 stepper motor stage, while fine movements of 1 nm resolution use a piezoelectric (PZT) Physical Instruments, Inc P-562.3CD stage that can move up to 200 μm along each of the XYZ axes. Additionally, cantilever beam positioning can be adjusted in the MFT through a screw-tightening system that allows for translations and rotations in the XY directions.

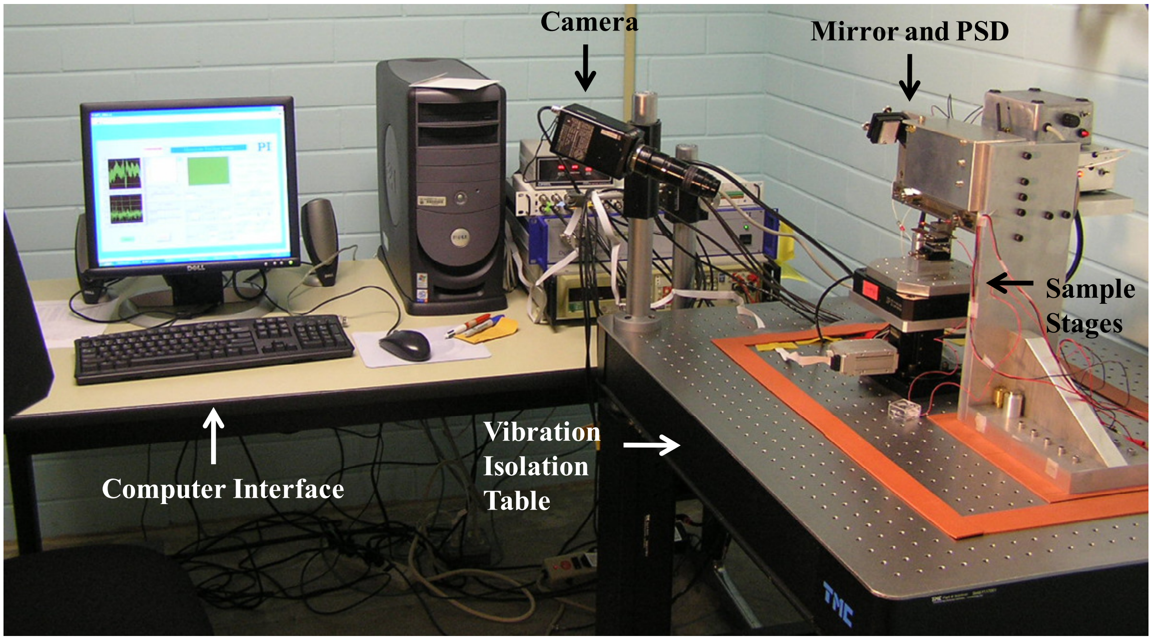

Figure 2.1: Mesoscale friction tester on a vibration isolation table

2.1.2 Measuring probe movement

The probe is mounted onto a beam where its movement is measured through the deflection of a laser beam reflecting from a polished silicon reflector bonded to the tip of the cantilever beam, traveling to a tilt-adjustable mirror, through a rotation-adjustable polarizer, and onto a two-dimensional position sensitive device (PSD), connected to the computer data acquisition software (Fig. 2.2). The Blue Sky Research MINI635-03C10WL laser diode uses a 635 nm beam wavelength and has beam diameter less than 500 µm. The Hamamatsu S2044 position sensitive detector (PSD) has a Hamamatsu

C4674 processing circuit and Schatvitz 02291331-000 direct current power supply. The coordinates of the laser beam on the PSD are output as XY voltages, which can be calibrated using beam theory and the known thickness t, length L, and width B of the beam to find the corresponding normal and lateral forces and deflections (Fig. 2.3).

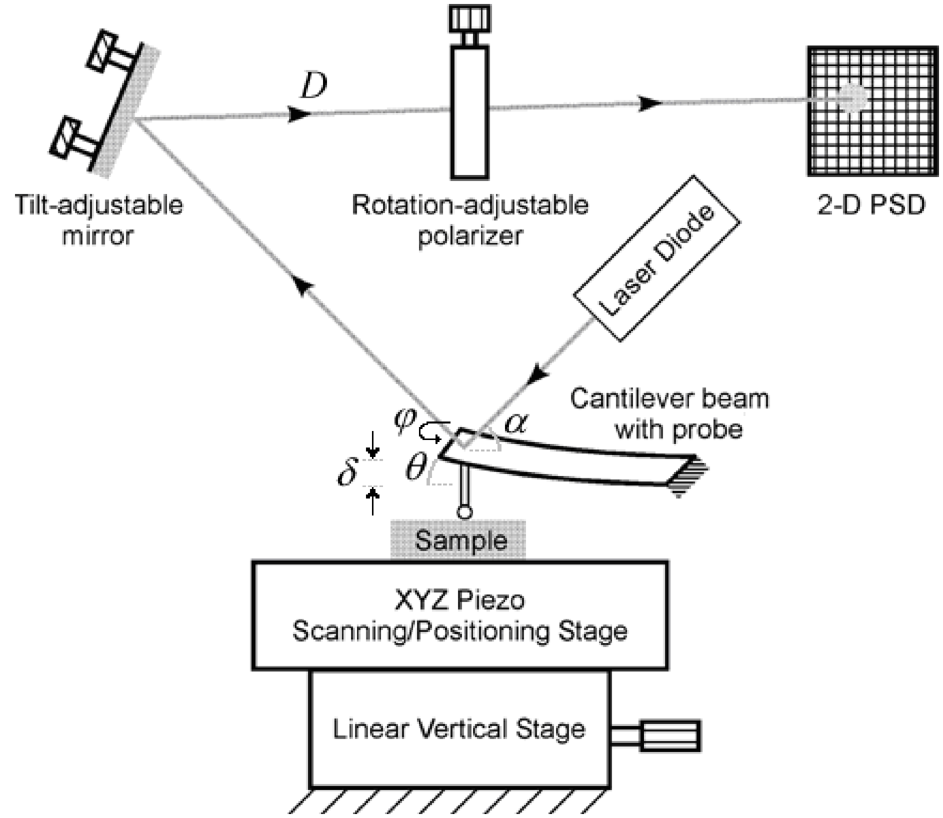

Figure 2.2: Diagram illustrating the operating principle of the MFT [4,5]

The PSD vertical and horizontal deflections, V_{PSD} and U_{PSD}, respectively:

$$V_{PSD} = 2\theta D + \delta \approx 2\theta D \tag{2.1}$$

$$U_{PSD} = 2\varphi D \cos\alpha \tag{2.2}$$

where:

θ: beam rotation angle (radians)

D: light path of laser beam (meters)

δ: vertical deflection at laser reflection spot (meters)

φ: beam twist angle (radians)

α: incident beam angle (radians)

From Euler-Bernoulli beam theory and elementary torsion theory (the setup geometry assumes that $D >> L$), the cantilever beam deflection, rotation, and twist at its free end in the XYZ directions are [4]:

$$\delta(L) = \frac{4PL^3}{EBt^3} \tag{2.3}$$

$$\theta(L) = \frac{6PL^2}{EBt^3} \tag{2.4}$$

$$\varphi(L) = \frac{3TL}{GBt^3} \tag{2.5}$$

where:

P: point force on beam (newtons)

E: Young's modulus of beam (pascals)

T: torque on beam (newton meters)

G: shear modulus of beam (pascals)

The beam stiffness is sensitive to thickness on the order of $1/t^3$ and normal and shear loads are sensitive to length on order of $1/L^2$ and $1/L$, respectively. The length of the probe on the beam and the weight of the silicon reflector at the tip do add a bending moment that is not accounted for in the beam rotation equation (2.4), but this effect is negligible. An axial force F_a acts on the probe from friction, in addition to the expected normal force N and lateral force F [4], but this is again estimated to be negligible.

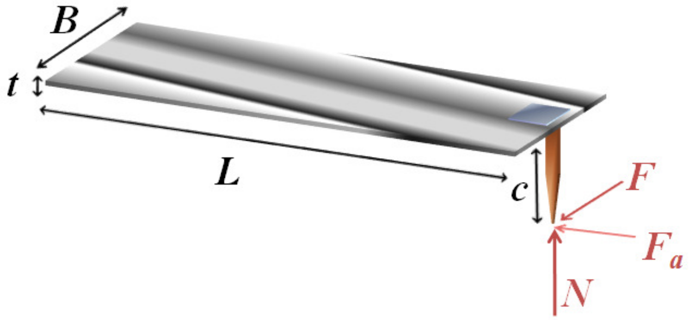

Figure 2.3: Cantilever beam dimensions and forces acting on probe

2.1.3 Power supply

The power supply was used to set a constant voltage potential between the substrate and probe. Experiments involved one of two different power supplies. The primary Kepco Model 300-8-1200 Power Supply had a voltage range up to 300 V and was controlled using the computer interface. An alternative power source was the Hoefer Scientific Instruments Model # PS 2500, which had a voltage, current, and power range, respectively, of 0-2500 V, 0-300 mA, and 0-375 W, and was controlled manually.

2.1.4 Electrical measurement

An electric circuit was formed by the power supply with voltage V_{in}, the probe and substrate (representing the rail-armature interface), fixed resistor of 2485 Ω, and a potentiometer with maximum resistance 50.39 kΩ. The polarity could be reversed by making the probe a cathode (Fig. 2.4) or anode (Fig. 2.5) depending on whether the electric current from the power supply was flowing out of it or into it, respectively. The electric circuit was wired inside a metal container (Fig. 2.6) to reduce interference from external electromagnetic sources and a thin aluminum sheet acts as shielding on a low-pass filter that connects the output voltage V_{out}. Grounding the circuit to the MFT is essential in reducing the noise. A Fluke 26 Series III Digital Multimeter can be inserted into the circuit where desired to monitor values of the voltage, current, or resistance.

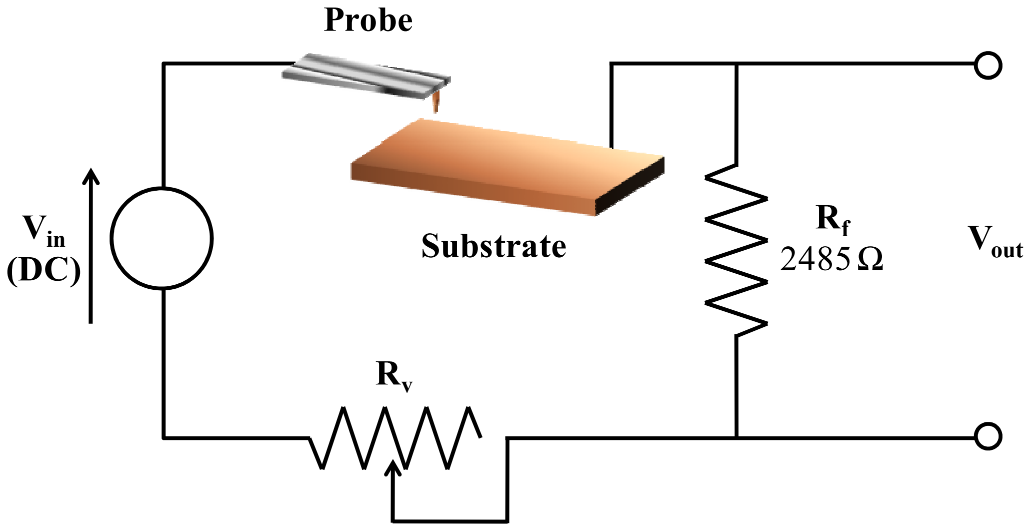

Figure 2.4: Electric circuit diagram for polarity with cathode (negative) probe

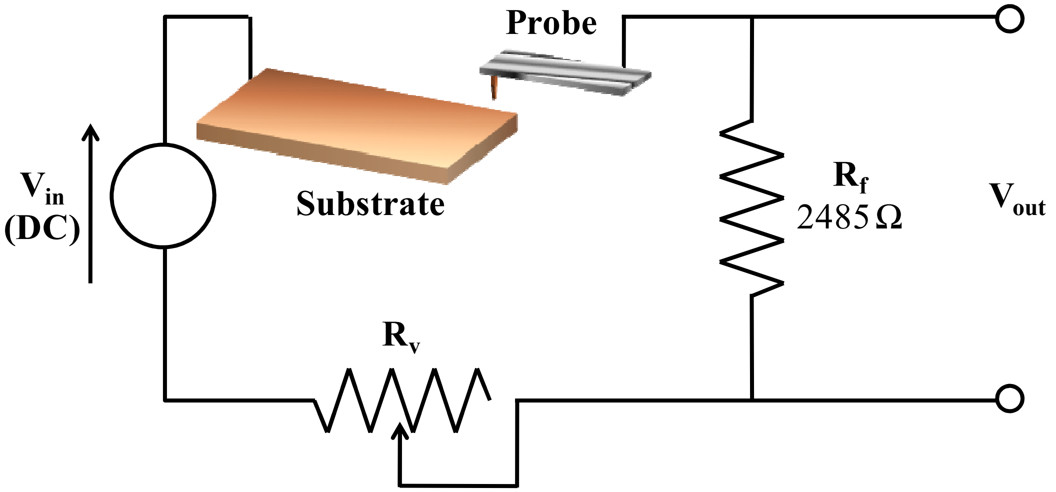

Figure 2.5: Electric circuit diagram for polarity with anode (positive) probe

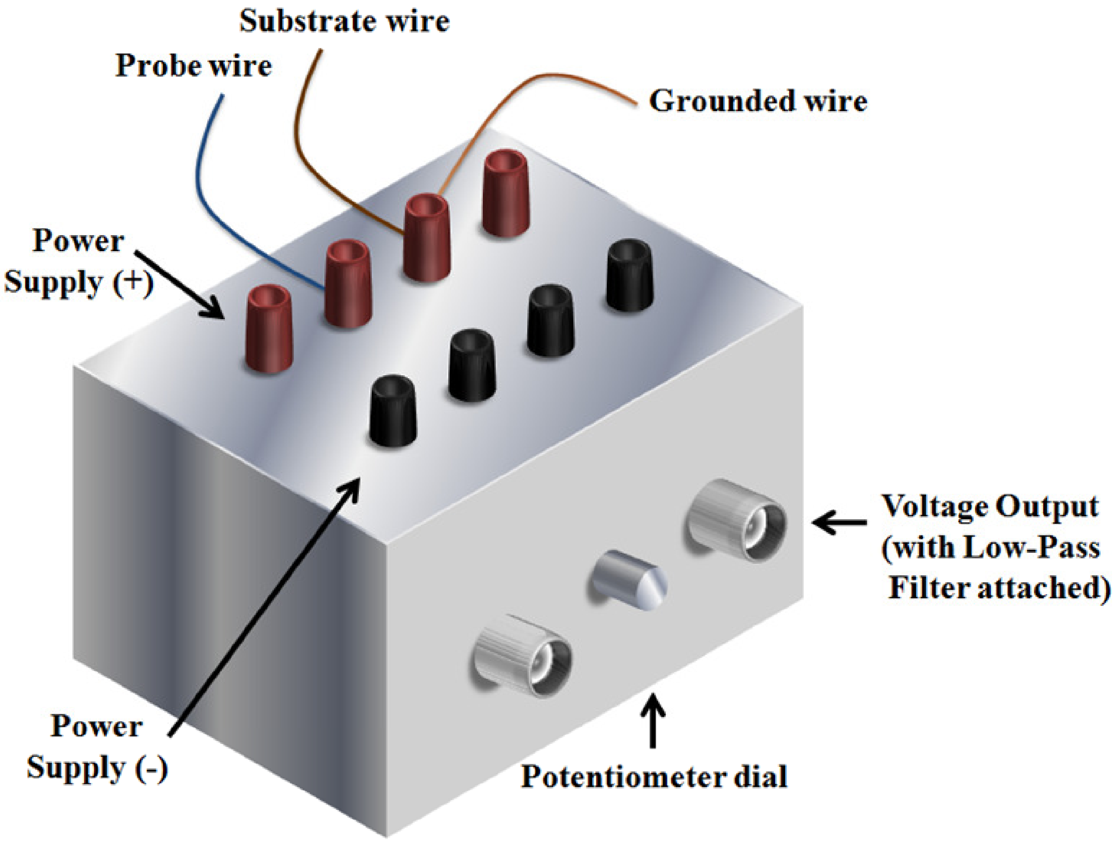

Figure 2.6: Diagram of metal box enclosing electric circuit, showing external terminals

2.1.5 Data acquisition system

A Dell Inspiron 8400 personal computer with National Instruments PCI-GPIB 488.2 board and DAQ M-series PCI6221 allow for a digital data acquisition system and control of almost all MFT functions. A virtual instrument program was written that displays the PSD component voltage and light spot position, PZT stage position, shunt voltage and current, temperature, and relative humidity (Fig. 2.7). In addition, the data sample rate, PZT position, and the size, dimension, and speed of the scan can be set.

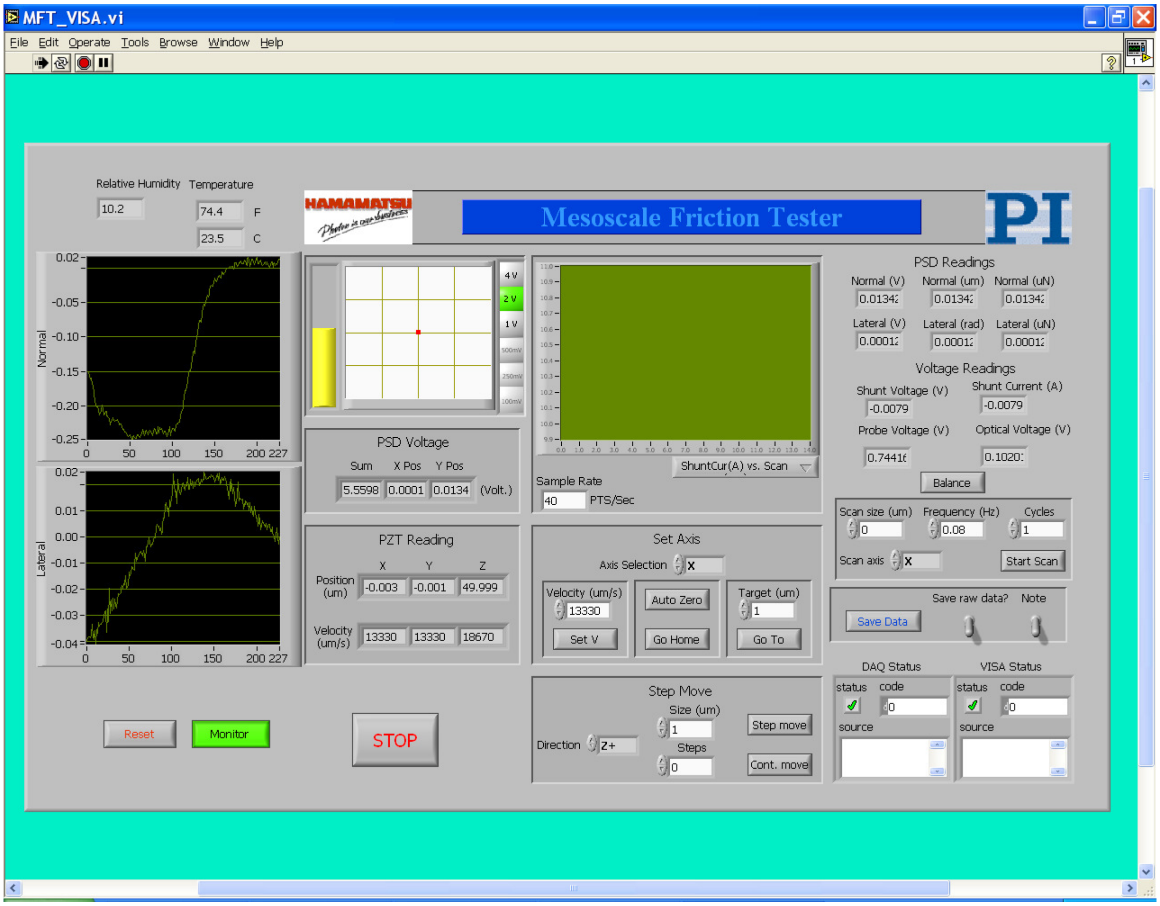

Relative Humidity: 10.2
Temperature: 74.4 F, 23.5 C

PSD Voltage (Volt.): Sum 5.5598, X Pos 0.0001, Y Pos 0.0134

PZT Reading:

	X	Y	Z
Position (um)	-0.003	-0.001	49.999
Velocity (um/s)	13330	13330	18670

Sample Rate: 40 PTS/Sec

PSD Readings:

Normal (V)	Normal (um)	Normal (uN)
0.01342	0.01342	0.01342

Lateral (V)	Lateral (rad)	Lateral (uN)
0.00012	0.00012	0.00012

Voltage Readings:
Shunt Voltage (V): -0.0079
Shunt Current (A): -0.0079
Probe Voltage (V): 0.74416
Optical Voltage (V): 0.10201

Scan size (um): 0
Frequency (Hz): 0.08
Cycles: 1
Scan axis: X

Set Axis:
Axis Selection: X
Velocity (um/s): 13330
Target (um): 1

Save raw data?
Note

Step Move:
Direction: Z+
Size (um): 1
Steps: 0

DAQ Status: status ✓, code 0, source
VISA Status: status ✓, code 0, source

Figure 2.7: Mesoscale friction tester virtual instrument control panel

There are seven data channels in the data acquisition system, which tracks the laser intensity, PSD normal and lateral voltages, shunt voltage, probe voltage, optical voltage, relative humidity, and temperature. The data channels can be configured to a voltage range with 16-bit resolution (65,536 subdivisions). For quantitative probe measurements, calibration values for the normal/lateral voltage to deflection/twist and deflection/twist to force as well as the circuit resistance are required to be entered in the control panel setup (Appendix A.1).

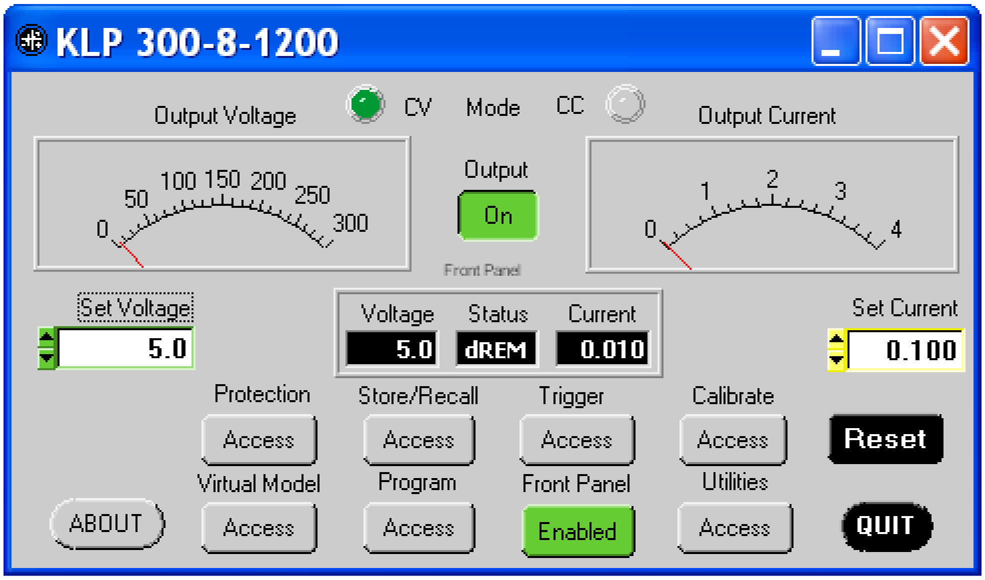

Set Voltage 5.0

Voltage 5.0

Status dREM

Current 0.010

Set Current 0.100

Figure 2.8: Kepco power supply virtual instrument control panel

Separate virtual instrument control panels adjust the voltage on the Kepco Model 300-8-1200 Power Supply (Fig. 2.8), Newport 20025 stepper motor stage, and Panasonic GP-KR222 camera as desired. The Kepco power supply can be operated in either constant voltage (CV) or constant current (CC) mode.

2.1.6 Auxiliary equipment

Additional equipment is used with the MFT for secondary objectives. An Omega Digital Thermo-Hygrometer records the environmental parameters of relative humidity and temperature, displaying this on the common virtual instrument panel (Fig. 2.7). Imaging of the probe and substrate is done on a Panasonic GP-KR222 camera with the aid of an Intralux 6000 light source. The camera is controlled via a separate computerized application (Fig. 2.9).

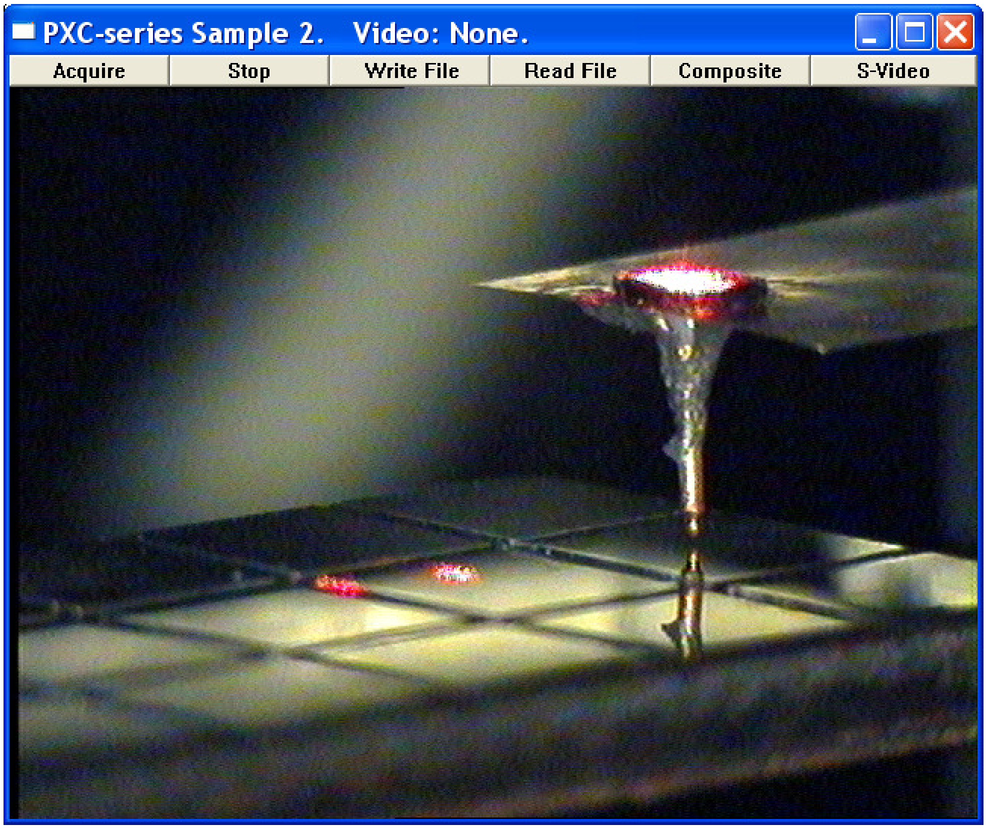

Figure 2.9: Panasonic camera view of copper substrate as it approaches copper probe

2.2 PROBE FABRICATION

An electrically conductive probe is attached to the free-end of the cantilever beam in the Mesoscale Friction Tester (MFT). The metal probes are wire segments with the tip formed to be both smooth (root mean square, or RMS, roughness on the order of subnanometer [6] to submicrometer) and round (with a radius of curvature on the order of 100 micrometers or less) by an electrochemical etching and polishing process. Advantages of this geometry include repeatability of fabrication, a common region of interaction for contact and arcing experiments that is independent of orientation, and ease of computational modeling due to it being predominantly defined by the radius of curvature parameter. The probe's aspect ratio – the length of the tip to the diameter of the wire – decreases as a function of time in the etching process. The advantage of forming a small radius of curvature is the ability to obtain current densities experienced in the rail-armature interface, on the order of 10^{10} A/m^2 [1]. However, at 10^{12} A/m^2 welding can occur on the contact region.

The radius of curvature was calculated through the Datatrend Software program *Grab It!* v1.41 that runs as a Microsoft Office Excel macro. Profile coordinates from a high-resolution scanning electron microscope (SEM) image of the probe tip in an upright orientation were fit to a parabola (Fig. 2.10) of form:

$$y = ax^2 + bx + c \tag{2.6}$$

where the radius of curvature

$$R = \frac{1}{2a} \tag{2.7}$$

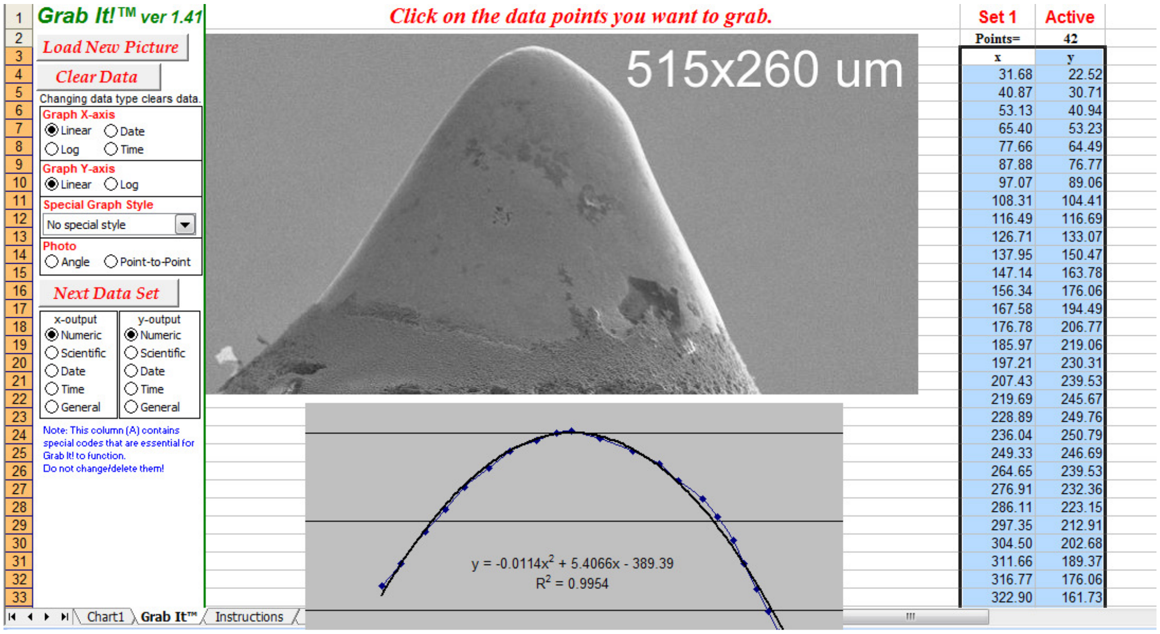

Changing data type clears data.

Graph X-axis
● Linear ○ Date
○ Log ○ Time

Graph Y-axis
● Linear ○ Log

Special Graph Style
No special style

Photo
○ Angle ○ Point-to-Point

x-output
● Numeric
○ Scientific
○ Date
○ Time
○ General

y-output
● Numeric
○ Scientific
○ Date
○ Time
○ General

Note: This column (A) contains special codes that are essential for Grab It! to function. Do not change/delete them!

Set 1	Active
Points=	42
x	y
31.68	22.52
40.87	30.71
53.13	40.94
65.40	53.23
77.66	64.49
87.88	76.77
97.07	89.06
108.31	104.41
116.49	116.69
126.71	133.07
137.95	150.47
147.14	163.78
156.34	176.06
167.58	194.49
176.78	206.77
185.97	219.06
197.21	230.31
207.43	239.53
219.69	245.67
228.89	249.76
236.04	250.79
249.33	246.69
264.65	239.53
276.91	232.36
286.11	223.15
297.35	212.91
304.50	202.68
311.66	189.37
316.77	176.06
322.90	161.73

Figure 2.10: Probe tip fitted to parabola to calculate radius of curvature

2.2.1 Electrochemical etching and polishing

The roughness and radius of curvature achieved through electrochemical etching and polishing are dependent on the material used. For example, copper probes will be rougher than tungsten as a result of taking shorter periods of time to process given the same voltage. Lower voltages result in a smoother probe. Previous work on copper probes [7] using voltage potentials ranging from 5 - 14 V and immersion depths of -0.2 to +0.4 mm had a range of radii from 5 - 278 μm.

Voltage (V)	Radius of curvature (μm)	Time Range (s)
5	43, 44, 74, 104, 156	600 - 750
8	18, 23, 32, 32, 34, 48, 114	350 - 390

Table 2.1: Radius of curvature for twelve copper probes under different etching voltages

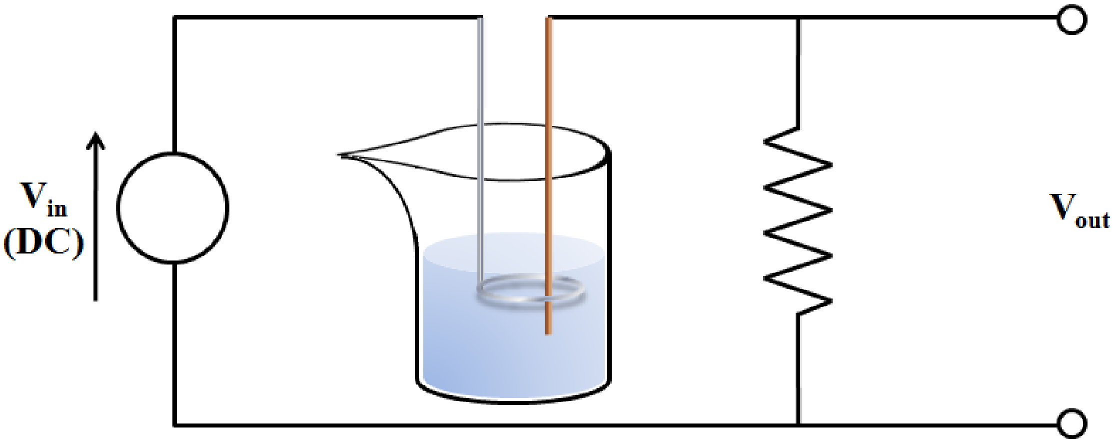

Figure 2.11: Electric circuit diagram for probe electrochemical etching

The electrochemical etching process involves lowering metal wire into an aqueous solution until a meniscus forms around the wire. An aqueous solution of 3 grams EM Science potassium hydroxide (KOH) per 30 mL distilled water (1.78*M*) was used for etching Goodfellow 99.95% pure tungsten wire with 0.2 mm diameter [6]. For etching Arcore AWG 24 (0.511 mm) bare copper wire, the aqueous solution used is 5 grams of Acros Organic pure phosphoric acid (H_3PO_4) per 30 mL distilled water. The wire with meniscus around it is enclosed by a cathode wire loop (tungsten and copper etching will utilize platinum and steel loops, respectively) of diameter 1 cm (Fig. 2.11). A constant voltage potential is applied through the wire loop and the ensuing electrochemical reaction dissolves the wire where it is in contact with the solution (Fig. 2.12, 2.13). The current will increase throughout the etching process. Considerable asperities are left on the probe due to inhomogeneities, such as microstructure and crystallographic orientation, and causes selective dissolution [6]. A constant etching voltage is provided by a Tektronic PS280 DC Power Supply and a Fluke 26 Series III Digital Multimeter is used to monitor the electric current.

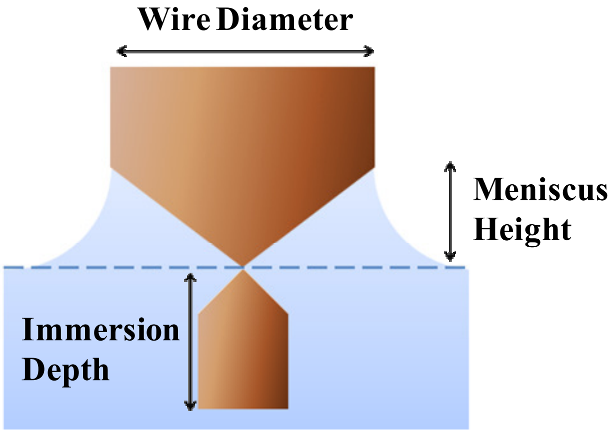

Figure 2.12: Schematic of wire in late stage of electrochemical etching process

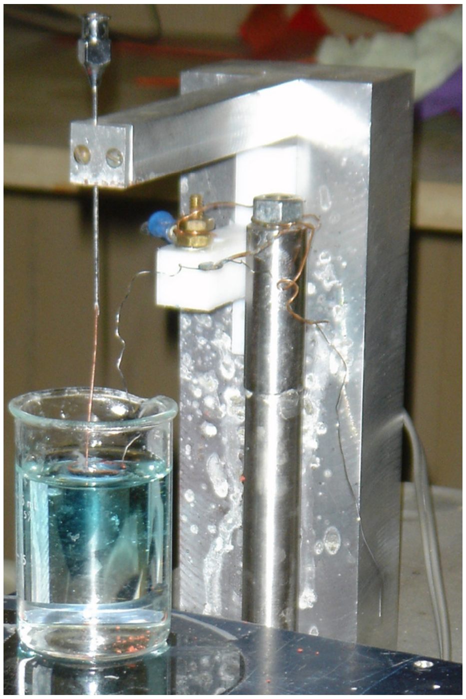

Figure 2.13: Electrochemical etched copper in aqueous solution

The electrochemical polishing process, at a constant current, as its name implies, reduces surface roughness. If there is sufficient depth of wire immersed in the aqueous solution, then necking can occur (Fig. 2.12) where the bottom portion will break-off after its weight surpasses the tensile force [7]. If the wire is immersed on the order of its radius or less, there will be no drop-off, and very smooth probes can be fabricated [6].

2.2.2 Cantilever beam and probe mounting

Following the electrochemical processes on the probe tip, the wire is cut to leave a probe of length one centimeter or less. Foreign materials that may have attached itself to the probe are removed using an L&R Quantrex 70 1QT Ultrasonic cleaner. Viewing the probe tip on a Microstar America Optical One Ten microscope can quickly assess probe geometry.

The cantilever beam is constructed using Precision Brand thick tempered and polished stainless steel feeler gage of 12.7 mm width. For laser measurements on the PSD, a polished silicon reflector on the order of a few millimeters is adhered to the free end of the beam opposite where the probe will be mounted. The end of the probe that was not electrochemically etched has Permatex Cold Weld bonding compound #14600 applied before pressing it against the underside of the steel beam to cure. The cold weld bonding uses a two-part epoxy solution that is equal concentrations of welding agent and hardening agent that must be thoroughly mixed. After the epoxy cures, the shear strength on steel is in excess of 20 MPa. Electrical conductivity between the probe and substrate requires a coating of M.G. Chemicals Nickel Print #840 connecting the base of the probe and the cold weld epoxy to the steel cantilever beam. The nickel print resistivity is $2.54 \cdot 10^{-5}$ Ω m.

2.3 SUBSTRATE PREPARATION

The substrate would be the interacting material for the probe tip and each sample consisted of an elemental metal plate on the order of a few centimeters across. In order to observe the contact effects like wear and arcing from the probe on the substrate, a grinding and polishing procedure was utilized prior to testing to remove asperities. A grid with 4 cm^2 enclosed regions or smaller (Fig. 2.9) was drawn or engraved onto the surface to aid in microscopy. The substrate rests upon an insulating base on top of the Mesoscale Friction Tester (MFT) stage. A wire connects the electric circuit to the substrate (Fig. 2.6), closing the circuit only when current passed between the substrate and probe.

2.3.1 Epoxy base

The addition of a bonded epoxy base to the metal plate aids the grinding and polishing procedure. The substrate was placed at the bottom of a hollow cylindrical container that had been swabbed with Buehler Release Agent #20-8185-002. Buehler epoxide resin #20-8130-128 was mixed with Buehler epoxide hardener #20-8132-032 using a 5:1 weight ratio and then poured over the substrate. Before the epoxy cured, air bubbles could be removed by placing the hollow cylinder in a vacuum chamber for 10-15 minutes. The epoxy base also acts as an electrical insulator so as to decouple the probe-substrate system from the rest of the apparatus.

2.3.2 Grinding and polishing

A series of grinding and polishing discs at 200 revolutions per minute were used on a Buehler EcoMet 3 Variable Speed Grinder-Polisher to grind off the surface layers of the substrate and remove most asperities through a refined polishing process. Allied High Tech Products, Inc. silicon carbide (SiC) abrasive discs #50-10065, #50-10075, and #50-11077 were used with 320, 600, and 1200 grit (grating of 35 μm, 15 μm, 5 μm), respectively, and water coolant. Polishing with Allied High Tech Gold Label #90-150-210 diamond (3 μm) and Vel Cloth # 90-500-400 diamond (1 μm) used a Green Lube Polishing Lubricant #90-209010. The final stage used Allied High Tech Chem-Pol #180-20015 colloidal suspension silica (0.05 μm). Each stage of the process had a 1-2 minute duration and mounting pressure was applied to the substrate in a complementary rotation with the disc. The surface was observed using an optical microscope before experiments to verify a surface without preexisting features. The substrate rms roughness was 10 nm.

2.4 ENVIRONMENTAL EFFECTS

To understand better the role of environment as it relates to the rail-armature interface, the Mesoscale Friction Tester (MFT) is capable of passively monitoring or actively altering these parameters. There is significant room for future research in the interaction between probe and substrate when varying environmental effects. This may be accomplished with additional modifications to the MFT, such as the addition of an airtight container and a vacuum system to facilitate a pure atmosphere environment.

2.4.1 Vibration reduction

External vibration to the MFT can oscillate the cantilever beam and add significant noise to the force measurements. To mitigate vibrations from foot traffic, the MFT is physically located at the basement of the laboratory building and is two rooms separated from the hallway. The MFT is supported by a TMC 63-533 High-Performance Vibration Isolation Lab Table (Fig. 2.1). Air convection is reduced by a steady room temperature and placing a box over the MFT apparatus. A Panasonic GP-KR222 camera with the aid of an Intralux 6000 light source can record images of the probe and substrate through a window in the box.

2.4.2 Argon gas

Experiments with an argon-rich atmosphere in the MFT were conducted to measure its effects on electrical arcing between the probe and substrate. A Praxair, Inc. 8.6 m^3 compressed gas cylinder of 99.997% pure argon was connected to a Union Carbide Corporation High Pressure Purifier #6140 with 20.7 MPa maximum inlet pressure and a Victor Equipment Company Model #FM 150CW gas flowmeter to display the rate of volume output. A pressure gauge monitored the quantity of argon remaining in the cylinder. After exiting the flowmeter, the argon gas passed through a bubbler with water to maintain stable humidity levels as it entered the container housing the MFT (Fig. 2.14). The gas was released at sufficient distance from the cantilever beam that flow did not lead to unintended oscillations.

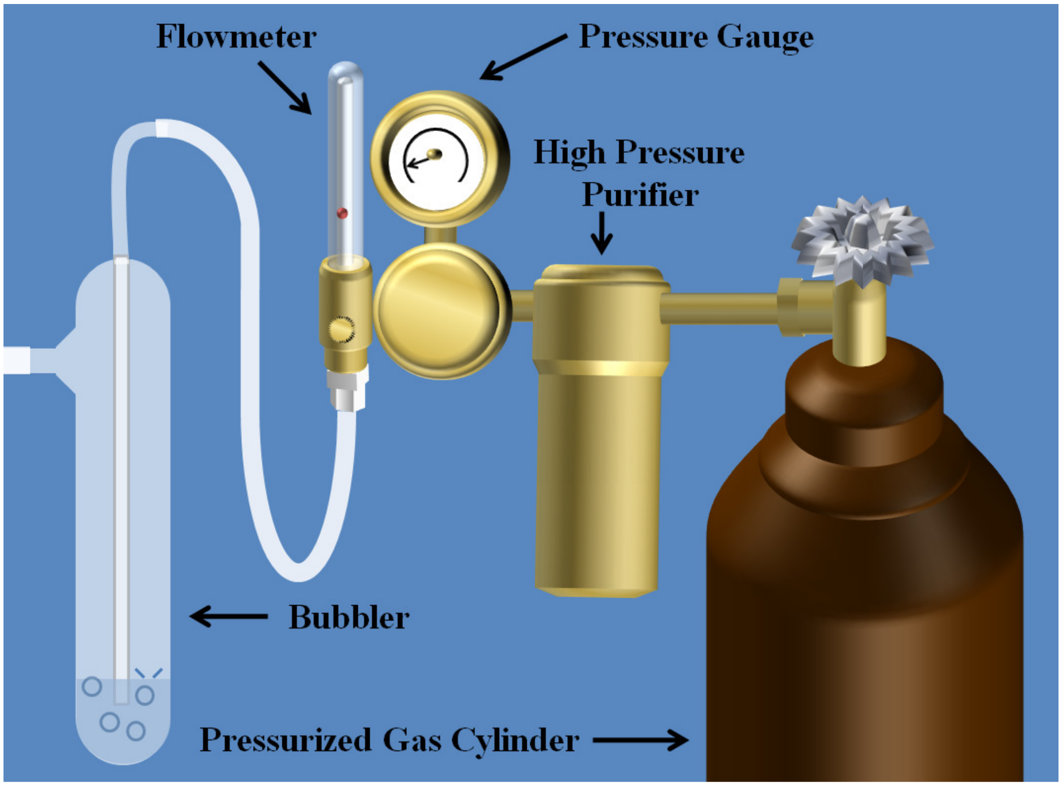

Figure 2.14: Apparatus for gas intake to mesoscale friction tester

2.4.3 Humidity control

The temperature and relative humidity were measured using an Omega Digital Thermo-Hygrometer and viewed on the virtual instrument display (Fig. 2.7). Year-round temperature for all experiments was within 23-27 °C. Changes in relative humidity could lead to signal drift in force measurements on the MFT. The desiccant Drierite (anhydrous $CaSO_4$) CAS #7778-18-9 is used for reducing excessive humidity. In the experimental case of a gas environment other than air, a bubbler was used to channel the dry gas from the cylinder through water before entering the MFT area. Rapid changes in humidity in the MFT, as with releasing dry argon gas, interfered with accurate readings. The exact gas concentrations were unknown and time-dependent without a vacuum seal on the MFT box containment or pump system.

2.5 MICROSCOPY

Several forms of microscopy were used to obtain images and quantitative information about the probe, substrate, and contact effects. Due to the difficulty involved with the elliptic geometry of the probe tips, the substrate was preferred for analysis of arcing and solid-solid contact erosion. The substrate had advantages of both a flat surface for simple tilt adjustment and space for multiple testing locations that can be analyzed individually.

2.5.1 Scanning electron microscopy (SEM)

Scanning electron microscopes (SEM) operate in a vacuum on conductive specimens and use backscattered and secondary electrons to determine composition and topographical information. The large depth of field means near and far regions can be simultaneously in focus and very high magnification and resolution can be obtained.

A LEO 1530 Thermally-Assisted Field Emission (TFE) Scanning Electron Microscope was used for high-resolution images of the probe tip in order to evaluate radius of curvature. The high magnification also enabled viewing of effects from arcing experimentation at the probe tip and verified the RMS roughness was sub-micrometer for copper (see Chapter 4 for images) and sub-nanometer for tungsten (Fig. 2.15, 2.16) [6]. This SEM also allowed for large sample analysis (up to 15 cm across) which aided in rotation of the probes bonded to cantilever beams for the possibility of a nearly circumferential view of the probe tip.

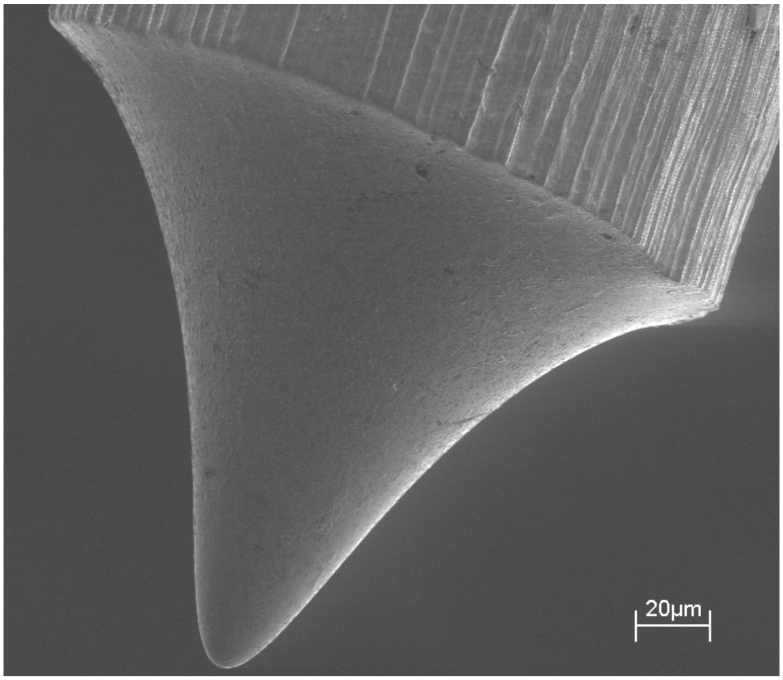

Figure 2.15: Tungsten probe tip for aspect ratio and radius of curvature determination, secondary electron image at 1170x, 25 mm WD, and 10 keV beam voltage

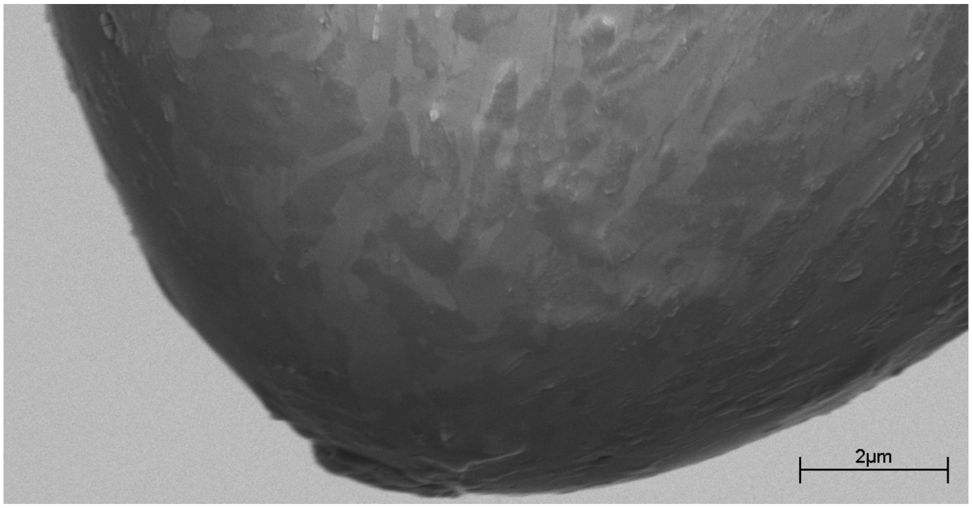

Figure 2.16: Tungsten probe tip for surface roughness and radius of curvature determination, in-lens signal image at 27550x, 5 mm WD, and 10 keV beam voltage

2.5.2 Atomic force microscopy (AFM)

Atomic force microscopy (AFM) has a similar procedure to that used for the MFT with exceptions of all measurements made between contact of tip and sample, are at smaller contact radii and forces, and that the probe scans the stationary sample. AFM offers excellent quantitative topographical resolution, but has disadvantages in artifacts from thermal drift and steep geometries that the probe cannot transverse.

A ThermoMicroscopes Autoprobe M5 atomic force microscope was used to assess the arcing erosion on copper substrates by imaging a topographical layout of the ablation site and its vicinity. The depressions formed from arcing were often too deep for quantitative information to be obtained. An optical profiler was utilized to resolve this issue.

2.5.3 Optical microscopy

Optical microscopy was used for true-color imaging of substrate contact surfaces. The Nikon Eclipse TE2000-U had six objective lenses of magnification 4x, 10x, 20x, 40x, 50x, and 60x. Software on a Dell OptiPlex GX400 workstation added size scaling information to digitally acquired images.

2.5.4 Optical profiler

Optical profiling uses light interference to model the surface geometry. The WYKO Rough Surface Tester-Plus Optical Profilometer is operated on a Dell Dimension XPS P90 computer with WYKO Vision for RST Plus software. The rough surface VSI mode could measure step sizes as small as 160 nm. The WYKO dataset surface profile information is recorded as a block file under a proprietary .opd format extension. The data was transferred to more manipulatable format using the DOS block to ASCII converter program blk2asc.exe. The numerical computing program Matlab 7.8.0 R2009a was used to make data analyses, such as correcting for global tilt of the specimen or calculating material volume above and below the surface mean that may have been transported as a result of arcing or friction between the probe and substrate.

Chapter 3

Paschen Curve

3.1 INTRODUCTION

The behavior known as Paschen's Law was introduced in 1889 by German physicist Friedrich Paschen. The law states that the breakdown voltage, the potential at which an insulating gas becomes conductive, is a function of the product of the pressure and separation distance [8]:

$$V = \frac{a(pd)}{\ln(pd) + b} \tag{3.1}$$

where:

a, b: coefficients dependent on gas

p: gas pressure

d: distance separating electrodes

Setting the derivative $\frac{dV}{d(pd)} = 0$, the minimum voltage for arcing to occur is:

$$V_{\min} = ae^{1-b} \tag{3.2}$$

The dominant physical mechanism for this breakdown voltage is through a Townsend avalanche of ionized gas. Both the minimum voltage and the corresponding pressure-distance product at this minimum are determined by the gas (Fig. 3.1).

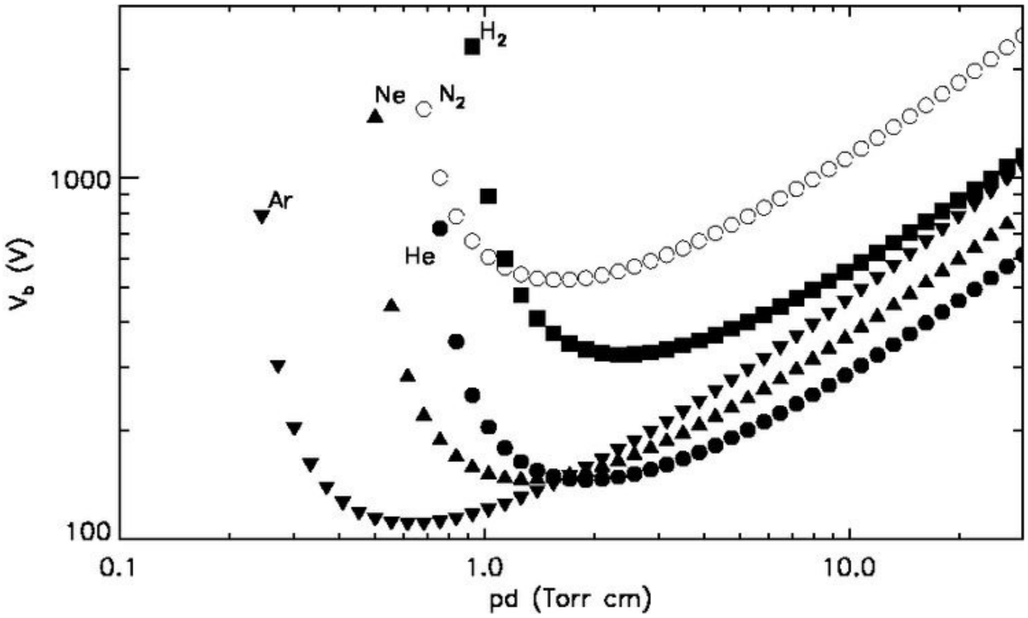

Figure 3.1: Paschen curves for hydrogen, helium, nitrogen, neon, and argon [9]

In the present work, only the gap distance between the probe and substrate electrodes was varied since the Mesoscale Friction Tester (MFT) does not have the capability to change the pressure. The MFT apparatus was used to examine arcing at distances on the order of 10 μm and below, and large deviations from the classical Paschen curve (Figure 3.1) were observed. Field emission of electrons becomes the dominant physical mechanism at gaps smaller than approximately 5 μm and tunneling of electrons is the defining process at gaps smaller than 2 nm. Thus, when operating with distances on the order of a few micrometers, a modified Paschen curve must be used to account for the different physical processes. The modified curve increases voltage with distance in a linear fashion at lower values and then enters a transition region before merging with the classical Paschen curve [10].

3.2 AIR AT ATMOSPHERIC PRESSURE

The Mesoscale Friction Tester (MFT) was used to determine the Paschen curve for air at micrometer-scale distances and atmospheric pressure. The electric circuit was modified for the probe to act as a cathode (Fig. 2.4) or anode (Fig. 2.5). In a typical experiment, the probe-substrate system is initially brought to a known gap in the range of 0.2 to 15 μm. The power supply was then switched on and maintained at a constant voltage. The gap between the probe and substrate was then decreased and increased at a constant speed by translating the PZT in the vertical direction by an amount that was slightly larger than the initial gap. This ensures establishment of contact at some point in the cycle. Both the normal force and the voltage drop across the fixed resistor (Fig. 2.4, 2.5) were monitored as a function of time. A typical result of such an experiment is shown in Figure 3.2. From this figure, it is clear that current flow was established well before a normal force was observed, implying that an arc or a similar noncontact mechanism must have been established to transport current. The current, initiated by the electrical arc, passing between the probe and substrate would continue as the PZT stage cycled from approach, contact with the probe, and then began to retract. As the substrate pulled back from the probe, hysteresis was observed in that distance at which the current quenches was significantly greater than the gap distance required for it to initiate arcing.

From a collection of such experiments with different initial gaps and voltages, a curve of the variation of the voltage versus gap distance is obtained for onset of arcing and for the quenching (Fig. 3.3). The following observations are made from these measurements:

- The variation of arcing voltage with gap distance is significantly different from the traditional Paschen's curve shown in Figure 3.1; this will be referred to as the modified Paschen's curve, although the mechanism of breakdown may be quite different.
- Some segments of the modified Paschen's curve for air at atmospheric pressure had a greater breakdown voltage (Fig. 3.3) when the copper probe was acting as a cathode on the copper substrate than as an anode, possibly due to asymmetry of the geometry.
- The quenching distance for the anode probe indidicates that, with increasing voltage, quenching of the arc occurs at a gap distance several times larger than the gap distance that initiated arcing. Plasma discharge is one highly non-linear system that is expected to exhibit this kind of hysteresis [11].
- If current density was sufficiently great, the probe would spot weld onto the substrate and require an impulse from the stage to detach.

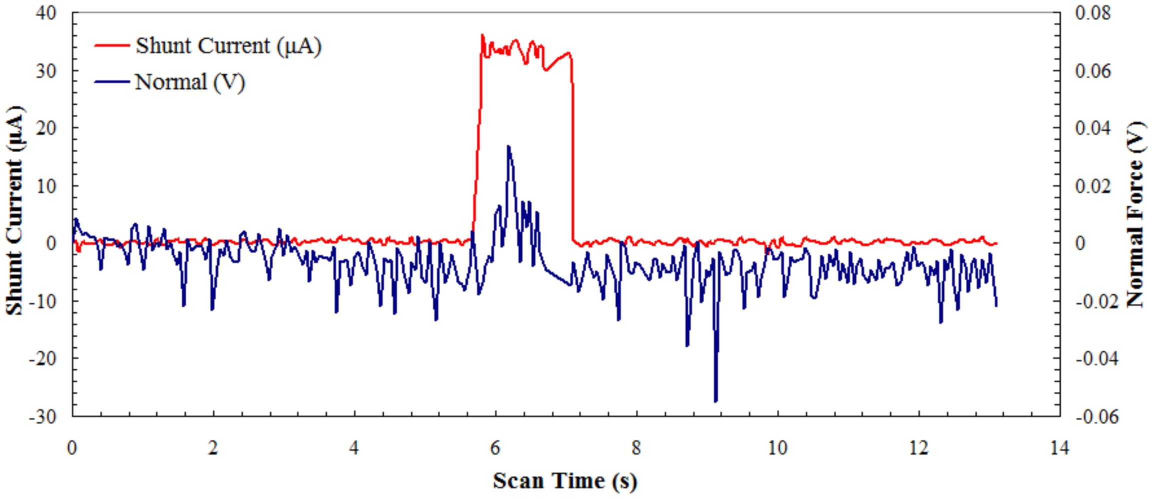

Figure 3.2: Normal force voltage and shunt current without arcing, from a supply voltage of 40.4 V and a vertical scan range of 5.0 µm

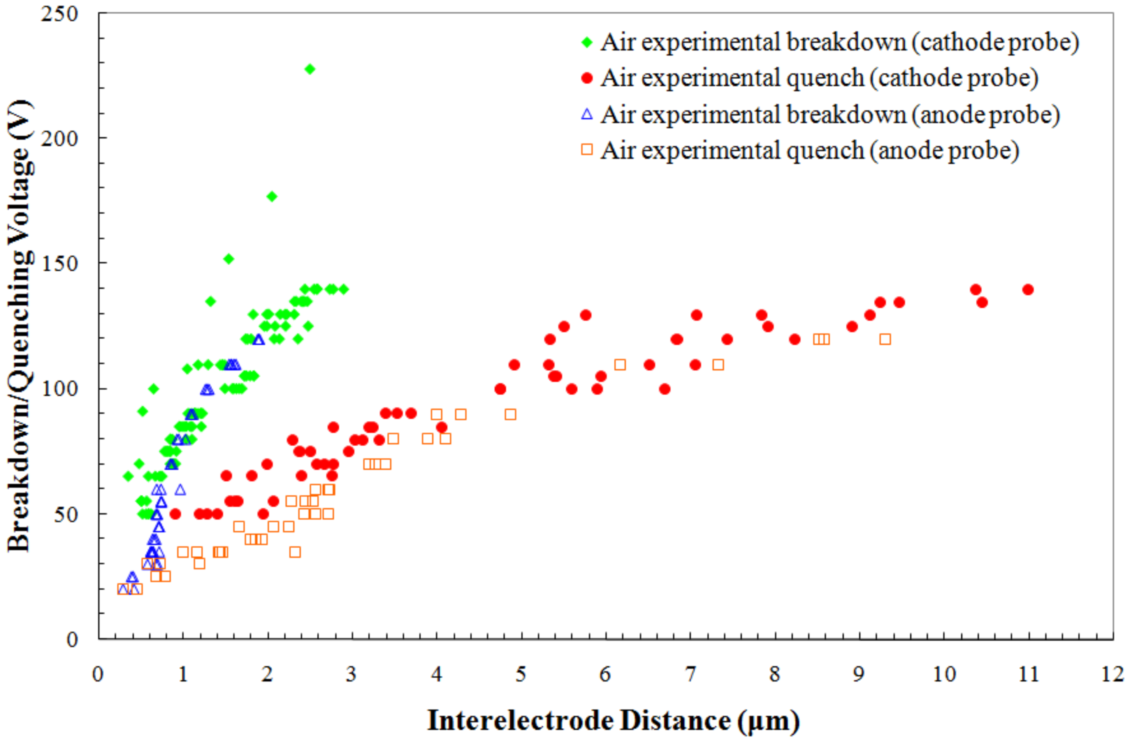

Figure 3.3: Paschen curve for breakdown voltage in air at atmospheric pressure

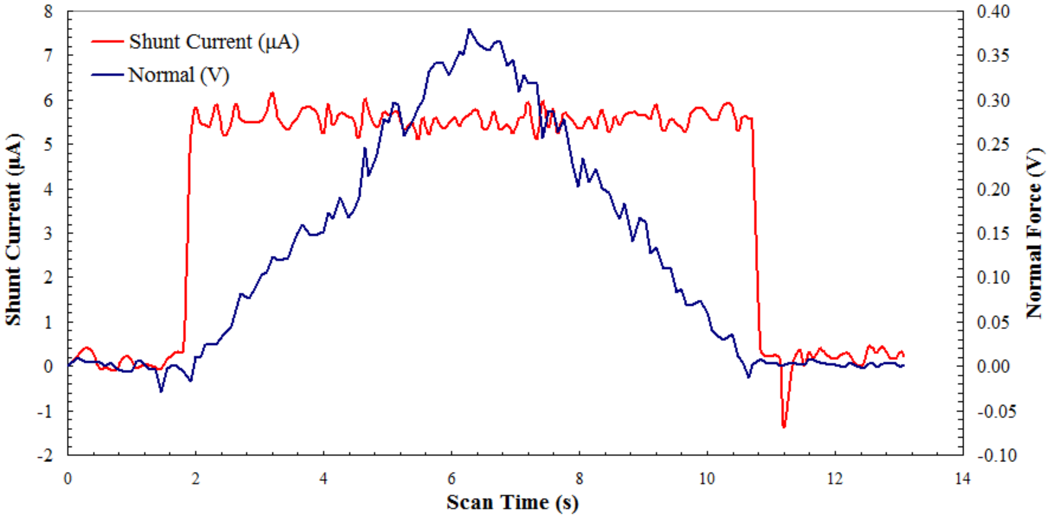

Figure 3.4: Normal force voltage and shunt current without arcing, from a supply voltage of 6.0 V and a vertical scan range of 6.0 µm

Voltages had to be sufficiently high for current to pass between the probe and substrate without a change in the beam deflection, indicating a minimum voltage must be obtained regardless of distance. Thus, the Paschen curve is not defined for low-voltage or low-distance values. As the scan range is equal approaching and retracting, the distance of closest approach between the probe and substrate was in the middle of the scan time. If this voltage was not above a critical value, the change in deflection matched the onset of current and no hysteresis was observed (Fig. 3.4). The shunt current i and normal force N are related to the shunt voltage V and normal force voltage V_N by a coefficient:

$$i = \frac{V}{R} \tag{3.3}$$

where $R = R_f + \mathrm{R}_v$ from the electric circuit resistor and potentiometer, and

$$N = \frac{V_N}{\kappa_N} \tag{3.4}$$

where κ_N is the calibration factor based on the beam dimensions (Appendix A.2)

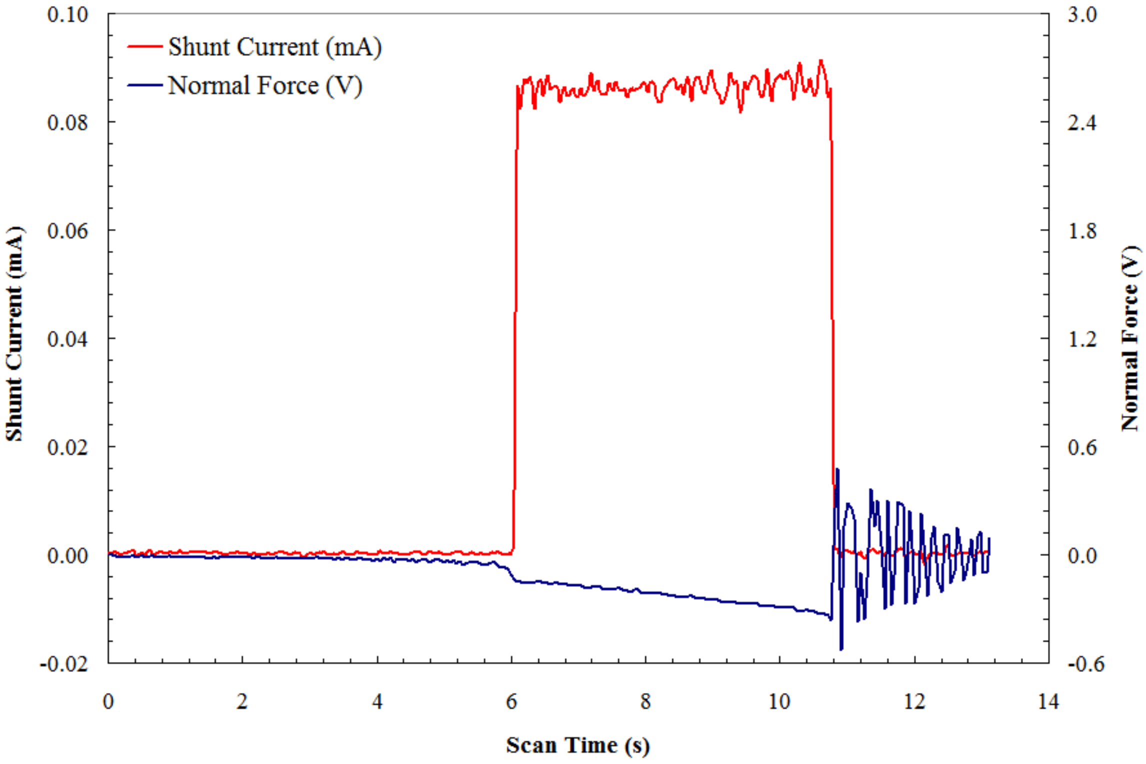

Figure 3.5: Shunt current and normal force voltage with electrostatic attraction, from supply voltage of 105.2 V and a vertical scan range of 6.0 μm

In the case of a cathode (negative) probe, electrostatic attraction was observed where the probe behaved as if it was attracted to the oppositely charged substrate and would deflect closer to the substrate during its approach (Fig. 3.5) until contact. Spot welding would often occur and the beam oscillation from breaking this bond is evidenced at the end of the scan time (Fig. 3.5).

3.3 ARGON AT ATMOSPHERIC PRESSURE

The modified Paschen curve for argon, an inert gas, was of interest to determine if this would have significant effect on the voltage necessary for arcing to occur. As arcing at higher voltages requires greater current, and this lies outside the domain encountered between the rail-armature interface, it may lead to a reduction in rail ablation.

The Mesoscale Friction Tester (MFT) was incapable of accurate measurements in a pure argon environment. For experimentation in a pure argon environment, the container would need to be sealed such that a vacuum pump system could remove the air, prior to filling with argon. In the present system, a steady-state air-argon concentration could not be obtained by varying the flow rate. Argon gas negatively affected the accuracy and reliability of PSD deflection measurements. The source of this error may be related to the relative humidity discrepancy of the air and argon. A high pressure purifier and bubbler (Fig. 2.14) were utilized, with limited success, in reducing the differences in relative humidity. Therefore, efforts to characterize breakdown in argon atmosphere were abandoned after numerous unsuccessful trials.

3.3.1 Comparison with computational simulation

The modified Paschen curve data for air was compared with the simulations of Albright et al. [11] that involved a self-consistent non-equilibrium plasma model to generate a computational breakdown curve for argon. The substrate was modeled as a flat electrode surface and the probe tip was represented by pin electrode with rounded tip and a diameter on the order of tens of micrometers.

The solver they used was a continuum (fluid) model (equations in Appendix A.3) which had a mean free path on the order of 0.1 μm and valid for the discharge regime of interest. Six species and 17 reactions considered by the finite-rate argon chemistry. Field emission of electrons was simulated with the Fowler-Nordheim equation. The model used results from literature for validation. The results of the computation are shown in Figure 3.6, along with a comparison to the experimental data obtained for air. The agreement between the simulations and experiments is quite good for the onset of arcing. The hysteretic response between establishment of arcing and quenching is also captured in the simulations, although the quantitative comparison is not so good. Computational values of the gap distance for quenching were not as large as those found from the experiments (Fig. 3.6) [11].

These experiments provide an important consideration from the point of view of applications to railguns: while the traditional Paschen's curve suggests that arcing cannot occur if the voltages are below the minimum $V_{\min} = ae^{1-b}$, the modified Paschen's curve indiciates arcing at very low voltages, when the gaps are small. This is precisely the regime in which the railguns operate and hence, one would expect arcing at the microscale and hence erosion. Erosion from microscale arcing is considered in the next chapter.

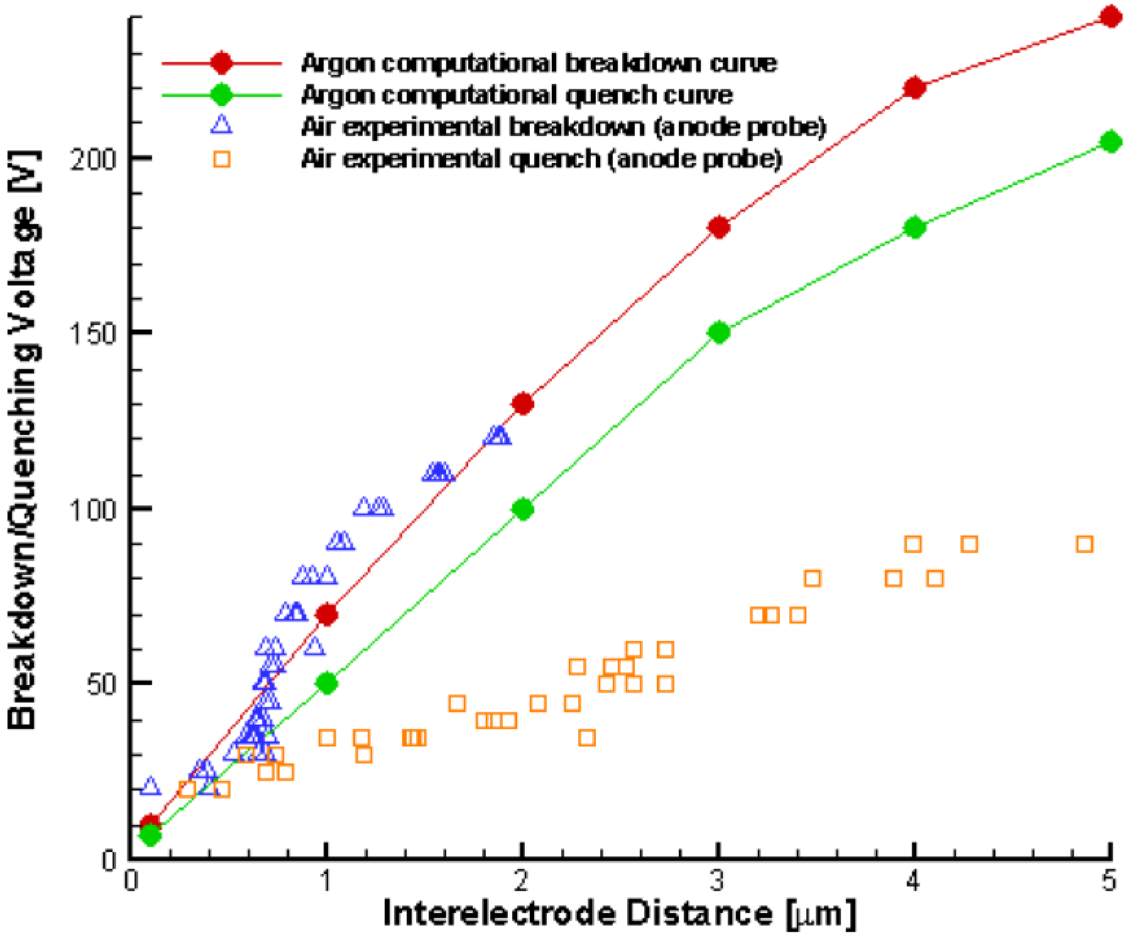

Figure 3.6: Experimental and computational plasma breakdown and quenching conditions for air and argon in small interelectrode distances at atmospheric pressure [11]

Chapter 4

Arcing Erosion

4.1 TOPOGRAPHY

The current density along the rail-armature interface is estimated to be on the order of 10^{10} A/m^2 [1]. Motivation to reduce arcing damage along the rails led to experimental simulation of this interface using a copper probe and copper substrate. Qualitative and quantitative surface data of the probe and substrate erosion was obtained as a function of voltage, number of discharges, dwell time, and overvoltage.

Several methods were employed to image these surfaces. These included scanning electron microscopy (SEM), atomic force microscopy (AFM), optical microscopy, and an optical profiler. An emphasis was placed on microscopy of the arcing effects on copper substrates due to its advantageous flat geometry. However, the probe tip arcing images offer the additional information of localized erosion and these are examined qualitatively.

4.2 EFFECTS OF VOLTAGE AND REPEATED DISCHARGES ON PROBES

A number of copper probes were electrochemically etched and polished (Table 2.1), and imaged on a scanning electron microscope (SEM) prior to any electrical arcing. These serve as the nominal surface with which to compare effects from arcing or sliding.

The SEM images also provided values of probe geometry such as aspect ratio and radius of curvature, allowing for a broader range of experimental parameters. Copper probes were fabricated with an etching voltage of either 5 V (Figs. 4.1, A.2-A.5) or 8 V (Figs. 4.2, A.6-A.11). Each SEM image includes the working distance (WD) used and had accelerating beam voltage of 10 keV.

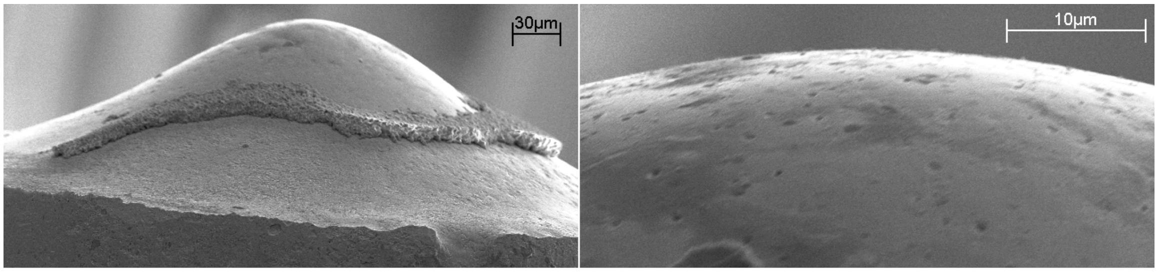

Figure 4.1: Copper probe tip etched at 5 V with 104 μm radius of curvature: secondary electron images at 206x and 1800x, 11 mm WD

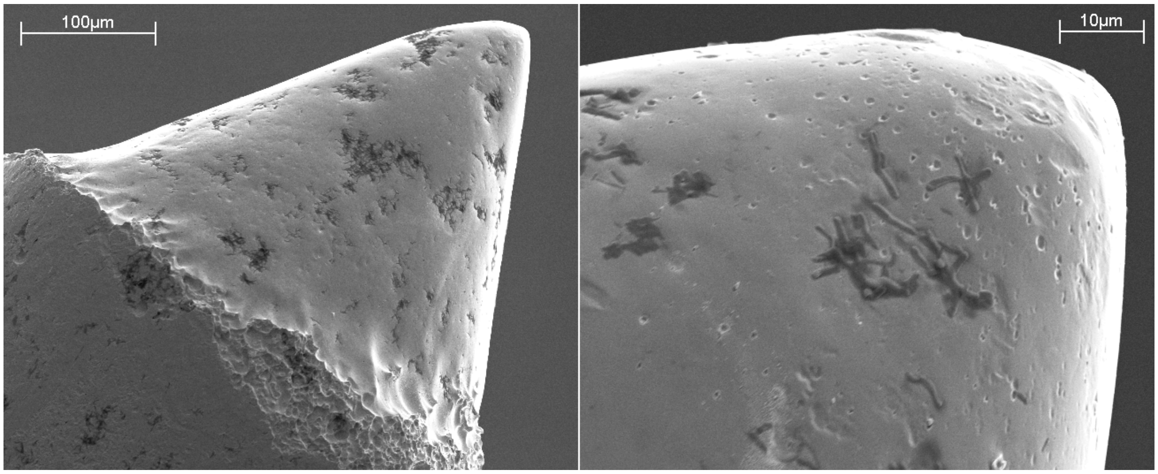

Figure 4.2: Copper probe tip etched at 8 V with 18 μm radius of curvature: secondary electron images at 174x and 1080x, 13 mm WD

Using voltages up to 120 V, several copper probes were brought to a distance for arcing to occur during a single vertical scan with the sample stage. This period of arcing, the dwell time, was on the order of a tenth to one second. SEM images revealed no noticeable differences between the copper probe tips before and after this short-duration single-arc except at the highest voltage used, where it appears to have smooth regions of material that may provide evidence for copper melting (Fig. 4.3). Note that Figure 4.3 is of the same probe from Figure A.8 and the "after arcing" image has some tilt relative to the "before arcing" image.

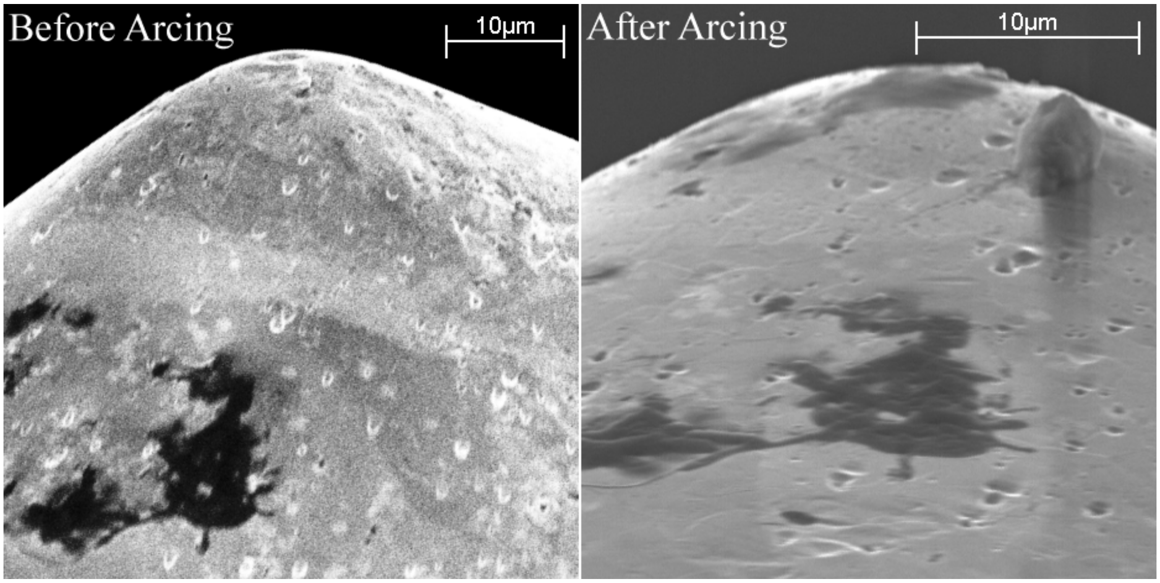

Figure 4.3: Copper probe tip etched at 8 V with 32 μm radius of curvature before and after one arc at 120 V: InLens and secondary electron images at 1090x and 6610x, 13 mm and 20 mm WD

In order to make arcing effects visible, the number of discharges that each probe tip received was increased by up to two orders of magnitude (Table 4.1). Whereas the effects on the probe tip surface with a single discharge at low voltage were not noticeable, the results of repeated arcing leads to a nearly circular region around the arc site that had a substantial temperature increase and leads to visible surface modification.

Figures 4.4 – 4.9 show SEM images of the multiple arc damaged probe surfaces; for the lowest voltage used – 5 V – the surface appears nearly unaltered even after 100 arc discharges (Fig. 4.4, 4.5). On the other hand, for higher voltage discharges, the arc causes surface modification over about 10 μm diameter region (Figs. 4.6-4.9). The determination of whether this circular area on the probe tip (Figs. 4.6-4.9) is crystalline or amorphous copper warrants further investigation. The use of an electron backscatter diffraction (EBSD) detector on a Philips/FEI XL30 Environmental SEM was insufficient for this purpose due to the small region of interest (diameter is on the order of ten micrometers), the probe's ellipsoidal geometry, and from oxides which can reduce signal since depth resolution is limited to 10-100 nm [12]. The flat and polished surface of the copper substrate may be much more amenable to the different microscopy techniques, but the surface modification on these may also evolve differently. Nevertheless, we look at the surfaces of the substrates subjected to multiple arc discharges.

Copper Probe Tip (etching voltage and radius of curvature)	**Applied Voltage (V)**	**Arcing Cycles**
8V, 23 μm	5	100
8V, 32 μm	20	23
8V, 18 μm	60	50
8V, 48 μm	100	50

Table 4.1: Copper probe tips with applied voltage and number of discharges

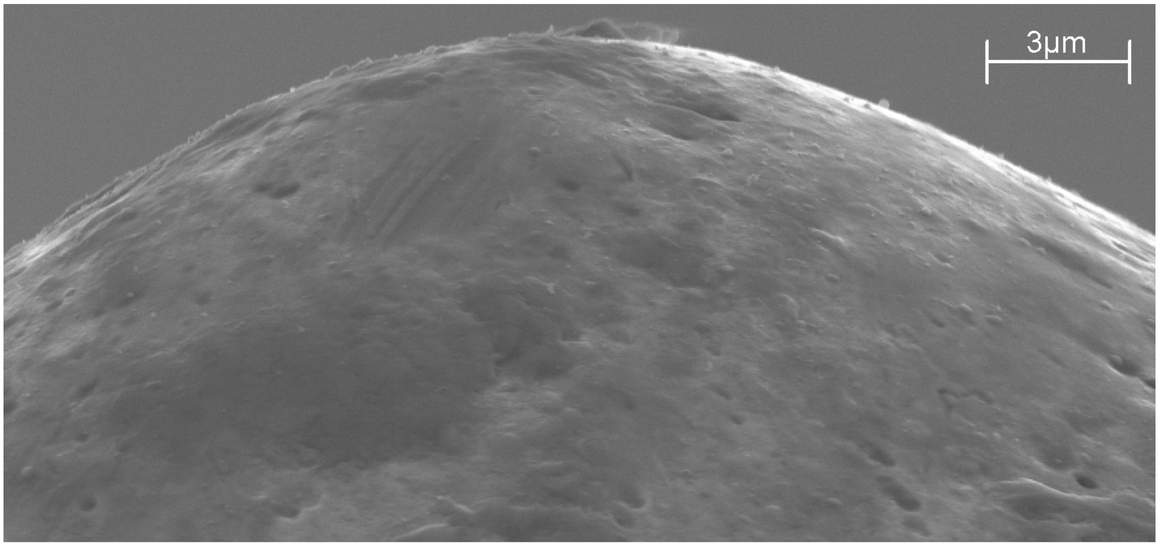

Figure 4.4: Copper probe tip etched at 8 V with 23 µm radius of curvature after 100 arcing cycles at 5 V: secondary electron image at 11340x, 9 mm WD

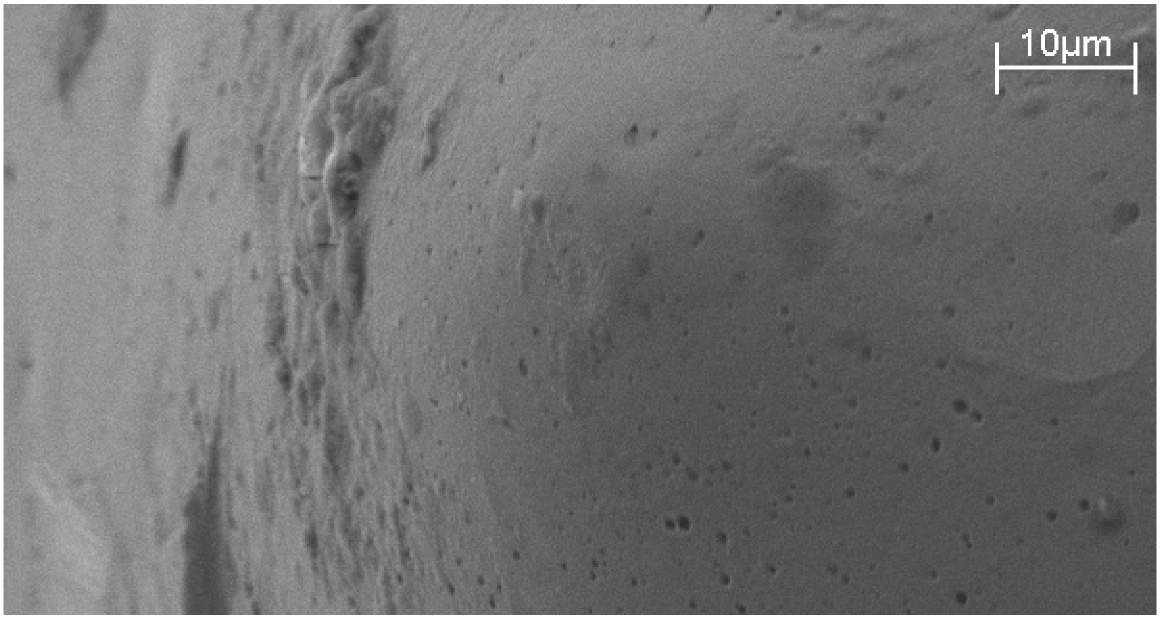

Figure 4.5: Copper probe tip etched at 8 V with 23 µm radius of curvature after 100 arcing cycles at 5 V: secondary electron image at 2650x, 10 mm WD

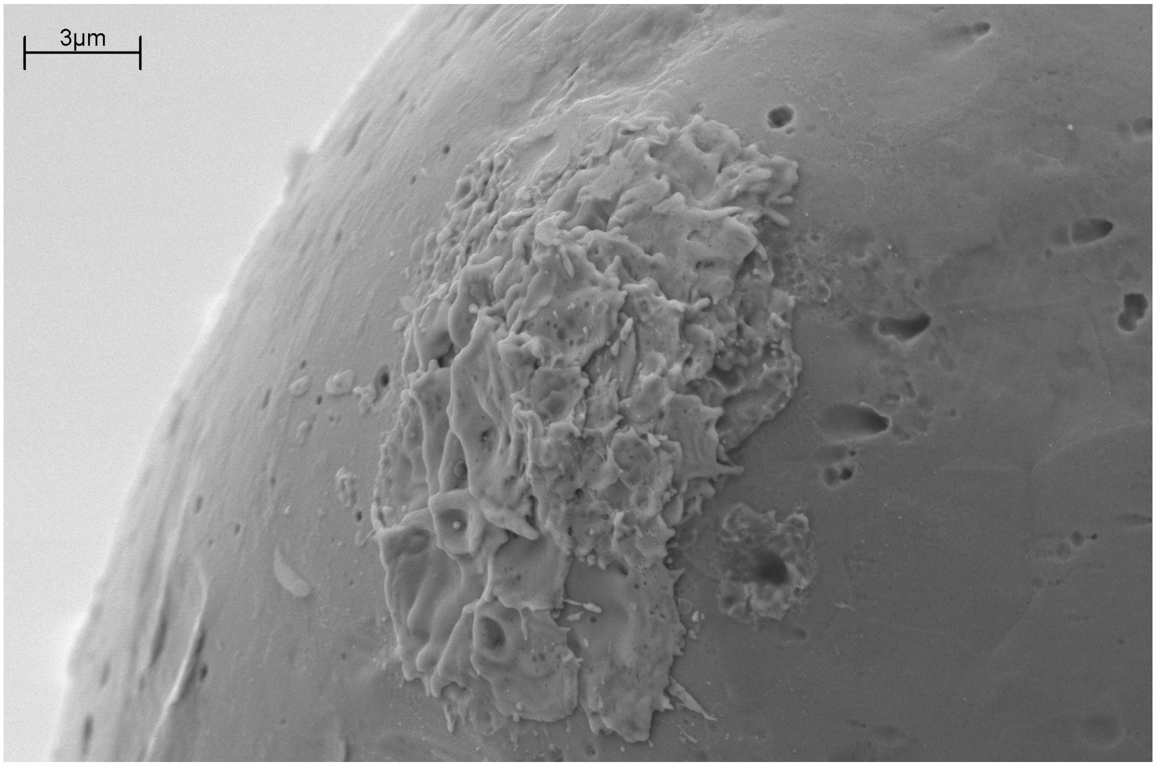

Figure 4.6: Copper probe tip etched at 8 V with 18 μm radius of curvature after 50 arcing cycles at 60 V: secondary electron image at 11340x, 9 mm WD

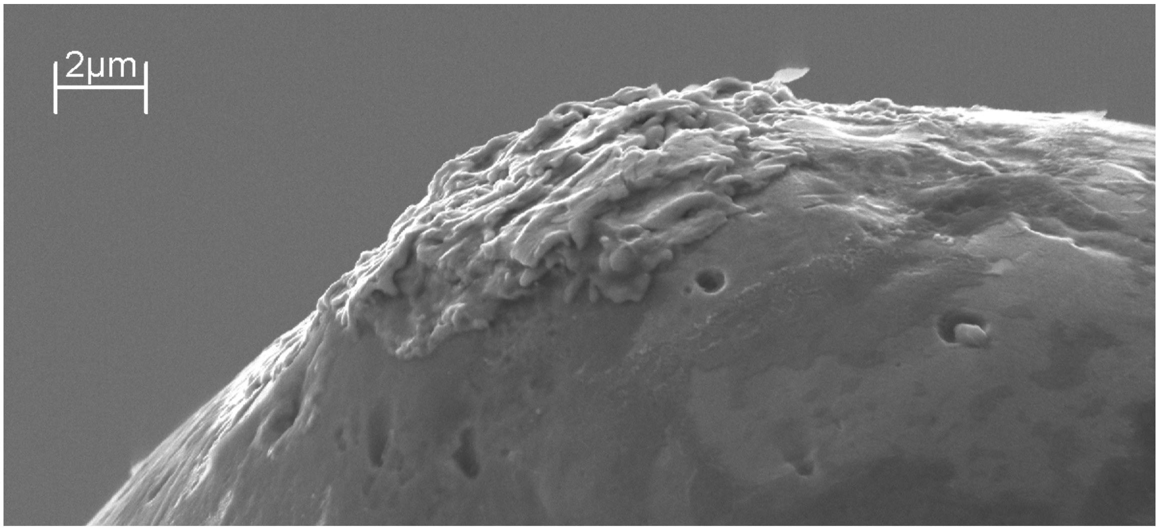

Figure 4.7: Copper probe tip etched at 8 V with 18 μm radius of curvature after 50 arcing cycles at 60 V: secondary electron image at 8680x, 16 mm WD

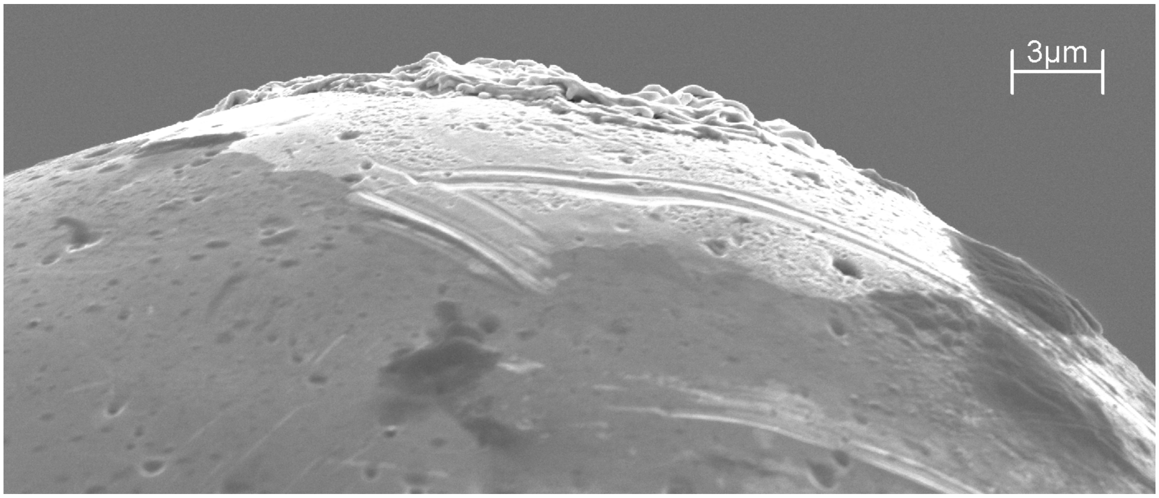

Figure 4.8: Copper probe tip etched at 8 V with 48 µm radius of curvature after 50 arcing cycles at 100 V: secondary electron image at 6740x, 16 mm WD

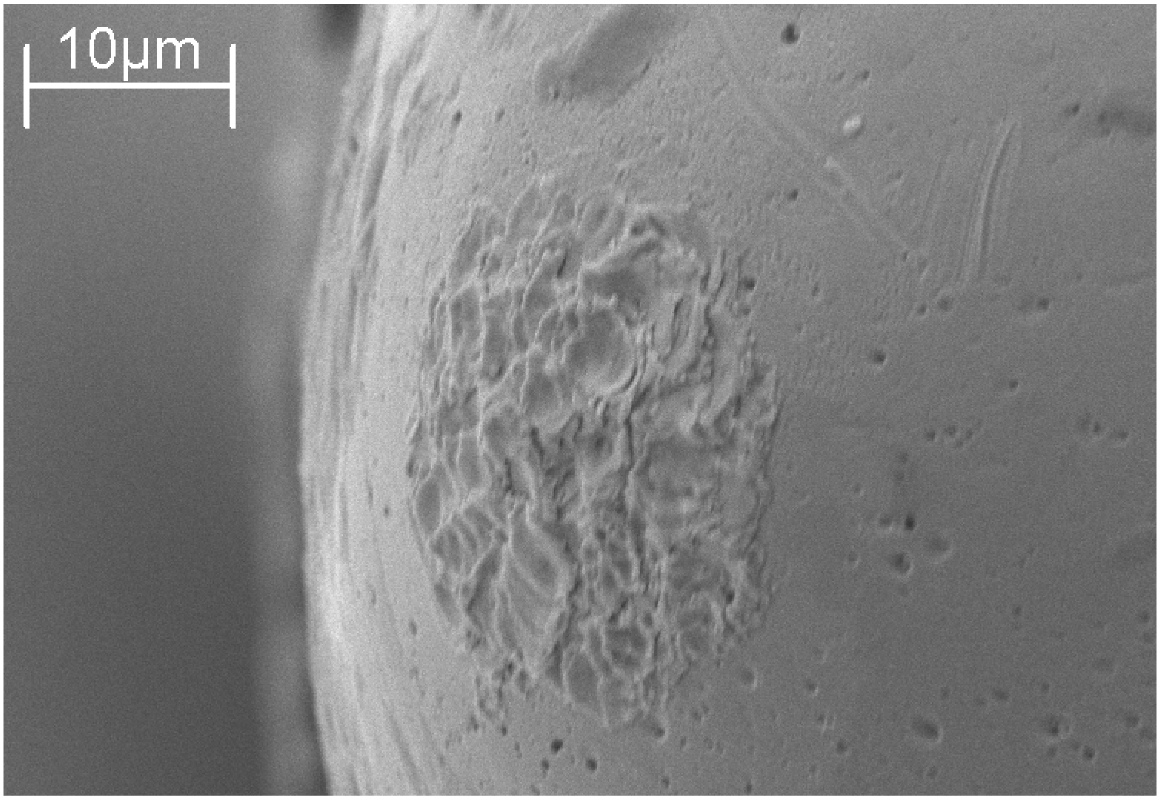

Figure 4.9: Copper probe tip etched at 8 V with 48 µm radius of curvature after 50 arcing cycles at 100 V: secondary electron image at 2460x, 10 mm WD

4.3 EFFECTS OF VOLTAGE AND REPEATED DISCHARGES ON SUBSTRATES

Repeated instances of arcing were applied on sections of copper substrates. The number of discharges and applied voltage affected the size of the depression or arc – erosion pit formed, and some of the material from the pit appears to have been displaced to a mound along the perimeter. Optical microscopy was utilized to obtain visual spectrum images of the arcing sites (Fig. 4.10-4.14). Discoloration was seen around the arcing sites, possibly due to oxidation after heating. Atomic force microscopy (AFM) was attempted as one way to obtain quantitative measure of the erosion pit, but this technique was limited by the steepness of the pits (Fig. 4.15); therefore, an optical profilometer was used to measure the topography (Figs. 4.16-4.20).

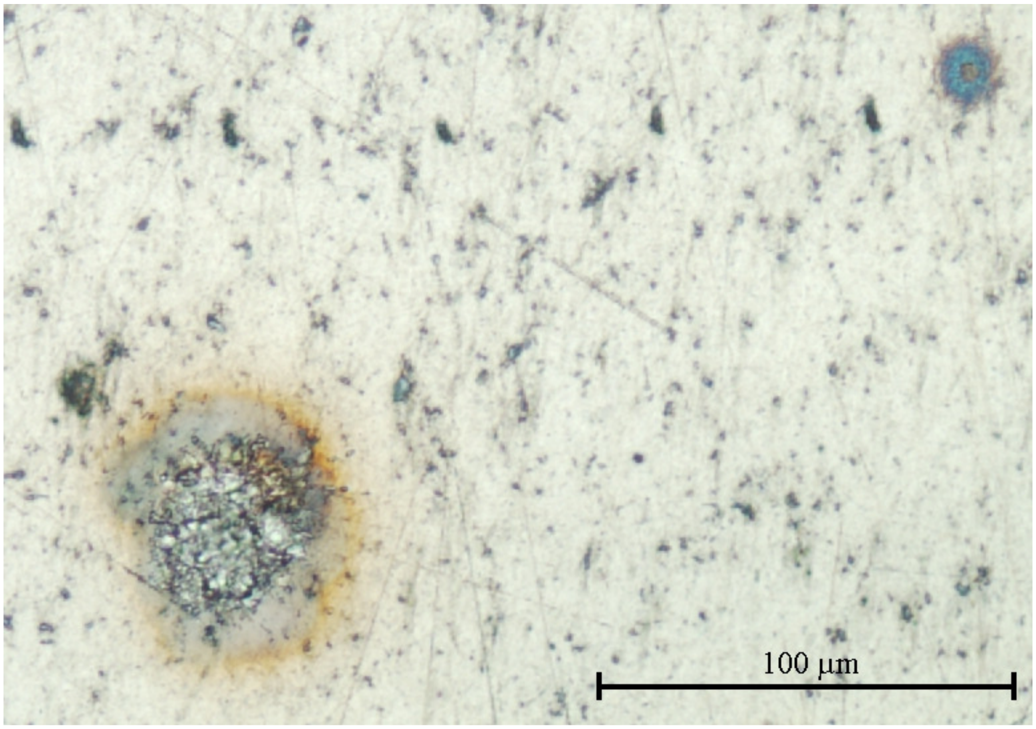

Figure 4.10: Copper substrate after 100 cycles at 100 V, from optical microscope at 20x

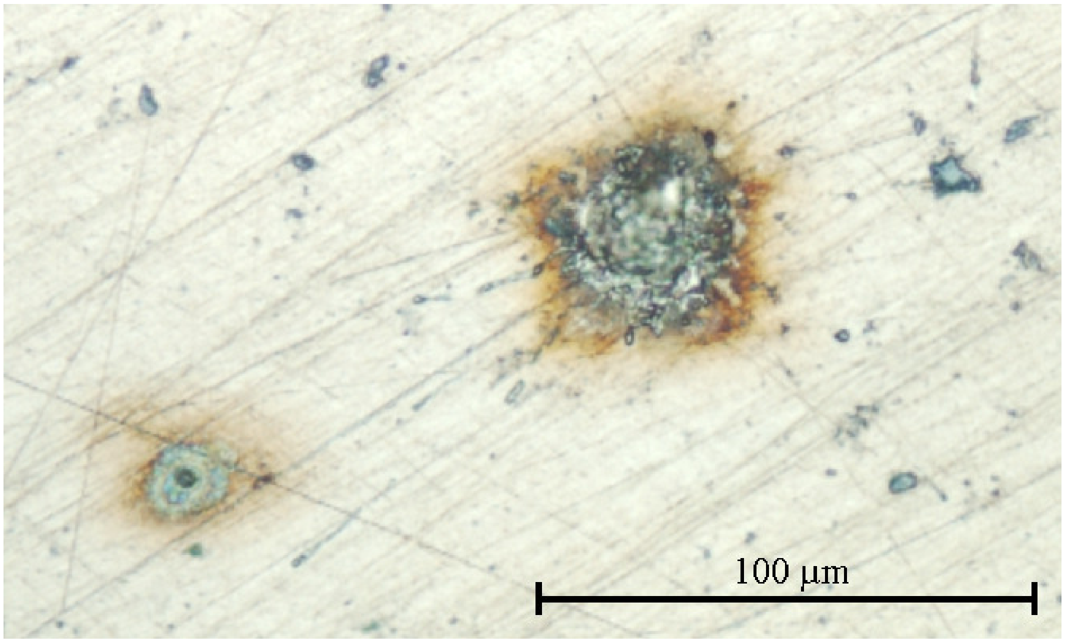

Figure 4.11: Copper substrate after 5 cycles at 150 V, from optical microscope at 20x

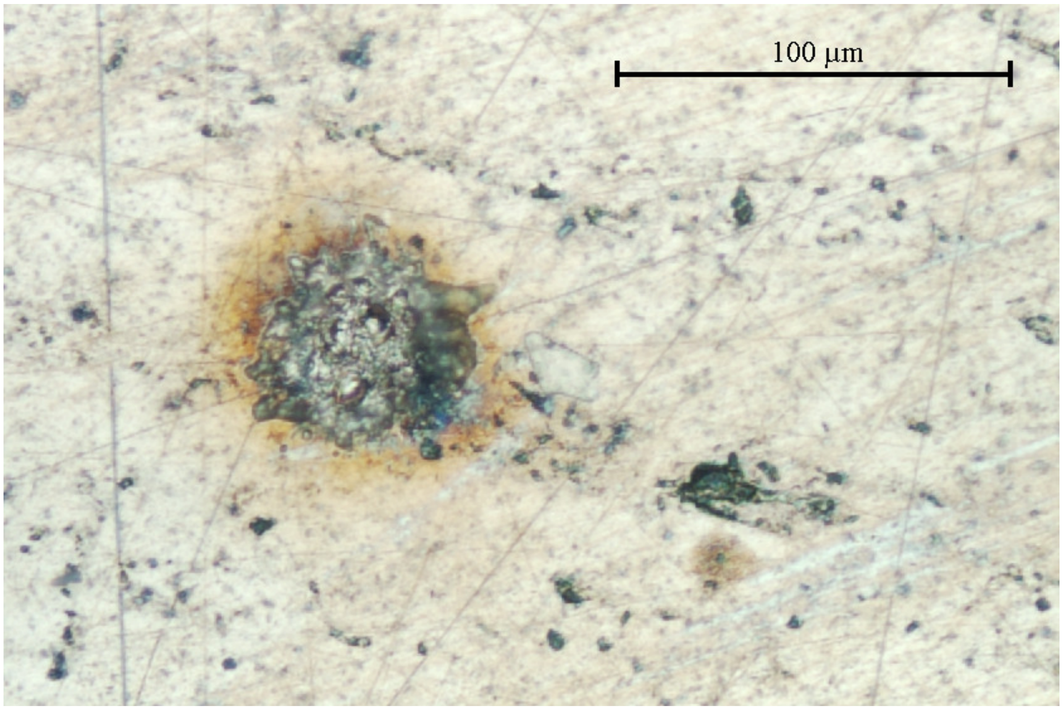

Figure 4.12: Copper substrate after 25 cycles at 150 V, from optical microscope at 20x

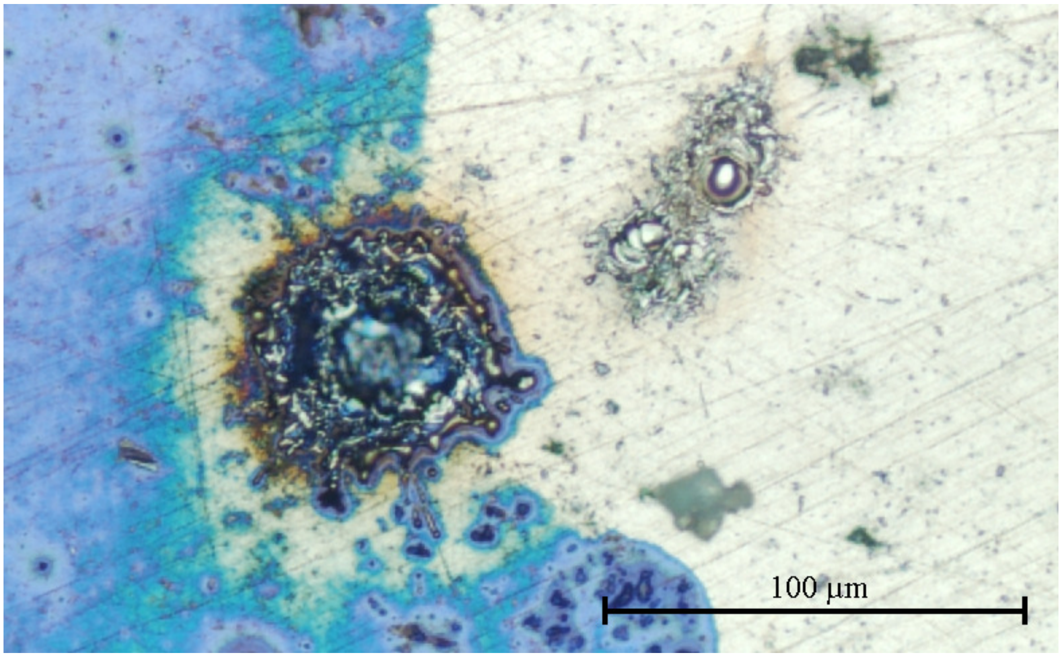

Figure 4.13: Copper substrate after 50 cycles at 150 V, from optical microscope at 20x

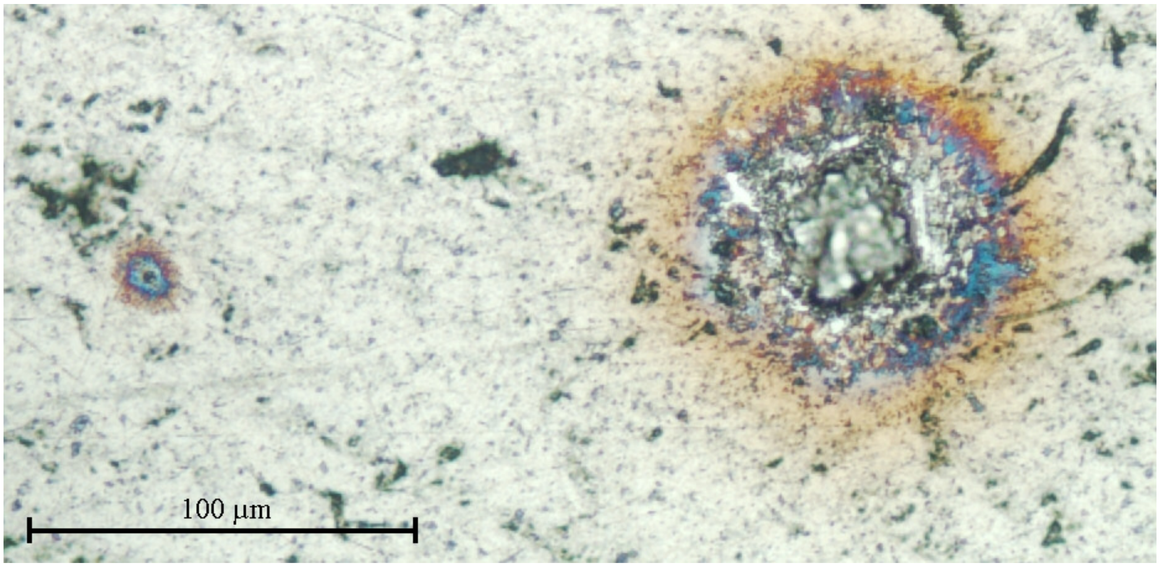

Figure 4.14: Copper substrate after 100 cycles at 150 V, from optical microscope at 20x

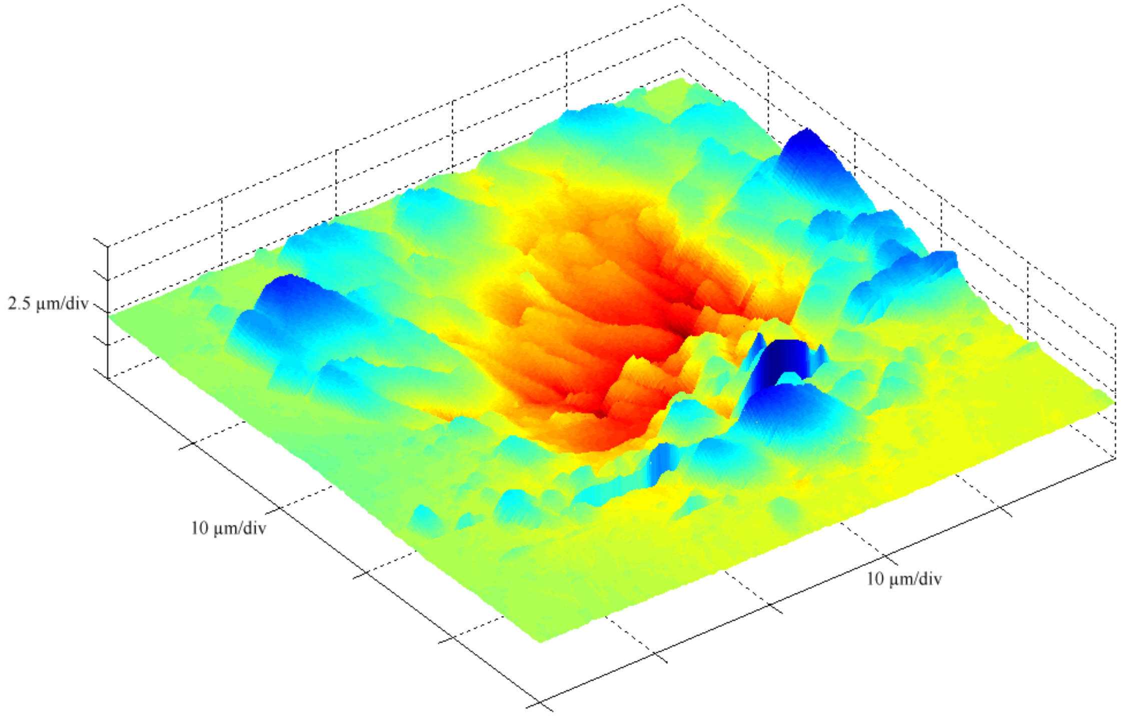

Figure 4.15: Copper substrate after 50 arcing cycles at 150 V, using AFM

Copper substrates were subjected to 5, 25, 50, and 100 discharges with the probe at each of 75 V, 100 V, and 150 V. In these experiments, the probe voltage was fixed at the desired level and the specimen was brought close to the probe until an arc was struck and then removed to quench the arc; this was repeated for the desired number of cycles. Even with several stages of polishing to remove asperities prior to experimentation, definitive visual evidence of the arcing site was observed only for the case of 100 V arc discharge at 100 cycles and for all cases at 150 V. A verification step in which the probe would contact the substrate at a distance of either 100 or 200 µm from the test site to determine the standoff distance, and a blue marker were used to identify the region of interest using microscopy or with the naked eye, respectively.

Quantitative analysis of these images can yield significant quantities of interest concerning the arcing sites such as the radius of the cavity formed by the arcing, the radius where sputtered substrate material has settled, and the radius of the discoloration that may be due to heating and oxidation. Undefined regions (e.g. appearing white in Fig. 4.16) are where fringes could not be resolved and not for a depth beyond the scale bar. Estimates of these radii are given in Table 4.2; the general trend is that these values appear to be saturated at a few tens of microns, perhaps indicating the diameter of the arc.

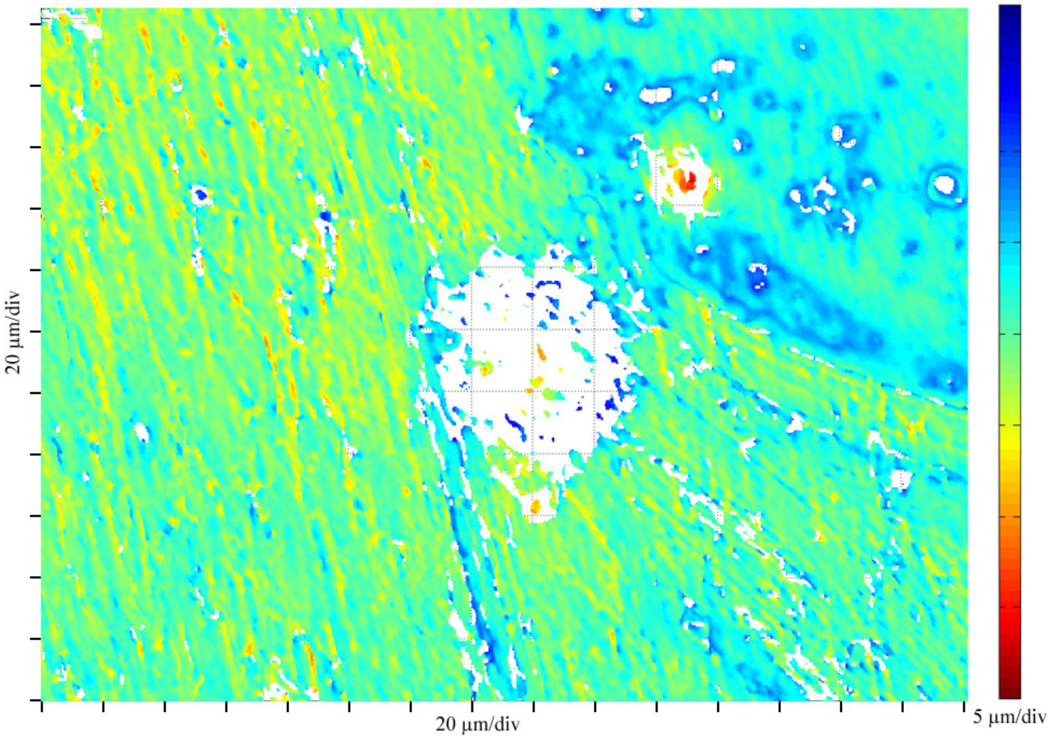

Figure 4.16: Copper substrate after 100 cycles at 100 V, from optical profiler at 21x

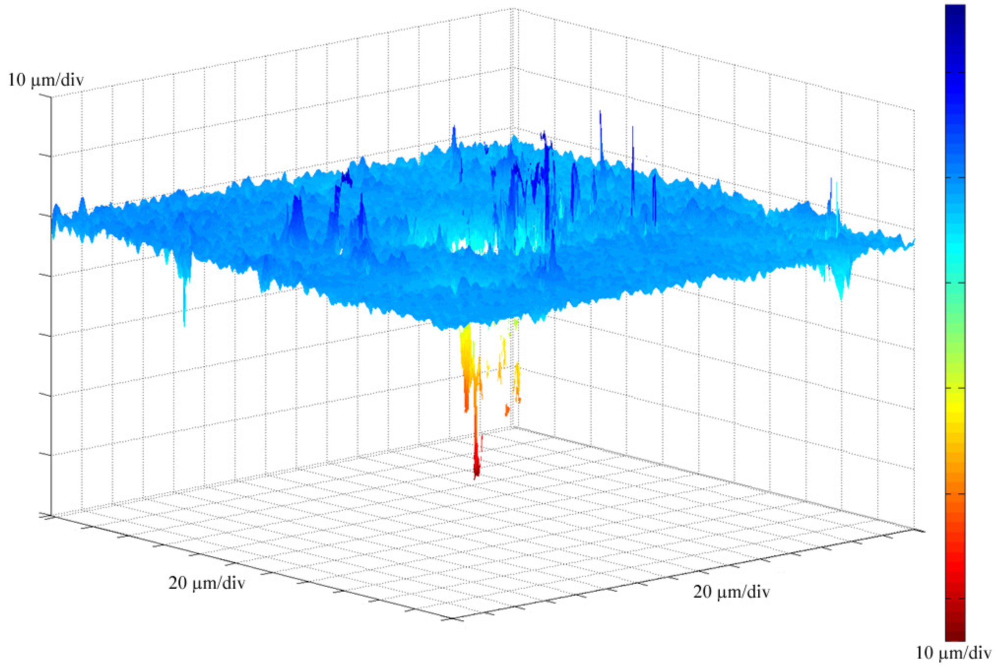

Figure 4.17: Copper substrate after 5 cycles at 150 V, from optical profiler at 21x

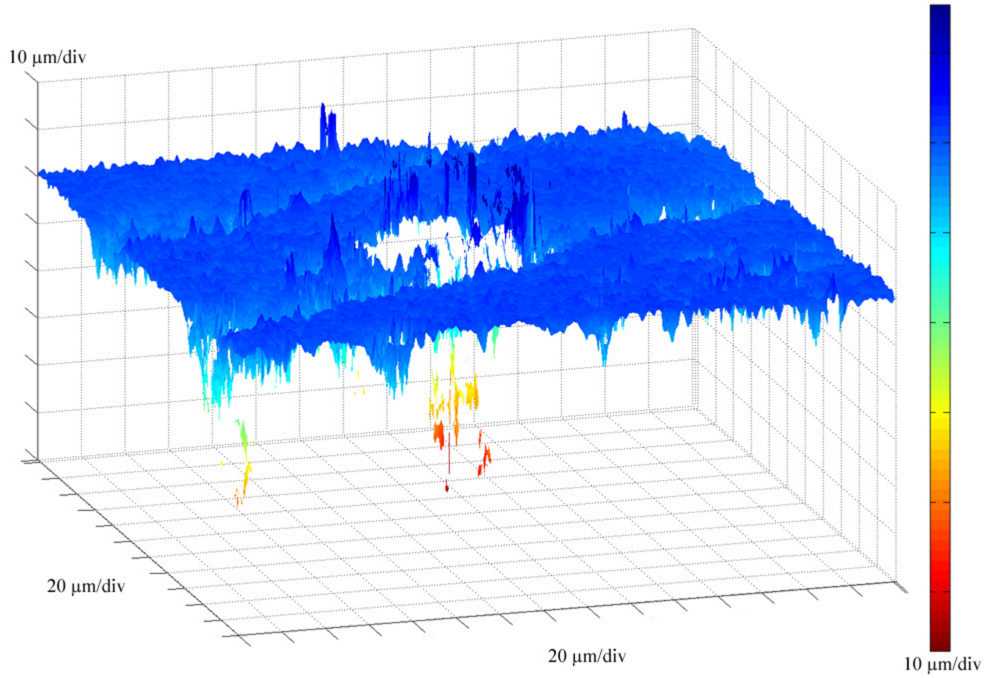

Figure 4.18: Copper substrate after 25 cycles at 150 V, from optical profiler at 21x

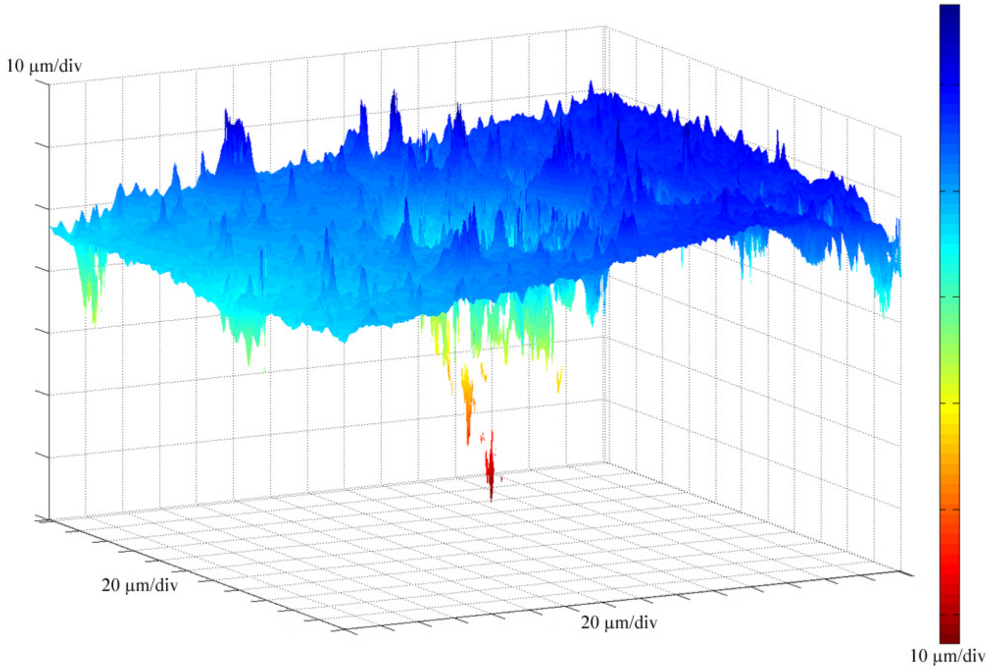

Figure 4.19: Copper substrate after 50 cycles at 150 V, from optical profiler at 21x

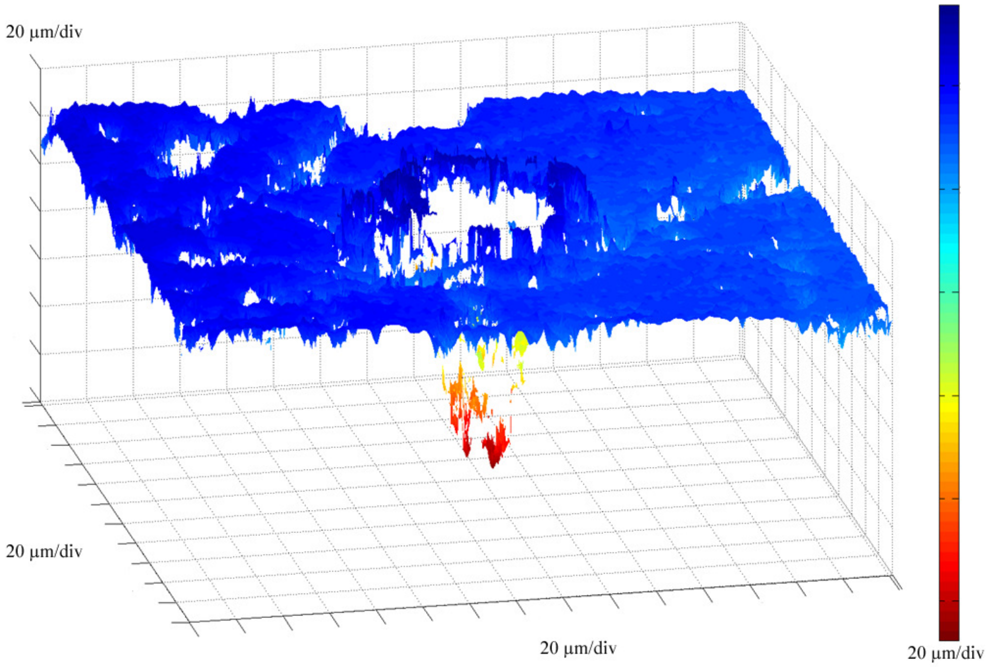

Figure 4.20: Copper substrate after 100 cycles at 150 V, from optical profiler at 21x

Copper Substrate (Voltage, Cycles)	Cavity Radius (µm)	Sputter Radius (µm)	Heat Radius (µm)
100 V, 100 cycles	17 ± 2	35	33 ± 1
150 V, 5 cycles	14 ± 1	27 ± 2	31 ± 5
150 V, 25 cycles	22 ± 1	36 ± 2	38 ± 2
150 V, 50 cycles	13 ± 2	23	36 ± 3
150 V, 100 cycles	22 ± 1	34 ± 3	49 ± 1

Table 4.2: Copper substrate cavity, sputter, heating radii as function of arcing voltage and cycles of discharge

4.4 EFFECTS OF ARCING FROM OVERVOLTAGE AND EXTENDED DWELL TIME

The modified Paschen curve (Fig. 3.3) shows that a minimum voltage is necessary for arcing to occur between the probe and the substrate in air at atmospheric pressure at a given distance. To investigate the physical effects that arcing would have if this distance was reduced and thus providing a greater voltage than necessary – an overvoltage – experiments were conducted on a copper substrate. Albright and Raja [13] indicates that the calculated heat flux corresponded to such an overvoltage (Fig. 4.21). In this figure, the heat flux for difference overvoltages and gap distances is shown; clearly, as the overvoltage reaches about 30 V, the heat flux saturates. This variation in the heat flux should, of course, be reflected in the arc-erosion pit. Hence, experiments were performed on copper probe-copper substrate system to record the arc-erosion pits from different overvoltages. These tests were a slight modification of the test used to obtain the modified Paschen curve; the substrate approached the probe until arcing was established, but was then brought closer by an additional distance thus providing the overvoltage; furthermore, the overvoltage situation was held for a duration of about ten seconds – an order of magnitude or greater than with previous arc tests. This was performed for a range of voltages and distances (Table 4.3) and, using the Paschen curve, the extended arcing distance was matched with its corresponding overvoltage. Optical microscopy (Fig. 4.22) and an optical profiler (Figs. 4.23-4.30) were used to image the overvoltage arc sites and extract quantitative measures of the arc-erosion pit.

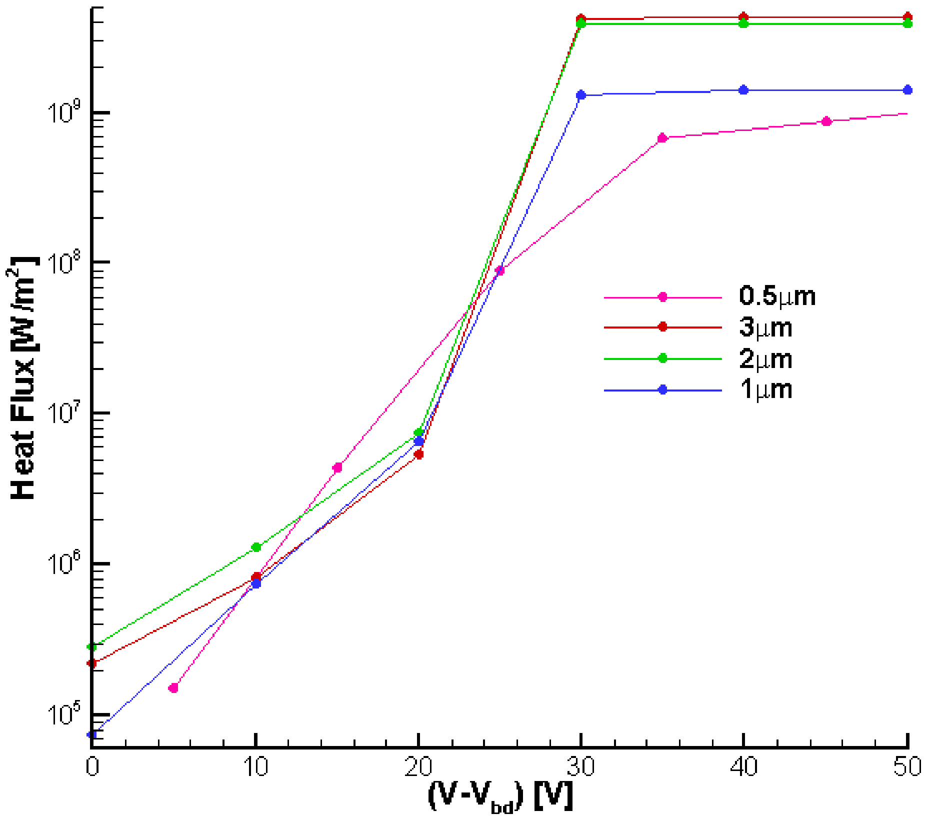

Figure 4.21: Computational heat flux and overvoltage for varying interelectrode distances [13]

Copper Substrate Applied Voltage (V)	**Interelectrode Distances (µm)**	**Corresponding Overvoltage (V)**
75	0.7, 0.5, 0.3	0, 10, 20
125	2.0, 1.5, 1.2, 0.5, 0.4	10, 25, 30, 60, 65
150	2.9, 2.0, 1.0, 1.0, 0.4	0, 35, 65, 65, 90

Table 4.3: Copper substrate with applied voltage and overvoltages

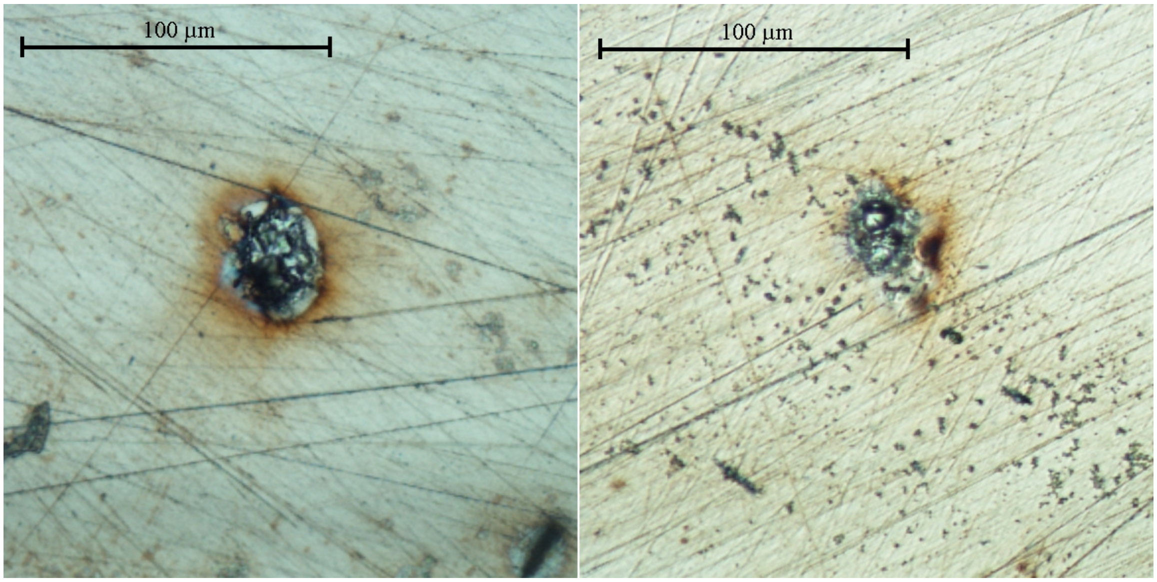

Figure 4.22: Copper substrate with 0 and 65 V overvoltage above 150 V, from optical microscope at 20x

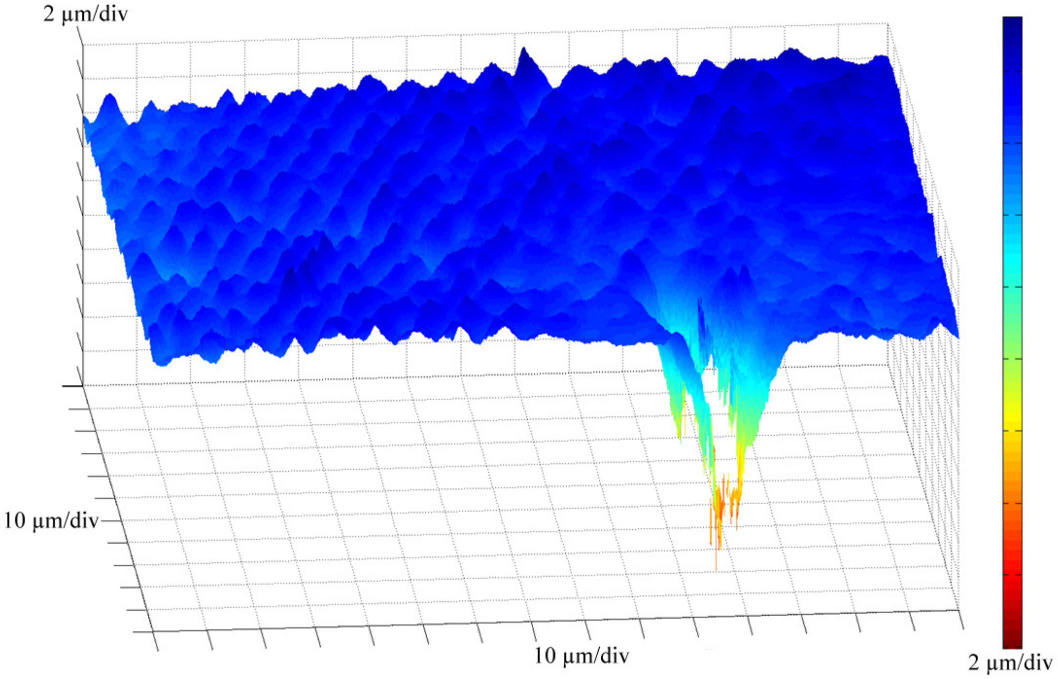

Figure 4.23: Copper substrate at 10 V overvoltage of 75 V, from optical profiler at 42x

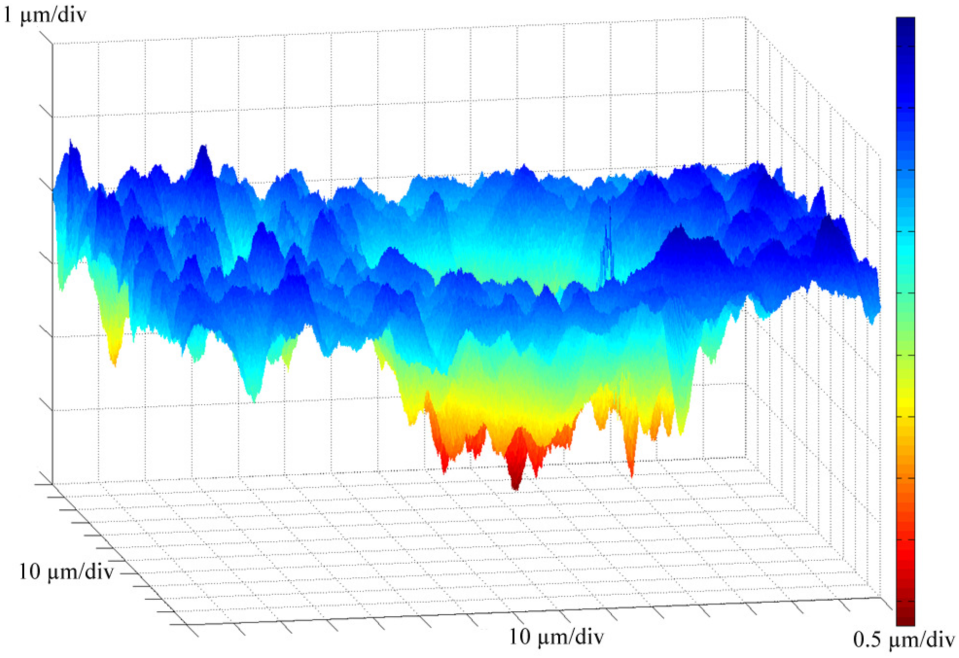

Figure 4.24: Copper substrate at 20 V overvoltage of 75 V, from optical profiler at 42x

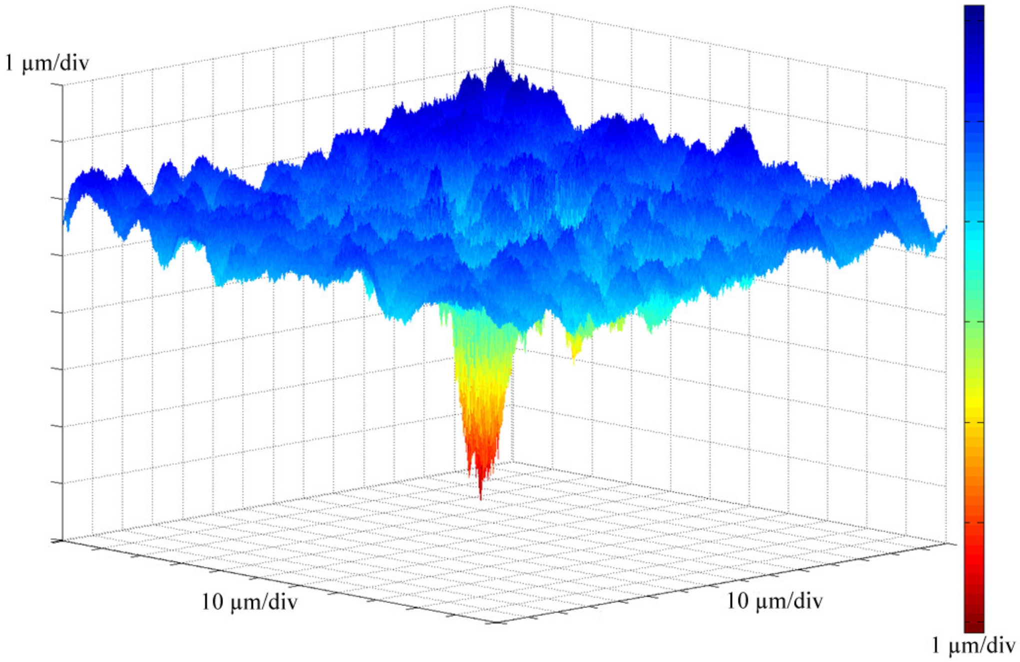

Figure 4.25: Copper substrate at 10 V overvoltage of 125 V, from optical profiler at 42x

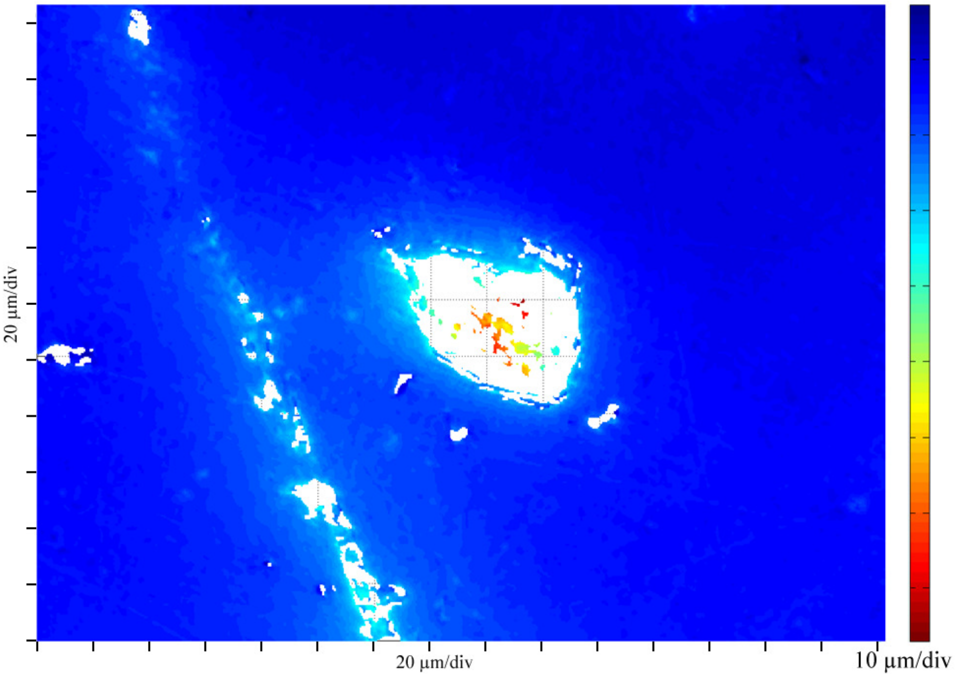

Figure 4.26: Copper substrate at 30 V overvoltage of 125 V, from optical profiler at 21x

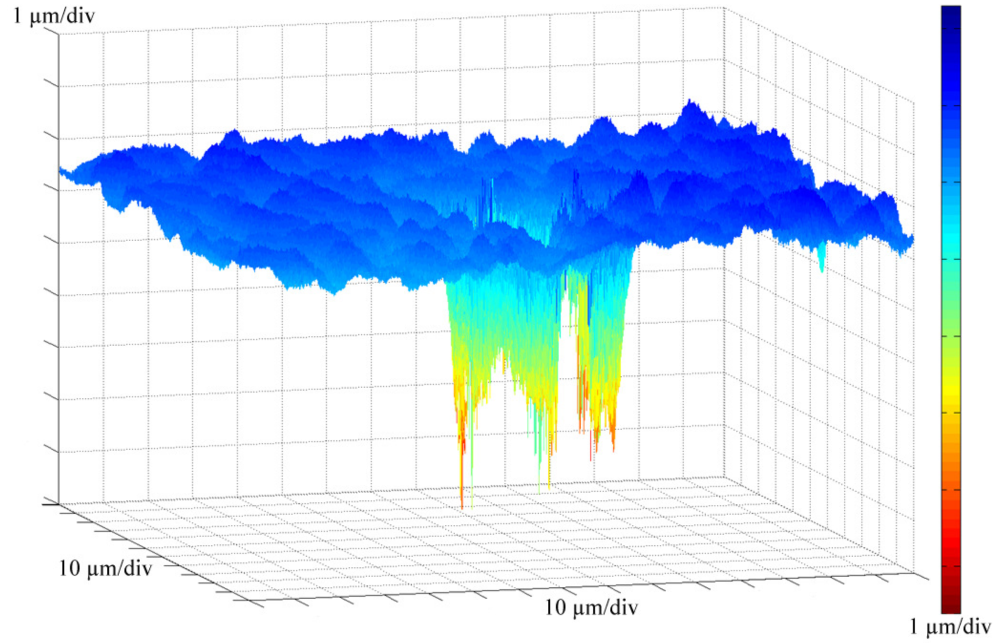

Figure 4.27: Copper substrate at 60 V overvoltage of 125 V, from optical profiler at 42x

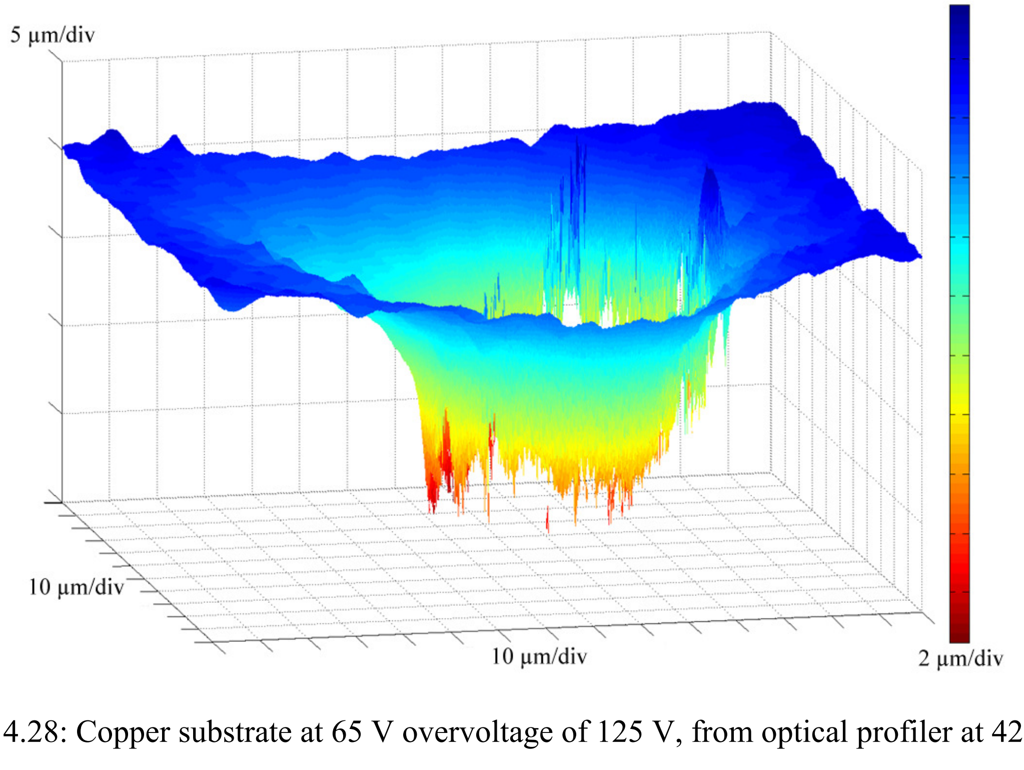

Figure 4.28: Copper substrate at 65 V overvoltage of 125 V, from optical profiler at 42x

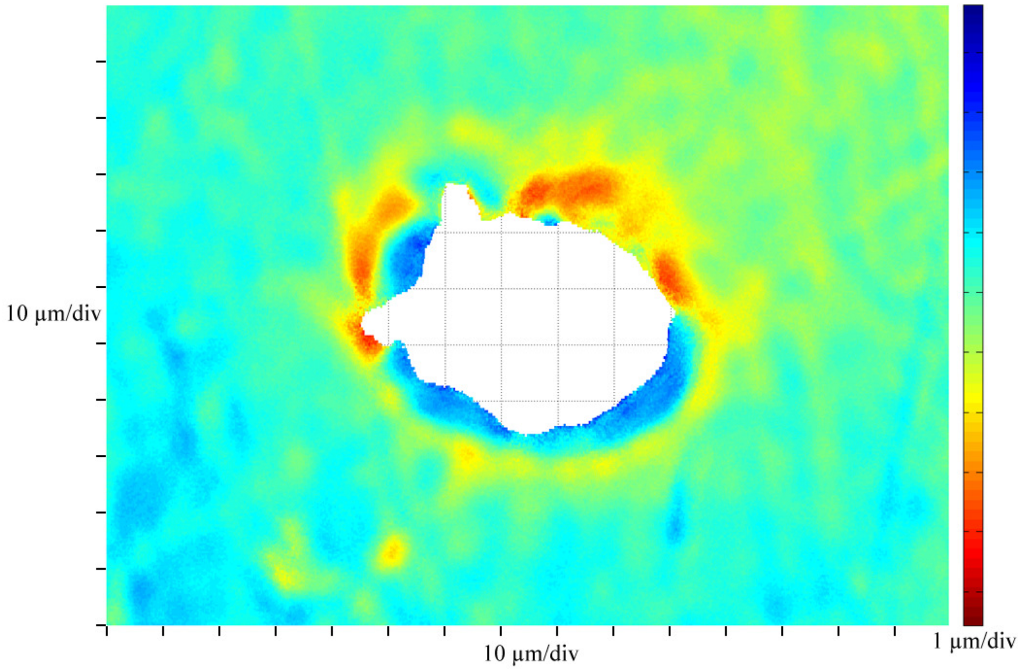

Figure 4.29: Copper substrate at 0 V overvoltage of 150 V, from optical profiler at 42x

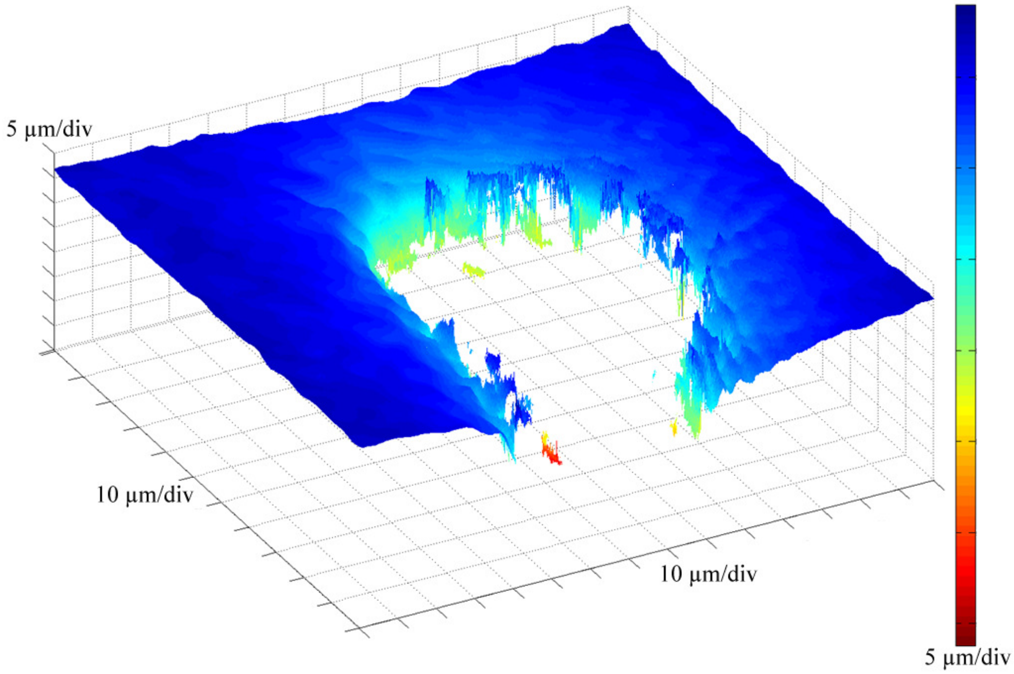

Figure 4.30: Copper substrate at 65 V overvoltage of 150 V, from optical profiler at 42x

The cavity radius at the surface of the substrate is easily obtained from the profilometer measurements. The cavity depths seemed to be sufficiently large that the optical profiler could not obtain data from the bottom of the erosion pit; therefore, we adopt two measures: the minimum estimated cavity volume and the cavity cross-sectional area at a depth of 1 μm. These measurements are given in Table 4.4 and plotted in Figure 4.31. A number of observations can be made from these experiments:

- The overvoltage cavity radii, which underwent a single arc with a ten second dwell time, had a smaller value than when the dwell time was shorter but with multiple arc discharges.
- The cavity radii tended to be greater if the voltage was larger as well; from Table 4.4 and Figure 4.31, although the scatter is large, one can see that the arc-erosion pit increases in size from about 5 μm to about 30 μm when the overvoltage is about 30 V and then saturates. The large scatter is due to uncertainty in identifying the gap distance and therefore the overvoltage. If we consider this in light of the estimates of the heat flux shown in Figure 4.21, one can understand qualitatively the increase and saturation of the arc-erosion pit size easily.
- Figure 4.29 shows asymmetry with substrate material being displaced to the opposite side of the depression rather than around it.

Copper Substrate		Cavity Radius (µm)	Minimum Estimate Cavity Volume (µm^3)	Estimated Cavity Cross-section Area at 1 µm Depth (µm^2)
Voltage (V)	Overvoltage (V)			
75	0	5 ± 1	235	80
	10	6 ± 4		
125	10	5 ± 1	315	80
	25	6 ± 2		
	30	20 ± 4		530
	60	20 ± 2	5650	960
	65	40 ± 2	70000	3850
150	0	32 ± 3	1900	12500
	65	16 ± 2		
		37 ± 1		4180
	90	11 ± 3		

Table 4.4: Copper substrate cavity radii, volume, and area as function of arcing voltage and overvoltage, with ten second dwell time

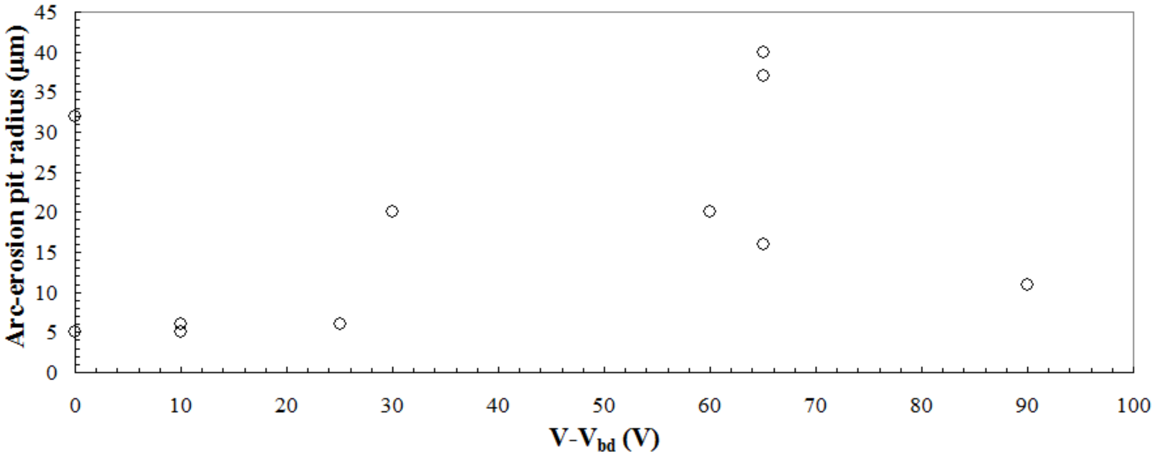

Figure 4.31: Arc-erosion pit radius as a function of overvoltage

Further experimentation with overvoltage involved initiation of an arc and, in an attempt to drag the arc, repeated horizontal translation scans of the substrate underneath the probe. At a gap voltage of 100 V 50 cycles of 100 μm, and 200 μm, horizontal scans were then performed. A Tektronix DPO 3034 Digital Phosphor Oscilloscope was used to monitor the power supply voltage as a function of time for varying the voltage with scan length. Since the gap distance varies as a function of the scan distance (due to roughness and possible global tilt), the overvoltage varied along the length and hence it is not included here. An optical image of the 200 μm horizontal translation is shown in Fig. 4.32; profilometer images of both 100 μm and 200 μm tests are shown in Fig. 4.33 and Fig. 4.34, respectively. The optical image in Fig. 4.32 shows that instead of observing an elongated erosion zone, a nearly circular erosion pit is seen, with a surrounding elongated heat tinted region. An SEM image of the same scar shown in Figure 4.35 clearly indicates that the erosion pit is circular. The profilometer measurements in Fig. 4.33 and Fig. 4.34 confirm this observation. It appears that instead of the arcing location dragging along the translation direction, the arc maintains its original position even as the probe is translated horizontally. It appears that the plasma from the electrical arc minimized its energy by taking a longer path through the air between the electrodes than re-establishing a moving point on the substrate. Scan lengths larger than 200 μm could not be performed since these require either an additional or different PZT stage on the MFT. Efforts to do this with a macroscopic translater did not succeed because of the inability to maintain a constant gap distance.

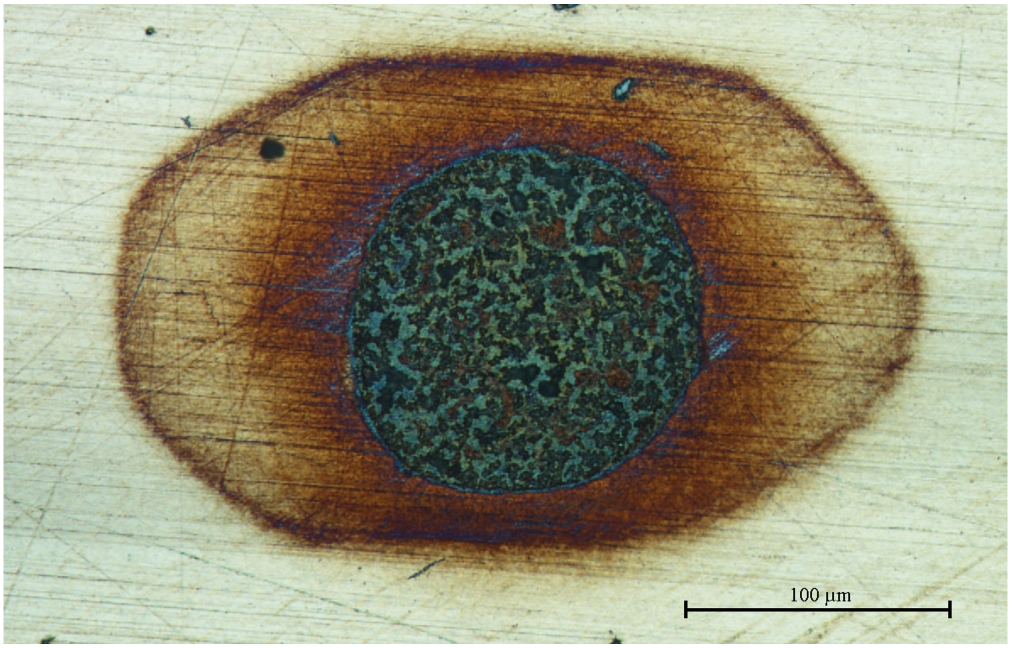

Figure 4.32: Copper substrate at 100 V with 50 horizontal cycles of 200 μm, from optical microscope at 20x

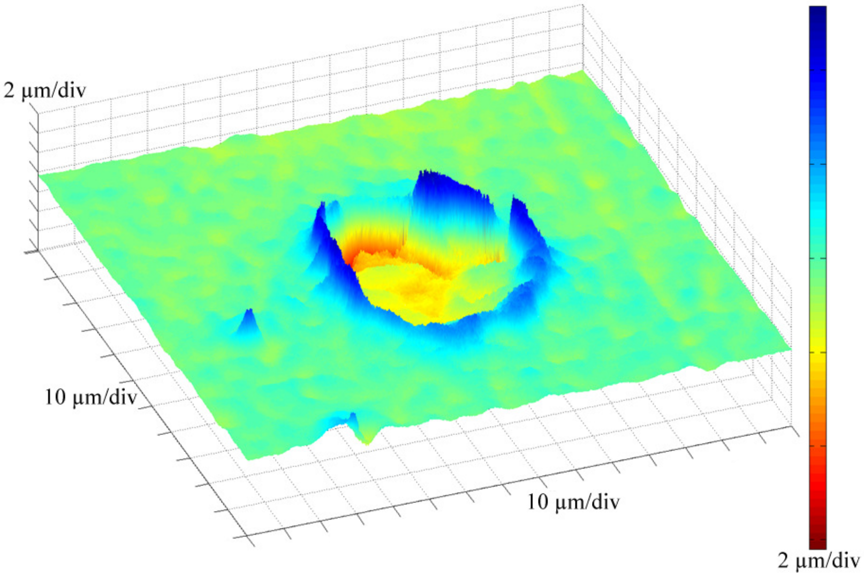

Figure 4.33: Copper substrate at 100 V with 50 horizontal cycles of 100 μm, from optical profiler at 42x

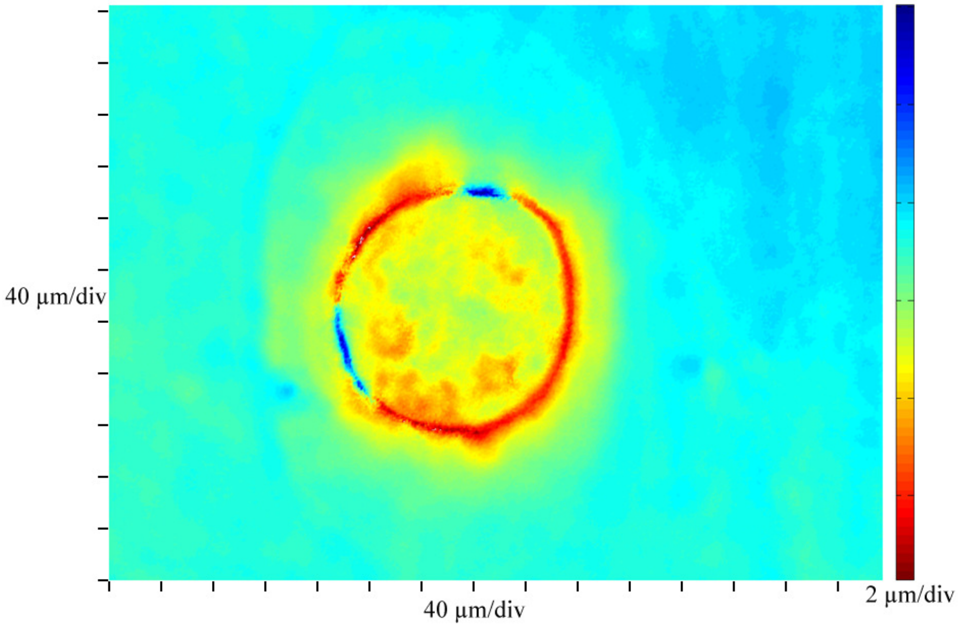

Figure 4.34: Copper substrate at 100 V with 50 horizontal cycles of 200 µm, from optical profiler at 10x

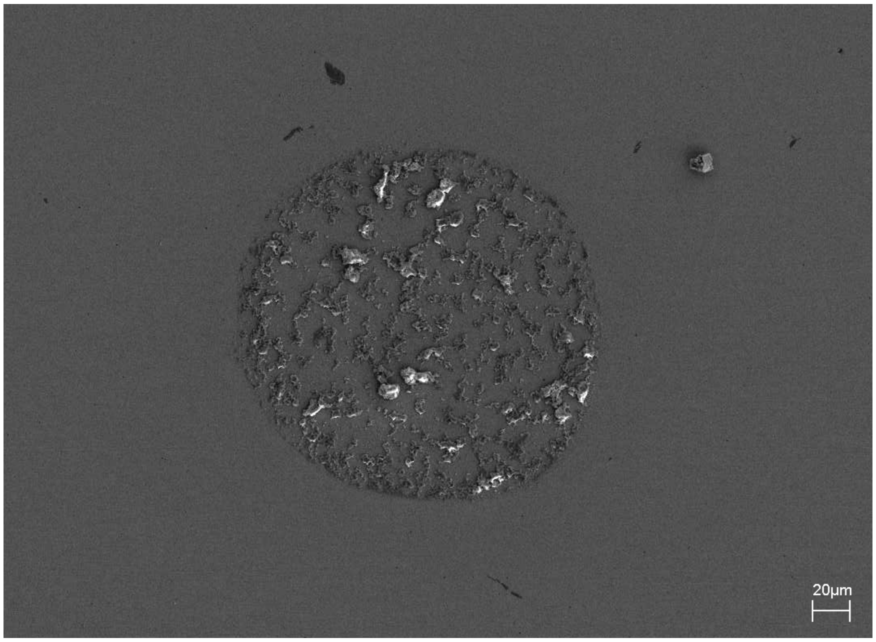

Figure 4.35: Copper substrate at 100 V with 50 horizontal cycles of 200 µm: secondary electron image at 850x, 15 mm WD

Chapter 5

Solid-solid Contact Erosion

5.1 INTRODUCTION

Solid-solid contact erosion is a contact regime that occurs between the rails and armature interface as a consequence of the projectile beginning its acceleration through the railgun and before friction causes the outer layers to melt and act as a lubricant. The normal force between the rail and armature are experimentally modeled as the probe is brought into contact perpendicular to the substrate. The German physicist Heinrich Hertz found that for contact between two elastic spherical objects the relation [14] between the contact radii *a* and the normal force *P* is:

$$a^3 = \frac{3}{4}\left(\frac{1-\nu_1^2}{E_1} + \frac{1-\nu_2^2}{E_2}\right)\left(\frac{R_1 R_2}{R_1 + R_2}\right)P \tag{5.1}$$

where:

ν: Poisson's ratio of object

E: modulus of elasticity (pascals)

R: radius of object (meters)

For the case of copper probe and flat, copper substrate $\left(R_2 \to \infty\right)$, the contact radius is then:

$$a = \left[\frac{3}{2} \left(\frac{1 - \nu_{Cu}^2}{E_{Cu}} \right) R_{probe} P \right]^{1/3} \tag{5.2}$$

Knowing the electric current *i*, this estimate of the contact radius is used to obtain a measure of the average current density

$$J = \frac{i}{\pi a^2} \,. \tag{5.3}$$

In railguns this is on the order of 10^{10} A/m^2.

5.2 EFFECT OF VOLTAGE

The normal and shear forces on the probe were calibrated using the PSD deflections along with the material and geometrical properties of the beam and probe. Previous studies investigated at the effect of voltage and friction using a steel probe on copper substrate [1] and tungsten probe on mica substrate [15]. Brown et al. [1] found that the friction coefficient at similar normal forces was substantially reduced by applying a constant current (Fig. 5.1).

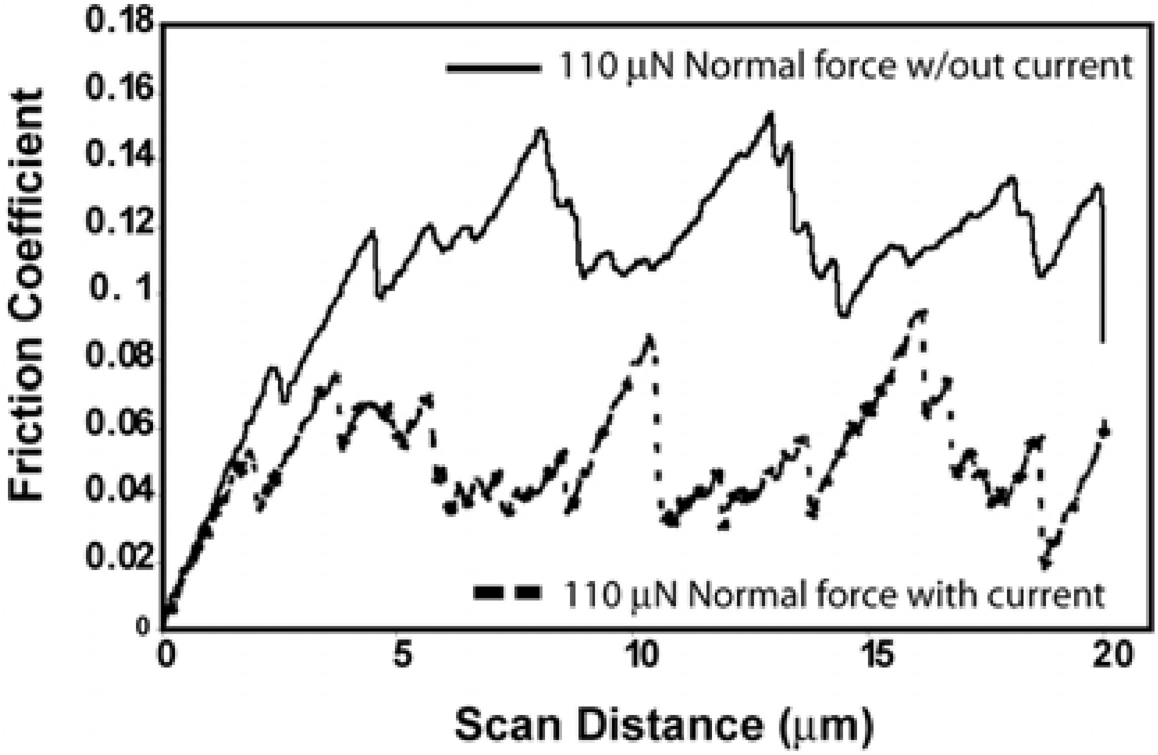

Figure 5.1: Friction coefficient comparison between similar normal force (110 μN) with and without an applied constant current between steel and copper [1]

Power supply voltages of 0 V, 5 V, and 50 V were used with 70 μm horizontal scan repeated 100 times at a normal force of 325 μN, with each different voltage scan separated by 100 μm from the other (Fig. 5.2). The probe had radius of curvature of 44 μm. From the Hertz contact radius in Equation 5.2 and using the copper elastic modulus E = 110 GPa and Poisson's ratio $\nu = 0.34$, the contact radius is 0.56 μm. The current densities for the 5 V and 50 V cases was on the order of $4 \cdot 10^6$ A/m^2 and $4 \cdot 10^7$ A/m^2, respectively. This current density is expected to be several orders of magnitude smaller than from arcing due to the large normal force and thus large contact radius, as well as the relatively low supply voltage and thus low current. Calibration details are detailed in Appendix A.5.

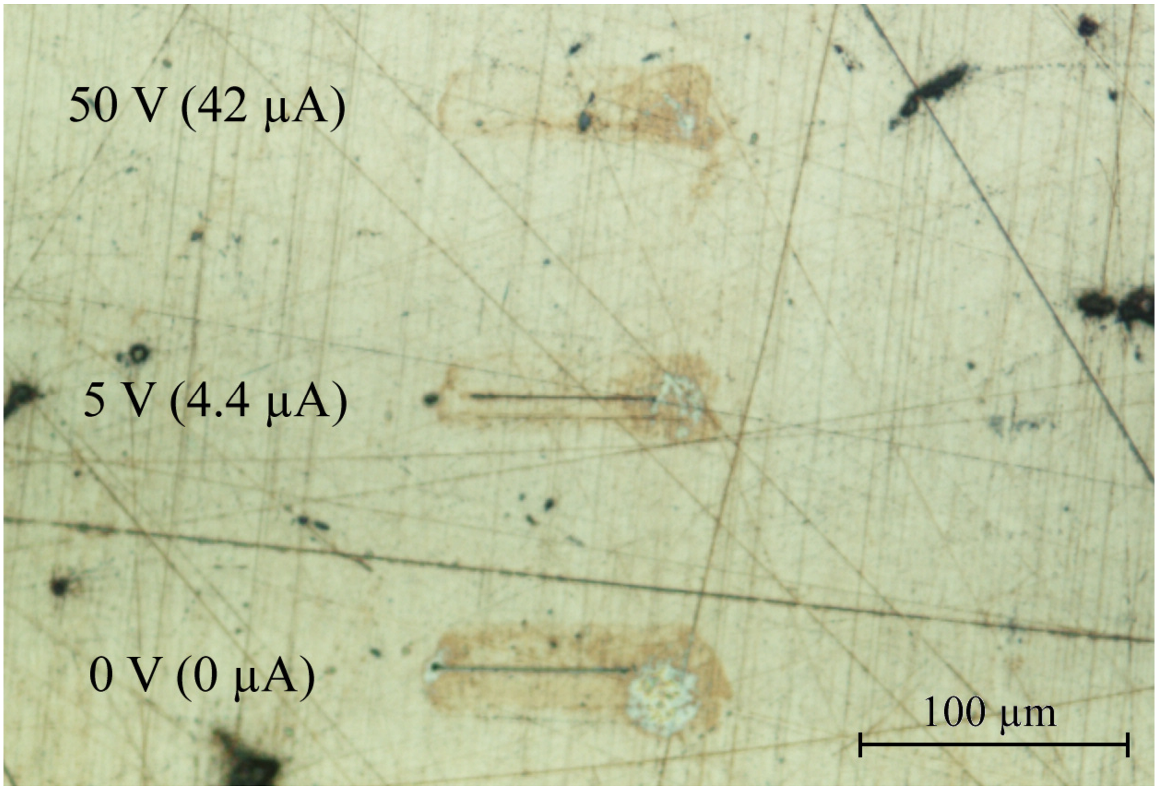

Figure 5.2: Wear from friction on copper substrate for 70 μm horizontal scans from supply voltage of 0 V, 5 V, 50 V, from optical microscope at 30x

Slightly more wear was seen on the 0 V case (Fig. 5.3) than by the 5 V case (Fig. 5.4), while there was very little scarring at 50 V (Fig. 5.5). Heating effects from the high current density were observed along the length of the horizontal scan path (Fig. 5.2). Confirming previous results [1], wear from friction was reduced in the presence of a constant applied current (Fig. 5.6).

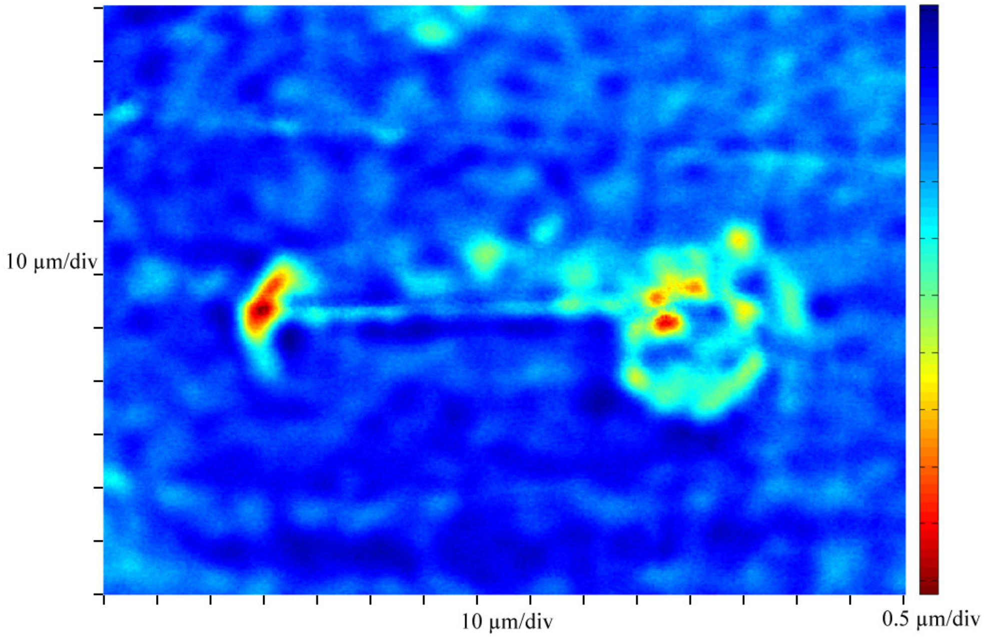

Figure 5.3: Copper substrate at 0 V with 325 µN normal force for 100 horizontal cycles of 70 µm, from optical profiler at 42x

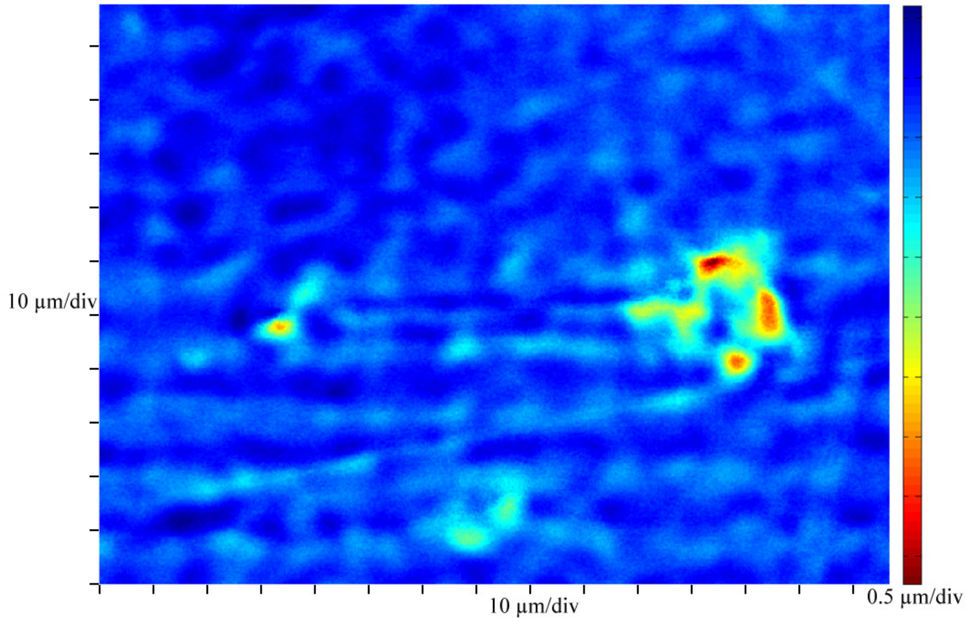

Figure 5.4: Copper substrate at 5 V with 325 µN normal force for 100 horizontal cycles of 70 µm, from optical profiler at 42x

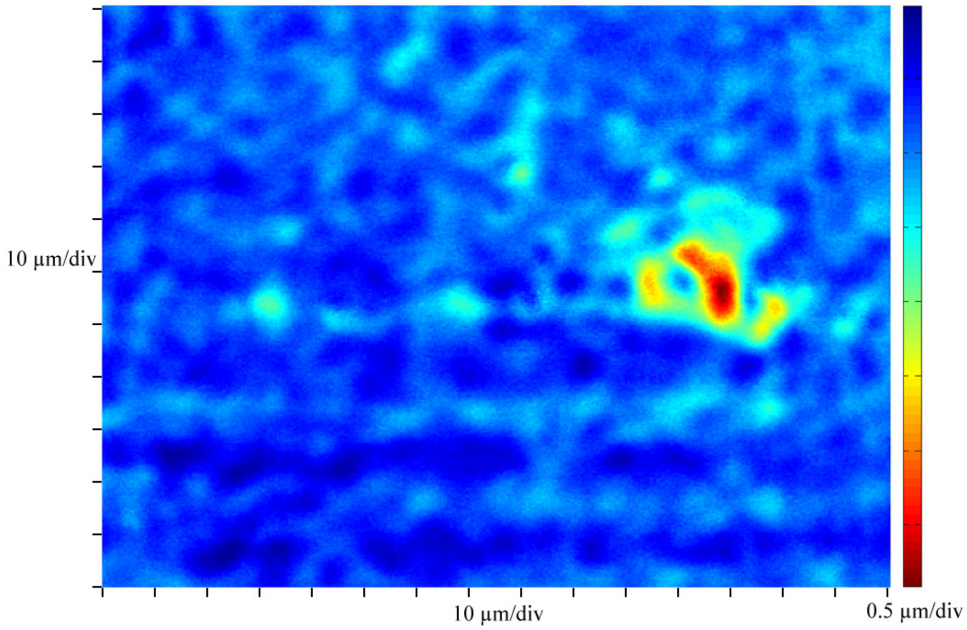

Figure 5.5: Copper substrate at 50 V with 325 µN normal force for 100 horizontal cycles of 70 µm, from optical profiler at 42x

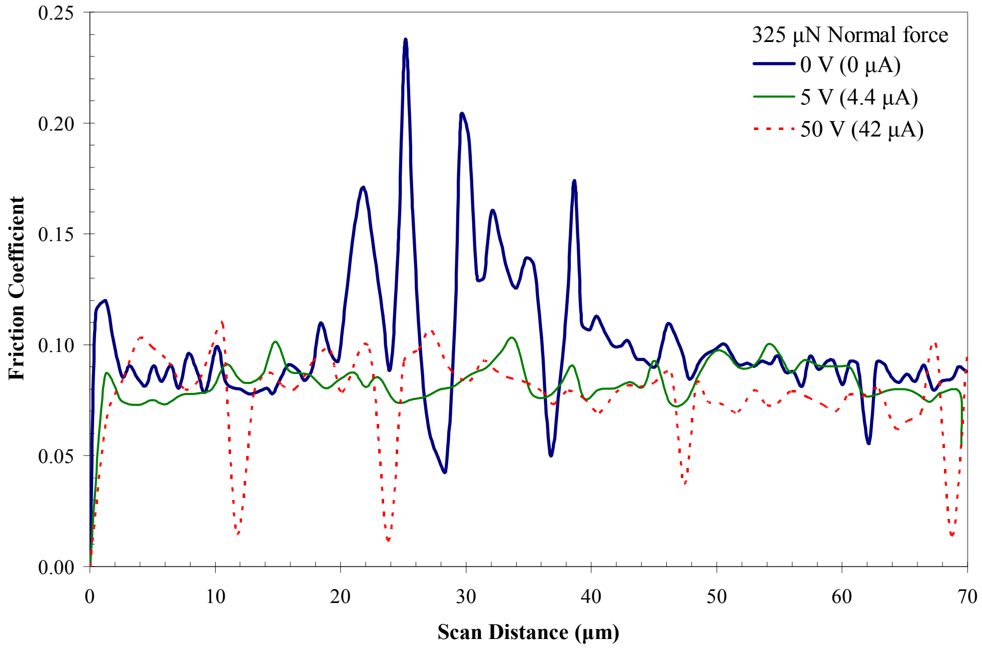

Figure 5.6: Coefficient of kinetic friction for copper probe and substrate at 325 µN normal force with constant applied current of 0 µA, 4.4 µA, and 42 µA

Chapter 6

Conclusions

6.1 EFFECTS FROM ARCING, FRICTION, AND ENVIRONMENT

The purpose of the research was to aid in developing a multishot electromagnetic launcher by investigating the proposed contact regimes that occur in the rail-armature interface of railguns. Surface asperity interactions for arcing and solid-solid contact were experimentally modeled with a modified Mesoscale Friction Tester (MFT). The MFT enabled exploration of applied forces and contact radii that lie between that of an Atomic Force Microscope (AFM) and Surface Force Apparatus (SFA), using state-of-the-art actuators, sensors, and digital data acquisition and control systems. The rail-armature interface was simulated with electrochemically etched and polished copper probes with sub-micrometer roughness and polished copper substrates.

A power supply delivered direct current (dc) through the probe and substrate, obtaining current densities similar to that in railguns, on the order of 10^{10} A/m^2. A modified Paschen curve for air at atmospheric pressure was empirically determined by finding the minimum distance for arcing to occur. The dominant physical mechanism for scales of a few micrometers is field emission of electrons, as opposed to Townsend avalanche of ionized gas, with a more linear relationship than the classical Paschen curve. Findings included hysteresis between arc initiation and quenching as well as due to the polarity of the probe and substrate. Environmental effects such as humidity and vibration were controlled while computational simulations revealed that a pure argon environment would have a similar modified Paschen curve as that of air.

The effects of erosion were analyzed using scanning electron microscopy (SEM), atomic force microscopy, optical microscopy, and an optical profiler. Arcing erosion was more exaggerated with larger currents, repeated strikes, and by extending the dwell time. After arcing, copper probe tips exhibited morphological changes but electron backscatter diffraction was unable to determine if this outermost layer was crystalline or amorphous. A cavity at the center of the arc site was surrounded by a ring of material, which in turn had discolored copper – presumably from the localized temperature increase of the plasma. The effects of overvoltage, a voltage beyond the level required to initiate an arc, had inconclusive effect on the size of the cavity. Translation of the substrate once arcing had begun strongly suggest that once an arc had formed that it did not re-establish itself along the shortest distance between the probe and substrate but rather altered its path between the two electrodes through the air.

Solid-solid contact examined the tribological effects from friction with a constant normal force as a function of applied current. Confirming previous work using tungsten on mica and steel on copper, these copper on copper experiments verified that the coefficient of kinetic friction was reduced in the presence of constant current. Optical microscopy images and profiler topography revealed noticeable visual evidence that increased current with a constant normal force reduced the wear on the substrate.

6.2 FUTURE WORK

There are several parameters that can be further explored in future work on examining the contact regimes in the rail-armature interface. Greater current densities can be obtained by reducing the probe radius of curvature and very fine, subnanometer roughness tungsten probe tips could be used. A large variety of polished plates, perhaps aluminum or steel, could be exchanged for the copper substrate. Further modification to the Mesoscale Friction Tester (MFT) such as equipping a different PZT stage for axial scans beyond 200 μm would be a significant asset in overvoltage experiments. A vacuum pump and sealed MFT would enable different gaseous environments (e.g. Ar, N_2, CO_2), such that Paschen curves could be experimentally found beyond that of air. Changes to temperature or pressure may also be possible in this setup. The effect of relative humidity on shear strength also warrants further investigation.

Appendices

A.1 RANGE OF PROBE TIP RADII OF CURVATURE FOR VARIOUS CONDITIONS

The radius of curvature is a function of wire material, immersion depth, etching voltage, aqueous solution concentration, and loop cathode (Table A.1). If the immersion depth is approximately one-half the wire diameter, there will be no drop-off [6].

Immersion depth / Etching voltage	**5 V**	**8 V**	**14 V**
0.4 mm		19 µm 147 µm 161 µm	23 µm 69 µm 106 µm
0.25 mm	15 µm	5 µm 89 µm 278 µm	41 µm 88 µm 135 µm
0.1 mm	28 µm	28 µm 65 µm 79 µm	58 µm 60 µm 79 µm
-0.2 mm	8 µm	64 µm 69 µm 56 µm	135 µm 147 µm

Table A.1: Radius of curvature of copper probe tips obtained at different etching voltage and immersion depths [7]

A.2 MESOSCALE FRICTION TESTER SETUP AND CALIBRATION FACTORS

The Mesoscale Friction Tester (MFT) requires normal forces and transverse moments to be calibrated from voltages to their appropriate physical value based on calibrations of the dimensions of the beam. Finer force resolution is obtained from thinner and longer beams due to the increased sensitivity of deflections at the tip. Table A.2 uses stainless steel beams of 12.7 mm width to obtain the following:

Thickness (µm)	Length (mm)	κ_N (µN/V)	κ_T (µN-m/V)	Resolution (µN)
25.4	9.5	50.6	0.53	0.051
	12.7	28.3	0.40	0.028
	25.4	7.0	0.20	0.007
50.8	12.7	226.8	3.19	0.227
	25.4	55.7	1.60	0.056
63.5	12.7	442.9	6.23	0.443
	25.4	108.9	3.12	0.108
76.2	12.7	765.3	10.77	0.765
	25.4	188.1	5.39	0.189

Table A.2: Mesoscale friction tester resolution and calibration values for steel of width 12.7 mm [7]

Setup of the virtual instrument panel (Figure A.1) requires inputing the resistance of the voltage divider circuit to obtain the shunt current, the flow between the substrate and probe. The resistance is that of the fixed resistor (2485 Ω) and potentiometer (maximum of 50.39 kΩ). The maximum and minimum shunt voltage can be altered in the channel configuration and this range is discretized to 65,536 (2^{16}) values.

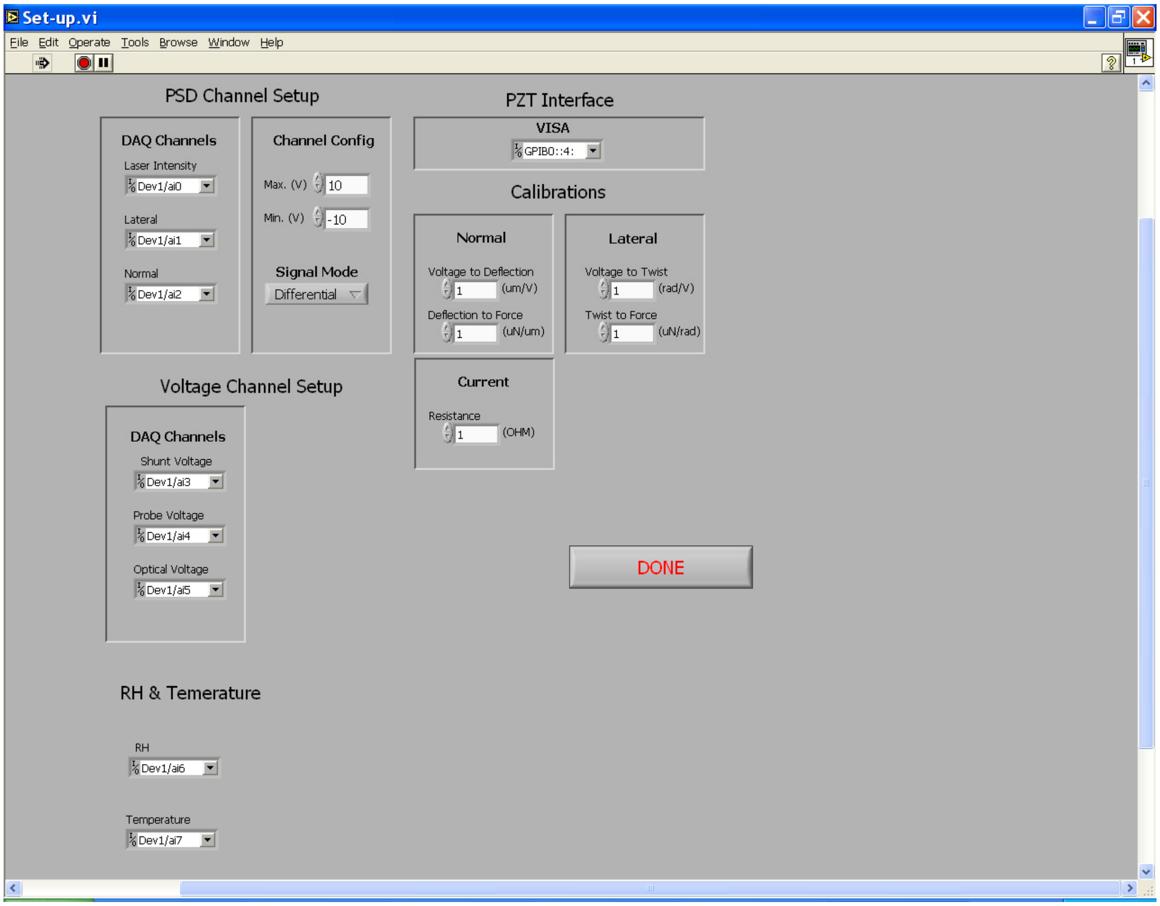

PSD Channel Setup

DAQ Channels
Laser Intensity: Dev1/ai0
Lateral: Dev1/ai1
Normal: Dev1/ai2

Channel Config
Max. (V): 10
Min. (V): -10
Signal Mode: Differential

PZT Interface

VISA: GPIB0::4:

Calibrations

Normal
Voltage to Deflection: 1 (um/V)
Deflection to Force: 1 (uN/um)

Lateral
Voltage to Twist: 1 (rad/V)
Twist to Force: 1 (uN/rad)

Current
Resistance: 1 (OHM)

Voltage Channel Setup

DAQ Channels
Shunt Voltage: Dev1/ai3
Probe Voltage: Dev1/ai4
Optical Voltage: Dev1/ai5

RH & Temerature
RH: Dev1/ai6
Temperature: Dev1/ai7

Figure A.1: Mesoscale friction tester virtual panel setup screen

Saved experimental results are automatically recorded as a tab-delimited text file with the filename MFT*YYYYMMDDhhmmss*.txt, for year *YYYY*, month *MM*, day *DD*, hour *hh*, minute *mm*, and second *ss*. Certain parameters are not recorded, such as power supply voltage, temperature, or relative humidity. Opening the file with Microsoft Office Excel will display the data headers:

Data Header	**Description**
Time (s)	Axis scan time, where the first half is substrate approach to probe and second half is retraction
Position (um)	PZT position on scale of 0-200 µm for the axis being scanned
Friction (V)	PSD voltage for lateral deflection of the beam
Normal (V)	PSD voltage for vertical deflection of the beam
Friction (rad)	Angle of lateral deflection of the beam, derived from product of friction force voltage and the calibration Voltage to Twist.
Normal (um)	Distance of vertical deflection of the beam, derived from product of normal force voltage and the calibration Voltage to Deflection.
Friction (uN)	Force of lateral deflection of the beam, derived from product of friction force voltage and the calibrations Voltage to Twist and Twist to Force.
Normal (uN)	Force of vertical deflection of the beam, derived from product of normal force voltage and the calibrations Voltage to Deflection and Deflection to Force.
Shunt (V)	Output voltage, directly proportional to the power supply voltage.
Probe (V)	*Channel not used.*
Optical (V)	*Channel not used.*
Shuntcur (A)	Current flow between probe and substrate, derived from quotient of shunt voltage and the combined resistance of the fixed resistor and potentiometer

Table A.3: Mesoscale friction tester data headers with descriptions

A.3 EQUATIONS USED FOR PASCHEN CURVE COMPUTATIONAL MODEL

The work of Albright et al. used a self-consistent non-equilibrium plasma computational model of a copper probe and copper substrate to generate a Paschen curve for argon gas at atmospheric pressure. The computational model has numerous governing equations [11]:

$$\frac{\partial n_k}{\partial t} + \vec{\nabla} \cdot \vec{\Gamma} = \dot{G}_k \qquad k = 1, \ldots, K_g \quad (k \neq k_b) \tag{A.1}$$

where:

n: number density
$\vec{\Gamma}$: number flux of each species
$\dot{G}_k$: source term for species production and destruction
K_g: total number of gas species

$$p = \sum_k n_k k_B T_k \tag{A.2}$$

where:

p: gas pressure
k_B: Boltzmann constant
T_k: temperature of k^{th} gas component
K_g: total number of gas species

$$\vec{\Gamma}_k = -\mu_k n_k \vec{\nabla} \phi - D_k \vec{\nabla} n_k \tag{A.3}$$

where:

μ_k: species mobility coefficient
D_k: diffusion coefficient

$$\nabla^2 \phi = -\frac{e}{\varepsilon_0} \sum_k Z_k n_k \tag{A.4}$$

where:

ϕ: electrostatic potential
e: elementary charge
ε_0: vacuum permeability
Z_k: charge number of species k

$$\frac{\partial e_e}{\partial t} + \vec{\nabla} \cdot \left[\left(e_e + p_e \right) \vec{u}_e - \kappa_e \vec{\nabla} T_e \right] = e \vec{\Gamma}_e \cdot \vec{\nabla} \phi - e \sum_i \Delta E_i^e r_i - \frac{3}{2} k_B n_e \frac{2 m_e}{m_{k_b}} \left(T_e - T_g \right) \bar{\nu}_{e,k_b} \tag{A.5}$$

$$e_e \approx \frac{3}{2} n_e k_B T_k \tag{A.6}$$

where:

e_e: total electron energy per unit volume
p_e: electron pressure
$\vec{u}_e$: total electron convective velocity
κ_e: electron thermal conductivity
ΔE_i^e: energy lost per inelastic collision i
r_i: rate of progress
m_e: mass of an electron
m_{k_b}: mass of the dominant background species
$\bar{\nu}_{e,k_b}$: electron momentum transfer collision frequency with the background gas species

$$\frac{\partial}{\partial t} \left(\sum_{k \in H} n_k h_{k,sens} \right) + \vec{\nabla} \cdot \left(\sum_{k \in H} \kappa_k \vec{\nabla} T_g \right) = S_{T_g} \tag{A.7}$$

$$h_{k,sens} = \int_0^{T_g} C_{p_k} dT \approx C_{p_k} T_g \tag{A.8}$$

$$S_{T_g} = n_j \left(- e \sum_{k \in H} Z_k \vec{\Gamma}_k \cdot \vec{\nabla} \phi \right) - \frac{3}{2} k_B n_e \frac{2 m_e}{m_{k_b}} \left(T_e - T_g \right) \bar{\nu}_{e,kb} - \sum_{k \in H} \dot{G}_k \left(\Delta h_\Gamma \right)_k^0 \tag{A.9}$$

where:

κ_k: thermal conductivity of species k
$h_{k,sens}$: sensible enthalpy of species k
H: set of all heavy species
S_{T_g}: source terms
C_{p_k}: specific heat of species k

η_j: thermalization coefficient

Electron field emission can be the dominant emission form for distances less than 5 µm:

$$j_{FE} = \frac{1.54\times10^{-6}\cdot10^{\frac{4.52}{\sqrt{\phi}}}(\beta E)^2}{\phi}\exp\left(-\frac{6.53\times10^9\phi^{\frac{3}{2}}}{\beta E}\right) \tag{A.10}$$

where:

ϕ: work function of cathode material
E: local electric field normal to electrode surface
β: field emission enhancement factor

A.4 ELECTROCHEMICALLY ETCHED OPPER PROBE TIPS

Each SEM image includes the working distance (WD) used and had accelerating beam voltage of 10 keV.

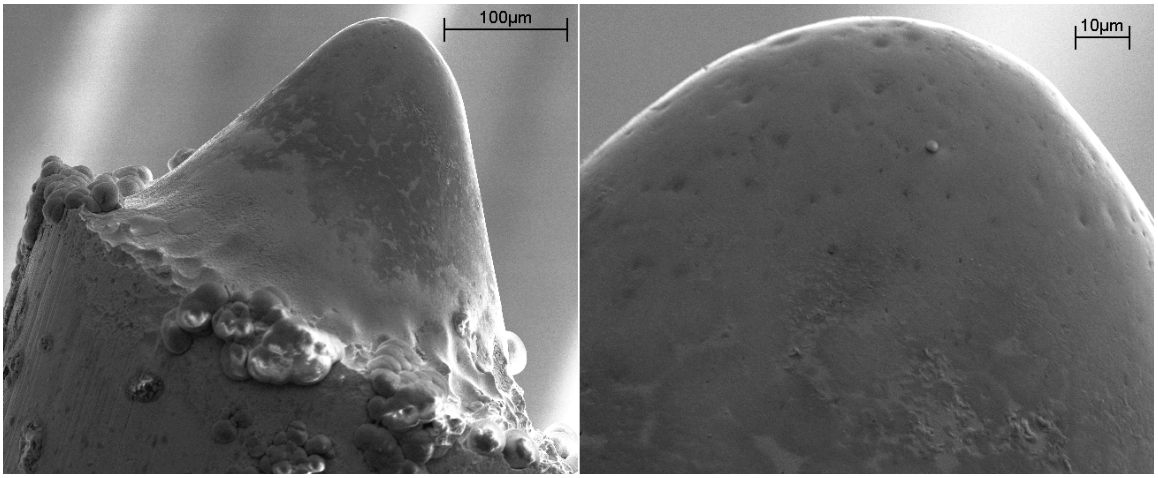

Figure A.2: Copper probe tip etched at 5 V with 43 µm radius of curvature: secondary electron images at 160x and 702x, 11 mm WD

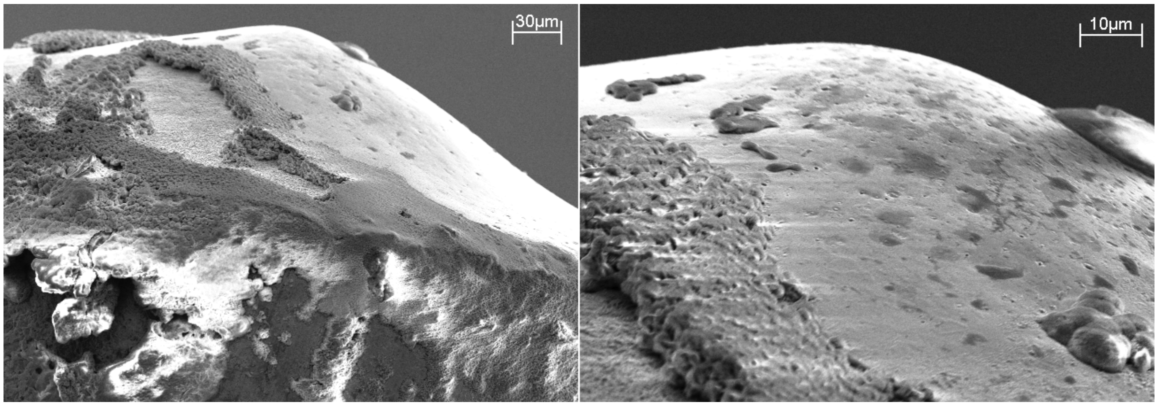

Figure A.3: Copper probe tip etched at 5 V with 74 µm radius of curvature: secondary electron images at 211x and 803x, 11 mm WD

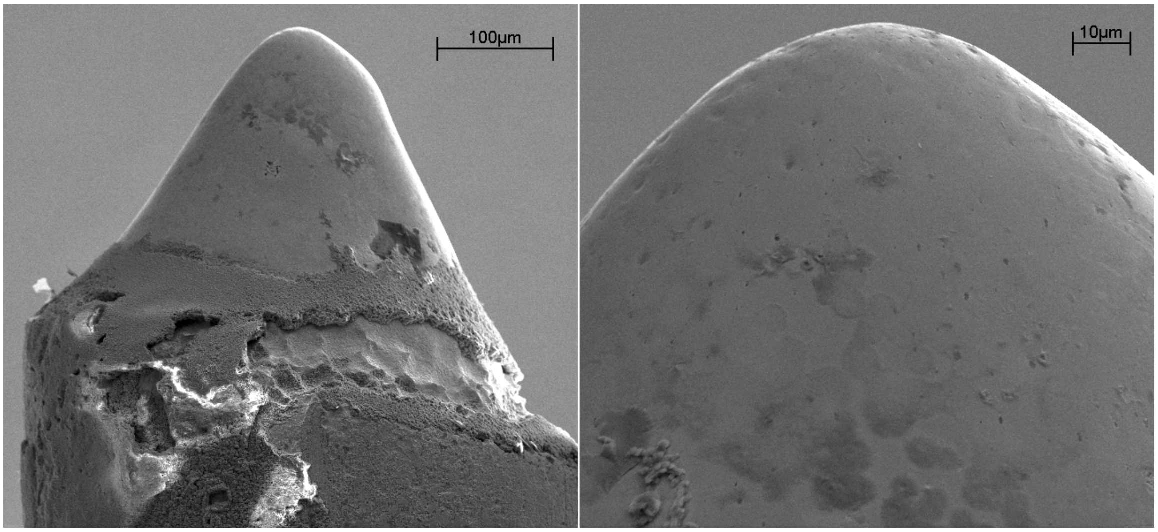

Figure A.4: Copper probe tip etched at 5 V with 44 µm radius of curvature: secondary electron images at 150x and 747x, 11 mm WD

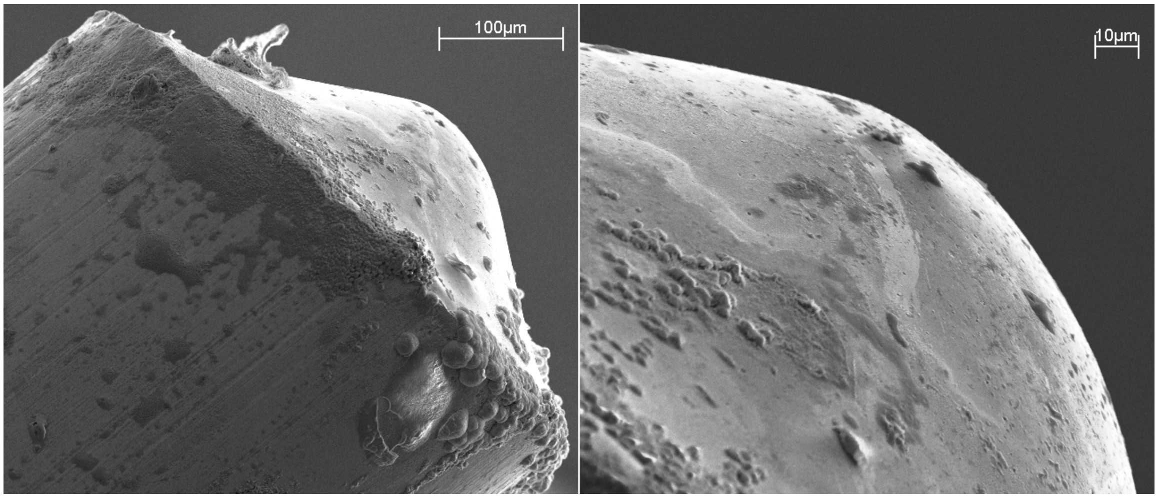

Figure A.5: Copper probe tip etched at 5 V with 156 µm radius of curvature: secondary electron images at 160x and 560x, 11 mm WD

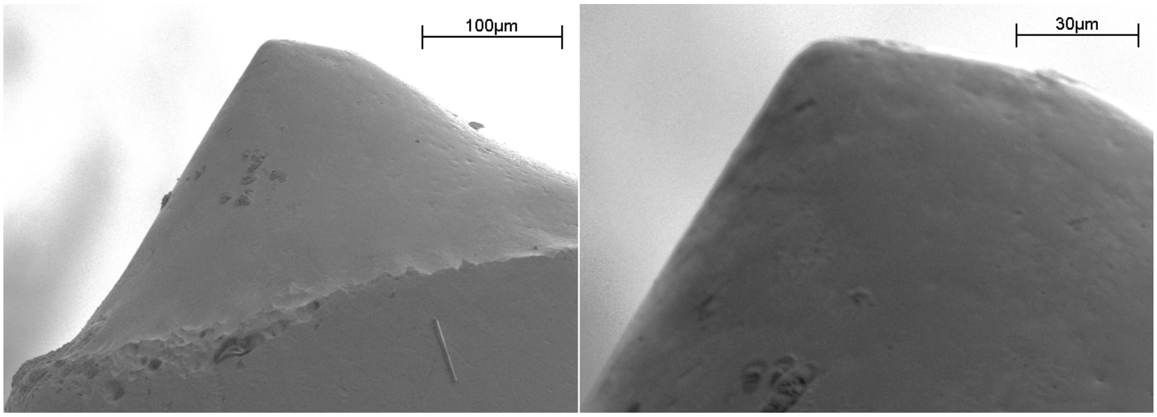

Figure A.6: Copper probe tip etched at 8 V with 23 µm radius of curvature: secondary electron images at 182x and 526x, 11 and 13 mm WD

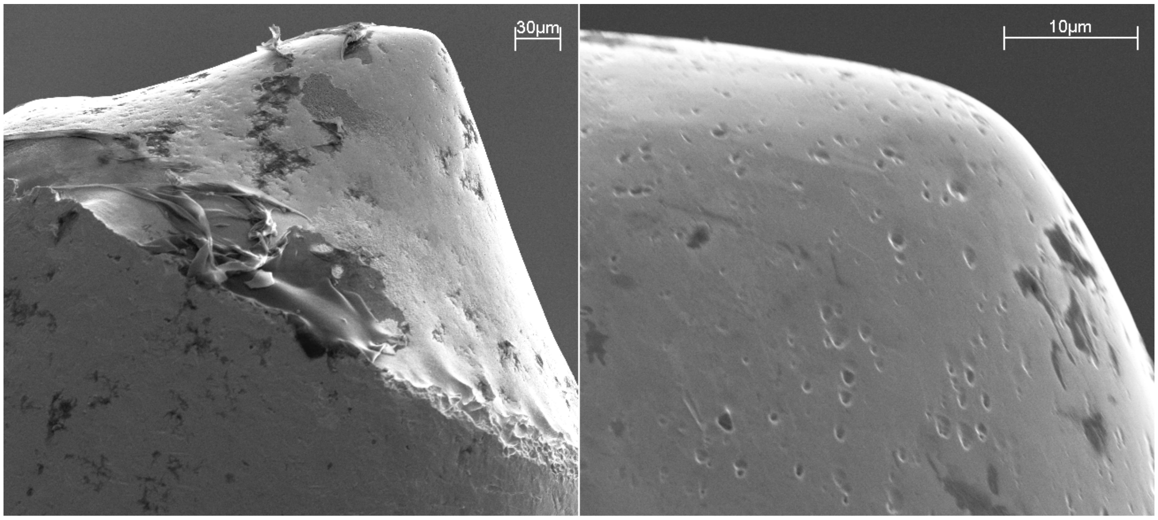

Figure A.7: Copper probe tip etched at 8 V with 32 μm radius of curvature: secondary electron images at 195x and 1720x, 13 mm WD

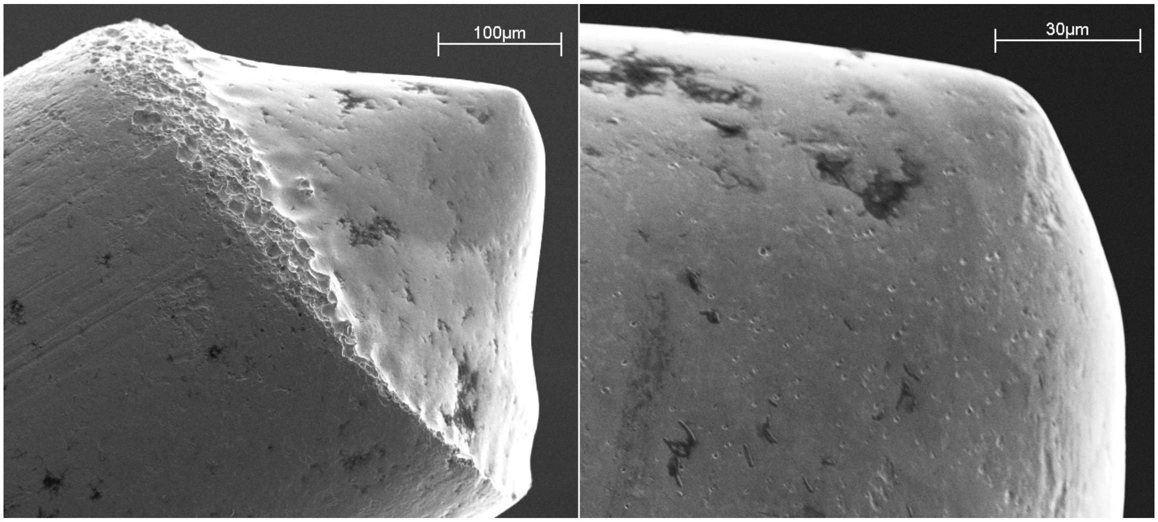

Figure A.8: Copper probe tip etched at 8 V also with 32 μm radius of curvature: secondary electron images at 160x and 628x, 13 mm WD

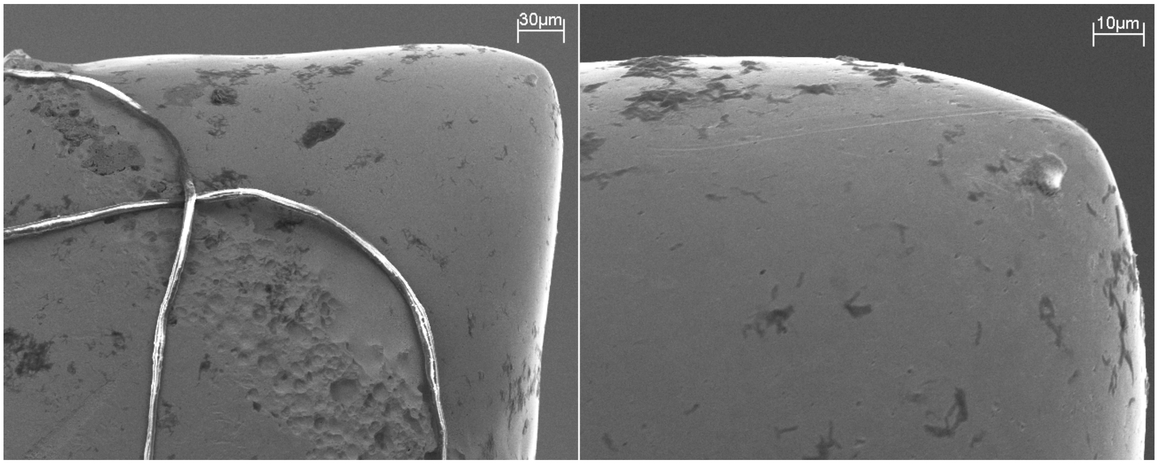

Figure A.9: Copper probe tip etched at 8 V with 34 μm radius of curvature: secondary electron images at 200x and 650x, 13 mm WD

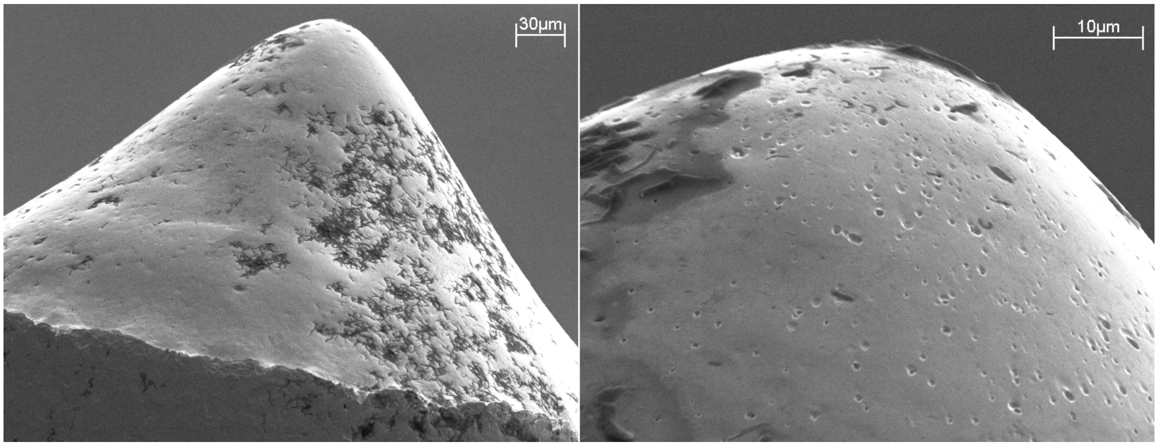

Figure A.10: Copper probe tip etched at 8 V with 48 μm radius of curvature: secondary electron images at 212x and 1150x, 13 mm WD

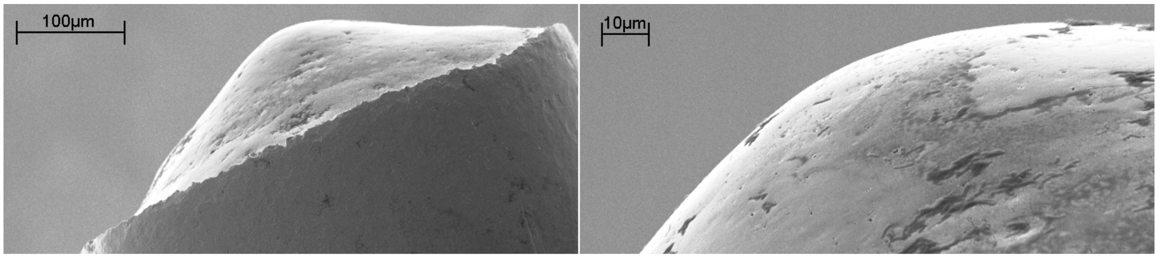

Figure A.11: Copper probe tip etched at 8 V with 114 μm radius of curvature: secondary electron images at 140x and 608x, 13 mm WD

A.5 CONTACT EROSION CALIBRATION

Type	Calibration	Method
Normal	8.65 µm/V	Empirical
	37.6 µN/µm	Analytical
Lateral	0.0215 rad/V	Empirical
	0.81 µN/µrad	Empirical
	0.82 µN/µrad	Analytical

Table A.4: MFT friction calibration with $G = 77.2$ GPa, $c = 9.0$ mm, $L = 19.5$ mm, $B = 12.7$ mm, $t = 76.2$ µm

This current and friction relationship was tested with a copper probe on a copper substrate while holding current density, scan speed, and other parameters constant. Calibrations involved vertical and lateral scans, the beam material and geometry. The stainless steel beam had a 77.2 GPa shear modulus, 19.5 mm length, 12.7 mm width, 76.2 µm thickness, and had a 9.0 mm length copper probe attached. The calibration factors were experimentally or analytically derived and are listed in Table A.4, although the twist to voltage number was a function of normal force and voltage.

Glossary

Arcing: The passing of current between the probe and substrate in the absence of a normal force from physical contact.

Armature: Component of a railgun between the two rails which houses the projectile, for the purpose of forming a closed circuit between the power supply and rails to launch the projectile.

Aspect ratio: Ratio of probe tip length to original diameter of the metal wire.

Asperity: Rough or uneven surface.

Atomic force microscopy (AFM): An apparatus that uses a probe on a cantilever beam to measure a sample's topography with subnanometer resolution. The contact forces and radii used are both smaller than with a MFT.

Contact regimes: The types of interactions from asperities; for the rail-armature interface it is proposed this would include solid-solid contact, liquid-metal lubricated contact, and arcing contact.

Dwell time: The period of time in which the probe and substrate had an electrical arc active.

Elliptic geometry: Non-Euclidian geometry, such as that of the curved surface of an MFT probe tip.

Hysteresis: The path dependent behavior of the probe and substrate in the minimum distance required to initiate or quench electric current.

Field emission: The emission of electrons caused by large electromagnetic fields and the dominant physical mechanism in Paschen curves when working at distances on the order of micrometers.

Lorentz force: A force orthogonal to the magnetic field and electric current used to accelerate a projectile in a railgun, named after physicist Hendrik Lorentz.

Mesoscale Friction Tester (MFT): A machine developed at the University of Texas at Austin that allows for applying forces and probe radii between that of an Atomic Force Microscope (AFM) or a Surface Force Apparatus (SFA).

Muzzle velocity: The instantaneous velocity of a projectile exiting a railgun; used to calculate the kinetic energy of the launcher.

Overvoltage: The difference in applied voltage and the Paschen curve minimum voltage needed to initiate an arc between two electrodes.

Paschen curve: A plot, based on Paschen's Law, showing the relationship between voltage, pressure, and distance between two electrodes in a gas for the minimum potential required to initiate an electrical arc. Modifications for small-distances include the effects of electron field emissions.

Position Sensitive Device (PSD): A detector on the MFT that finds the position of the laser beam's light spot on a two-dimensional plane which can be calculated to measure the forces and deflection acting on the probe.

Quench: The flow of electric current being severed as a result an increasing distance between probe and substrate in the MFT.

Railgun: Electromagnetic launcher that uses conductive rails, a power supply, and an armature to accelerate a projectile using the Lorentz force.

Scanning Electron Microscope (SEM): A microscope that generates images using backscattered and secondary electrons, with advantages of high magnification, resolution, and depth of field.

Spot weld: Two pieces of metal bonding due to applied pressure and heat from electric current flow, occurring over a small area and small time scales.

Topography: The mapping of a localized area's surface features.

Tribology: Study of effects from friction and how to mitigate it.

References

1. L. Brown, D. Xu, K. Ravi-Chandar, S. Satapathy, "Coefficient of friction measurement in the presence of high current density," *IEEE Transactions on Magnetics*, vol. 43, (2007), 334-337.

2. F. Bowden and D. Tabor, *The Friction and lubrication of solids*, Oxford Press, (1964).

3. D. Xu, K.M. Liechti, and K. Ravi-Chandar, "On the modified Tabor parameter for JKR-DMT transition in the presence of a liquid meniscus," *Journal of Colloid and Interface Science*, vol. 315, (2007), 772-785.

4. M. Wang, D. Xu, K. Ravi-Chandar and K.M. Liechti, "On the development of a mesoscale friction tester," *Experimental Mechanics*, vol. 47, (2007), 123-131.

5. D. Xu, K.M. Liechti, and K. Ravi-Chandar, "On scale dependence in friction: Transition from intimate to monolayer lubricated contact," *Journal of Colloid and Interface Science*, vol. 318, (2008), 507-519.

6. D. Xu, K.M. Liechti, and K. Ravi-Chandar, "Mesoscale scanning probe tips with subnanometer RMS roughness," *Review of Scientific Instruments*, vol. 78, 073707 (2007).

7. A.G. López, "Internship report: Study of friction at the mesoscale on copper probe tips," (2008). Unpublished manuscript.

8. P. Hawkes, *Advances in Electronics and Electron Physics*, vol. 78. (Academic Press, San Diego, 1990).

9. M.A. Lieberman and A.J. Lichtenberg, *Principles of Plasma Discharges and Materials Processing*, 1st ed. (Wiley, New York, 1994).

10. A. Wallash, L. Levit, "Electrical breakdown and ESD phenomena for devices with nanometer-to-micron gaps," *Proceedings of SPIE 4980*, vol. 87, (2003).

11. J.M. Albright, L.L. Raja, M. Manley, K. Ravi-Chanadar, and S. Satapathy, "Studies of Apserity-Scale Plasma Discharge Phenomena," (2010). Manuscript submitted for publication.

12. J. Goldstein, D. Newbury, D. Joy, C. Lyman, P. Echlin, E. Lifshin, L. Sawyer, and J. Michael, *Scanning Electron Microscopy and X-Ray Microanalysis*, 3rd ed. (Springer, New York, 2003).

13. J.M. Albright and L.L. Raja (2010), Heat flux and overvoltage. Unpublished raw data.

14. H. Hertz, *Miscellaneous* papers, p. 146, (Macmillan, 1896).

15. D. Xu, *Scale Dependence in Friction: The Transition from Intimate Contact to Monolayor Lubricated Contact* (2007). Ph.D. dissertation. University of Texas at Austin.

Vita

Matthew Halperin Manley was born in Rochester, New York. After graduating from John Overton High School, Nashville, Tennessee he attended University of Michigan in Ann Arbor, Michigan. During the summers of 2005 and 2007 he attended Middle Tennessee State University in Murfreesboro, Tennessee and during summer 2006 participated in a study abroad with the University of New South Wales in Sydney, Australia. He received the degree of Bachelor of Science in Engineering, cum laude, in aerospace engineering with a minor in political science from University of Michigan in April, 2008. In August, 2008, he entered the Graduate School at The University of Texas at Austin.

Permanent Email: mhmanley@umich.edu
Permanent Address: 300 Turnberry Circle
Brentwood, Tennessee 37027

This thesis was typed by Matthew Manley.